UNIVERSITY OF BIRMINGHAM

Passive Bistatic SAR with GNSS Transmitter and A Stationary Receiver

by

Zhangfan Zeng

A thesis submitted to the
School of Engineering
University of Birmingham
for the degree of
DOCTOR OF PHILOSOPHY

Department of Electronic, Electrical, and Computer Engineering
The University of Birmingham
Edgbaston
Birmingham, United Kingdom
B15 2TT

Abstract

Space-Surface Bistatic Synthetic Aperture Radar (SS-BSAR) is a sub-class of BSAR, where the transmitter can be any satellite and the receiver could be mounted on an aircraft, a land vehicle or stationary on the ground. If stationary receiver is applied, the synthetic aperture is fully attributed to the moving of satellite. Such a kind of geometry is suited for ground deformation monitoring.

Our research employs Global Navigation Satellite System (GNSS) as transmitter of Opportunity. This has many advantages. The medium Earth orbit (MEO) of GNSS satellite allows shorter satellite revisit cycles (8-9 days) than imaging radar such as Envisat (35days). Moreover, due to large number of satellites deployed (at least 4 satellites could be seen at any time), persistent monitoring of a given area can be achieved from multiple angles simultaneously. Although the potential radar performances characteristics such as power budget and resolution are outmatched by imaging radar, theoretical calculation shows that they are adequate for our purpose if long integration time is employed.

This thesis presents research results on the imaging capability of SS-BSAR with GNSS and a stationary receiver. Firstly, the system is outlined and the reason of selecting GNSS as transmitter of opportunity is justified. The power budget and resolution were then analyzed. Simulation indicates that a target with Radar Cross Section (RCS) of 50m^2can be detected at range of 1000m if using an integration time of 5 minutes. The end to end signal processing, from received raw data leading to SS-BSAR image, is described. This includes signal synchronization and image formation. The coordinate processing consists of coordinate extraction, interpolation and

transformation. The newly proposed signal synchronization algorithm omits the process of unused secondary code tracking of previous algorithm and improves the efficiency by three times while achieving the same accuracy. The modified imaging algorithm integrates the synchronized signal signatures (i.e. delay, Doppler and phase) and achieves sharp focus after Back Projection (BP) operation. Four experimental data sets acquired at different imaging scenarios are used to test our system hardware and signal processing algorithms mentioned below. It can be seen from the obtained images and associated analysis that such a system has the capability of real scene imaging.

Acknowledgements

First and foremost, I would like to present my thanks to my supervisors, Prof. Mike Cherniakov and Dr. Mike Antoniou. Mike Cherniakov's broad vision and kind personality taught me not only research method, but also how to be a better researcher. With regard to my research, no words can express my gratitude to Mike Antoniou, who directed me to the realm of radar and guided me into how the research should be undertaken. I am lucky to be student and friend of him.

Secondly, I would like to thank all the staffs and colleagues in our lab, i.e. Dr. Marina, Rui, Feifeng, Qilei, Chunyang, Hong Zhou, Sizov, Liam, Amileen, Ayu, Kalin, for their kind help and instructive advice.

Finally, I would like to give my greatest gratitude to my family, who have always given me all kinds of support

Table of Contents

List of Figures

Chapter 1

Chapter 2

Chapter 3

Chapter 4

Chapter 5

Chapter 6

Appendix B

Appendix D

List of Tables

Chapter 1

Chapter 2

Chapter 3

Chapter 4

Chapter 5

Appendix A

List of Abbreviations

2-D	Two-dimensional
3-D	Three-dimensional
ADC	Analogue-to-Digital Converter
ALOS	Advanced Land Observing Satellite
ASAR	Advanced Synthetic Aperture Radar
ATI	Along-Track Interferometry
BASS	Block Adjustment of Synchronizing Signal
BP	Back-Projection
BPSK	Binary Phase Shift Keying
BSAR	Bistatic Synthetic Aperture Radar
CARABAS	Coherent All Radio Band Sensing
CAT	Computer-aided Tomography
CCD	Coherent Change Detection
COSMO	COnstellation of small Satellite for the Mediterranean basin Observation
CSA	Chirp Scaling Algorithm
CW	Continuous-Wave
DAB	Digital Audio Broadcasting
DEM	Digital Elevation Model
DLL	Delay Locked Loop
DLR	German Aerospace Center
DMO	Dip Moveout
DPCA	Displaced Phase Center Antenna

ECEF	Earth Centered Earth Fixed
ENVISAT	Environment Satellite
ERS	European Remote-Sensing Satellite
EU	European Union
FDMA	Frequency Division Multiple Access
FFT	Fast Fourier Transform
FOI	Swedish Defence Research Agency
GAF	Generalized Ambiguity Function
GLONASS	Global Navigation Satellite System
GNSS	Global Navigation Satellite System
GPS	Global Positioning System
HC	Heterodyne Channel
IFFT	Inverse Fast Fourier Transform
IFT	Inverse Fourier Transform
IGS	International GNSS Service
LBF	Loffeld Bistatic Formula
LEO	Low Earth Orbit
LOS	Line of Sight
MSR	Method of Series Reversion
NLCS	Nonlinear Chirp Scaling
ONERA	Office National d'Etudes et de Recherches Aerospatiales
PALSAR	Phase Array L-band SAR
PAMIR	Phase Array Multifunctional Imaging Radar
POSP	Principle Of Stationary Phase
PRF	Pulse Repetition Frequency
PRI	Pulse Repetition Interval

PSF Point Spread Function

PSK Phase Shift Keying

PSLR Peak Side-lobe Ratio

RAMSES Radar Aeroporte Multi-spectral d'Etude des Signatures

RAR Real Aperture Radar

RC Radar Channel

RCM Range Cell Migration

RCS Radar Cross-Section

RDA Range Doppler

TDC Time Domain Correlation

SAR Synthetic Aperture Radar

SCR Signal Clutter Radio

SNR Signal Noise Ratio

SPP Stationary Phase Point

SRTM Shuttle Radar Tomography Mission

SS-BSAR Space-Surface Bistatic Synthetic Aperture Radar

UCT Coordinated Universal Time

UHF Ultra-High Frequency

UOB University of Birmingham

UPC Universitat Politecnica De Catalunya

UWB Ultra-Wide Band

VHF Very High Frequency

WGS84 World Geodetic System 84

CHAPTER 1

INTRODUCTION

1.1 Radar concept

Radar is the abbreviation of **Ra**dio **D**etection **a**nd **R**anging. It uses electromagnetic waves to measure the position and (or) speed of a moving or stationary object such as aircraft, ship, building, car, terrain, etc. A high level definition radar system consists of three elements: transmitter, receiver and target. Transmitter sends a signal along a narrow beam to the target area, a target within this area absorbs a fraction of electromagnetic energy and scatters the remainder [1]. The receiver collects the part of scattered wave controlled by the receiver antenna and acquires the information of the targets according to the received signal parameters.

The radar system can be classified into three categories when the number of platform is taken into account, namely, monostatic radar, bistatic radar and multi-static radar (Fig. 1.1). In monostatic radar, the transmitter and receiver are mounted on the same location, and they use the same antenna to send and receive signals. In bistatic radar, receiver and transmitter are separated spatially. In multi-static radar, there may be

several transmitters with one receiver or one transmitter with several receivers or even multiple transmitters with multiple receivers at the same time. As can be seen, bistatic radar is the simplest case of multi-static radar system.

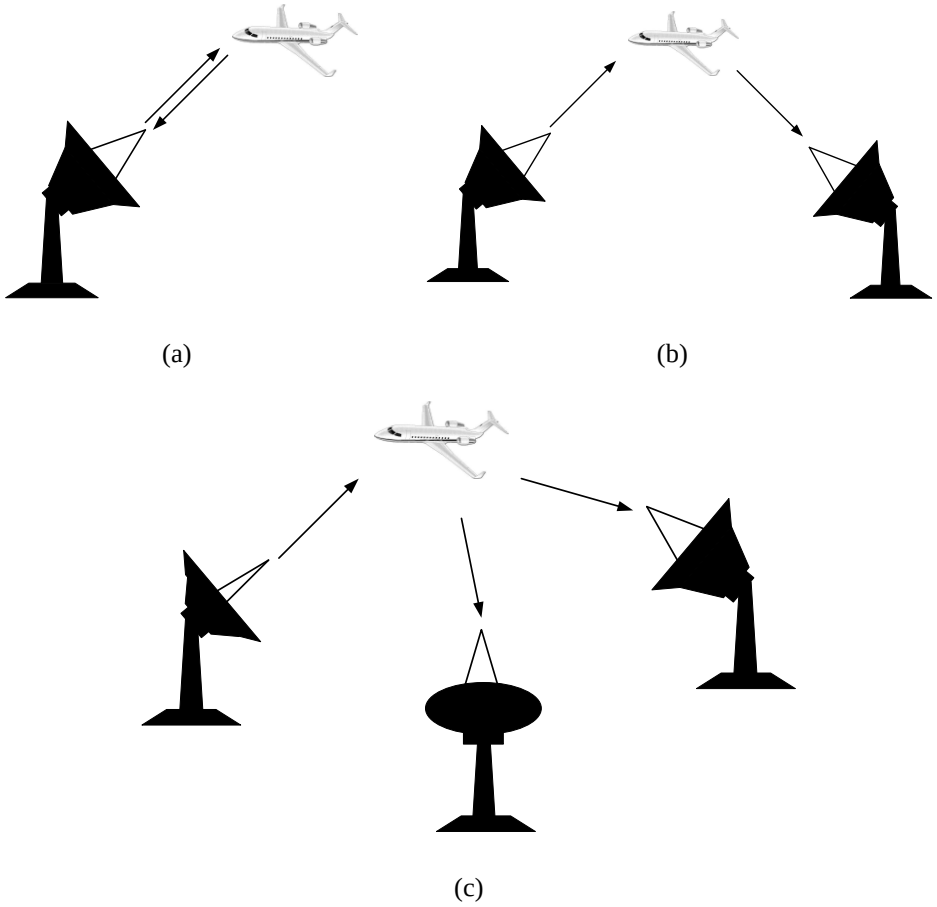

Figure 1.1: Radar configurations (a) Monostatic radar, (b) Bistatic radar, (c) Multi-static radar

Monostatic radar is the most commonly used type of radar, due to its less complex signal processing and better resolution. On the other hand, bistatic radar and multi-static radar have their own benefits both in military service and civil applications as well [2]. For example, the separation of transmitter and receiver make it possible to conceal the receiver off the enemy even if the receiver is quite close. Moreover, the radar vision could be largely enhanced by multi-perspective sources from multi-static radar. The most noteworthy advantage of multi/bi-static radar is a lower built and maintenance cost, particularly if a non-cooperative transmitter is met.

There are various types of radars in terms of application, such as surveillance radar, weather radar and imaging radar, etc.. Our research is restricted to imaging radar, which is performed by Synthetic Aperture Radar (SAR). SAR may be monostatic, bistatic or multistatic.

In this chapter, section 1.2 introduces the concept of monostatic SAR and commonly used monostatic SAR sensors. Section 1.3 outlines bistatic SAR and reviews the published bistatic studies. Then the research status of Space Surface Bistatic SAR is reported in section 1.4. Following up, the motivation and problem statement for this thesis are stated in section 1.5. Finally, the thesis structure is given in section 1.6.

1.2 Synthetic Aperture Radar

1.2.1 Concept of SAR

SAR was proposed against Real Aperture Radar (RAR), where the azimuth location of a target is measured by its antenna directivity. The azimuth resolution of a monostatic radar at a particular range r is given by

$$\delta_a \approx \frac{\lambda}{D} r \tag{1.1}$$

where λ is the radar signal wavelength, D is the horizontal dimension of the radar antenna.

Eq. (1.1) shows that in order to improve the azimuth resolution, the only method is to employ a large antenna (as signal wavelength and range are fix). For example, if a RAR is working at 1.2GHz, to achieve the 1m azimuth resolution at range of 1km, the length of the antenna will be 250 m [1].

In contrast, SAR syntheses a large effective beam by moving a small antenna radar for a long distance. Fig. 1.2 illustrates the concept of monostatic spotlight SAR.

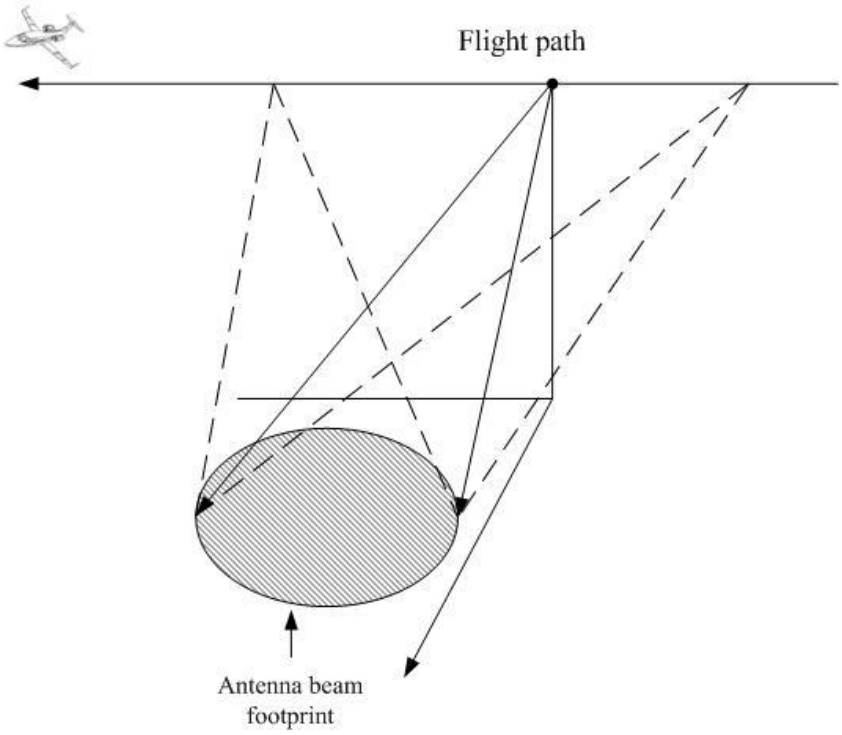

Figure 1.2: Concept of monostatic spotlight SAR

In Fig. 1.2, the radar is mounted on an aircraft. As the platform moves on, the radar records signal from the target on the sequence of platform locations and adds them coherently. The effective length of synthesized aperture will be motion distance. To form an image, the received signal will be re-formatted to two dimensional. One is along the movement direction, called azimuth direction. The other is perpendicular to movement direction, called range direction. By compressing signal in both directions, the responses of targets can be reconstructed. It should be noted that, in order to achieve high resolution in range and azimuth direction, large transmitted signal bandwidth and long observation time are required respectively.

1.2.2 Overview of SAR sensors

SAR was first discussed in 1950's when Carl Wiley [3] observed that the objects in different azimuth locations could be identified from their different instantaneous Doppler shifts. By moving the physical real aperture, finer azimuth resolution can be achieved. Since then, numbers of SAR sensors have been developed and put to practical utilizations. The most representative SAR sensors currently used are summarized in Table 1.1:

SAR sensors	Platform	Frequency	Maximum range resolution (m)	Acquisition mode
ENVISAT/ASAR	spaceborne	C	28	stripmap/scanning
RADARSAT 2	spaceborne	C	3	stripmap/spotlight
TerraSAR-X/ TanDEM-X	spaceborne	X	1	stripmap/spotlight/ Scanning/ sliding spotlight
ALOS/PALSAR	spaceborne	L	7	stripmap/scanning
Cosmo/SkyMed		X	1	stripmap/spotlight/ scanning
F-SAR	airborne	L/X/S/C/P	0.3	stripmap/spotlight
RAMSES	airborne	P/L/S/C/Ku/ Ka/W	0.1	stripmap
PAMIR	airborne	X	0.07	stripmap/spotlight/ sliding spotlight
MiniSAR	airborne	Ku/Ka/X	0.1	stripmap/spotlight

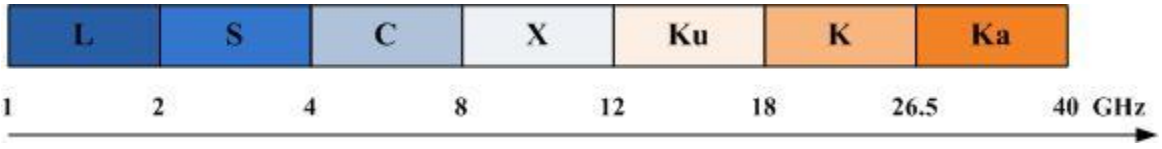

Table 1.1: Commonly used SAR sensors

1.3 Bistatic SAR

1.3.1 BSAR concept

The key feature for BSAR system is its physical separation between transmitter and receiver, which can be in either form, i.e. moving or stationary, as long as at least one is moving. The synthetic aperture can be attributed to either one of them or both. Their trajectories may be independent and random. Fig. 1.3 shows the concept of BSAR system, where both transmitter and receiver are moving.

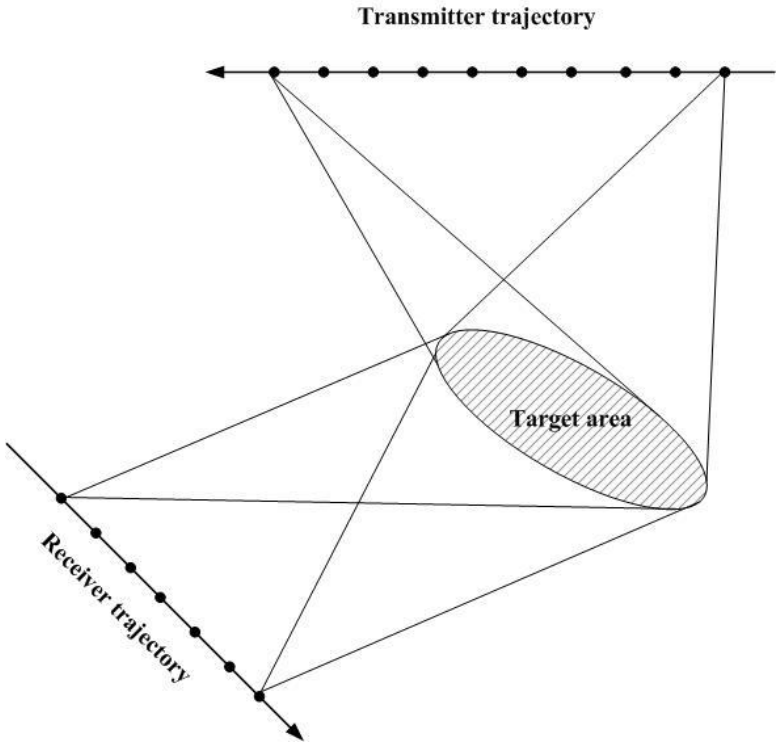

Figure 1.3: General BSAR geometry [2]

Bistaic SAR is more complex than monostatic SAR in terms of signal processing. In monostatic SAR, the synthetic aperture is fully formed from movement of a single radar platform. Doppler history and delay history are only relevant to the position of radar relative to the target. In bistatic SAR, however, Doppler history and delay history are resulted from two independent time-varying paths, increasing the

complexity. The most fundamental problem is synchronization between transmitter and receiver. Moreover, signal compression suffers from more restriction, as their relative position are varying.

1.3.2 BSAR configuration

Bistatic SAR configuration can be diverse, defined by transmitter and receiver trajectories. With regard to the geometry complexity, the bistatic SAR can be summarized into (partially according to [4]).

- Translational invariant configuration:

  Translational invariant configuration refers to the geometry that the Doppler history does not vary with targets' azimuth positions. The translational invariant case could be classified into two subclasses. One is Tandem configuration, where the transmitter and receiver are lined up with constant baseline. The other is configuration stage 2 specified in [4], where the transmitter and the receiver move in parallel.

- Translational variant configuration

  Translational variant configuration, on the contrary, refers to the geometry that the Doppler history varies with targets' azimuth positions. The translational variant configuration could be also classified into two subclasses. One is one-stationary configuration, where one of the platforms is stationary. The other is configuration stage 3 specified in [4], where transmitter and receiver has arbitrary but constant velocity vectors.

- General configuration

General configuration refers to the geometry that transmitter and receiver travel on arbitrary flight paths at arbitrary velocities.

Different BSAR configurations possess different signal models and characteristics, therefore different types of image algorithms will be adopted to accommodate various BSAR systems. A large number of works have discussed the nature and 2-D spectrum of both translational invariant and translational variant configurations, and their expectations not only on theoretical level, but from practical point of view. Nevertheless, the investigation of generic analytical expression of 2-D spectrum of general case has not yet been achieved. The major published work will be reviewed in the next section.

.

1.3.3 Published work on BSAR systems

This section provides an overview of research undertaken and literature available on BSAR. Ground based transmitter BSAR is described first, followed by airborne transmitter and spaceborne transmitter BSAR systems.

A. BSAR WITH GROUND-BASED TRANSMITTER

Sheen [5] dealt with a low frequency, ultra-wide bandwidth bistatic SAR system with the aim of foliage transmission measurement. In the work, the transmitter is a ground-based carriage moving horizontally and the receiver is fixed on a tripod. Experimental results were presented, which supported expectation that the foliage attenuation is affected by different radar configurations such as carrier frequency, polarization, depression angle, etc. In [6], an experimental ground based BSAR system is introduced. The transmitter moves on top of a truck bed, while the receiver is mounted on a stationary tripod adjacent to the truck. Aimed at achieving BSAR

interferometry, the author placed two antennas for echo reception and two complex images were obtained for the same target scene. Subsequently, the elevation information of the target was acquired by image comparison and a 3-D image was created. Therefore, the proof of concept of such a interferometry system was demonstrated.

B. BSAR WITH AIRBORNE TRANSMITTER

Soumekh [7] discussed an along-track bistatic SAR configuration for detecting moving targets. In his work, two sensors are employed, but on the same aircraft. The work was limited to simulation, however, it demonstrated a technique for moving target indication by such configuration. In [8], a preliminary airborne InSAR experimental result has been demonstrated by using two aircraft flying across track. Associated signal processing stages, such as synchronization, orbit determination, etc.. have been discussed and implemented to perform interferomgram. This experiment was the first trial of such configuration and demonstrated the feasibility of interferometric applications with such a configuration. An airborne bistatic SAR program conducted by QinetiQ has been considered in 2006 [9]. In the experiment, two X-band SAR sensors are mounted on one aircraft and one helicopter respectively. The paper presented the obtained bistatic images at different grazing angles, followed by comparison to corresponding monostatic counterparts. The work showed that, superficially, the images appear similar to the monostatic ones. Moreover, different scattering mechanisms were observed after comparing bistatic and monostatic images. Dubois [10] discussed an airborne bistatic SAR scheme to investiage bistatic scattering behaviour of natural and urban targets. In his research, two aircraft were used, one is RAMSES of ONERA, the other is E-SAR of DLR. Two types of geometrical configuration were applied, one is quasi-monostatic mode, where two

planes were flying very close to each other, the other is large bistatic angle case and the baseline is 2 km. Bistatic images were obtained at different configurations and natural surface characteristics were analyzed. Walterscheid [11] reported a translational invariant flight experimental image result obtained from bistatic range migration algorithm. Through their work, one SAR sensor is a Dornier with AER-II and the other is a Transall C-160 with PAMIR. A modified range migration processor for such a configuration has been developed, which was demonstrated to enable good error control. An experimental data was used to confirme its proper functionality. In [12][13], the UWB CARABAS bistatic SAR campaign has been outlined. In the work, the transmitter is an aircraft flying with a non-linear track and receiver is fixed on the mountain top. Data evaluation of various polarization schemes and different elevation angles have been examined. Moreover, a method for Signal Clutter Ratio (SCR) improvement has been proposed. Obtained preferable image suggested that bistatic configuration with higher elevation angle allowed better SCR and ground target detection. Balke introduced a Ka band forward-looking airbone bistatic measurement in [14][15], where the transmitter is moving and the receiver is stationary on the ground. The obtained image showed that two-dimensional resolution could be achieved in bistatic case, which is unattainable for monostatic counterpart. In addition, it proposed a novel idea to measure the height of target by using shadowing effects in bistatic image. Baque [16] reported bistatic VHF/UHF airborne SAR experimental results based on joint grant of ONERA in France and FOI in SWEDEN, aimed at evaluating performance of low frequency (i.e. UHF/VHF) bistatic SAR for clutter suppression for various applications. In their work, two airborne SAR sensors are flying in parallel, with the transmitter in various inclination angle and receiver fixed. Flight measurements with different configurations were conducted and the

signal processing until ultimate images were given. The obtained bistatic images were compared with monostatic images in terms of SNR, scattering nature, etc., suggesting some peculiarities for bistatic configuration. Also, success in detecting under foliage objects proved this applicability. Goh [17] reported a large bandwidth (600MHz) airborne bistatic SAR system and image results. In his system, the transmitter is following a circular trajectory and the receiver is stationary on the ground. A number of images were obtained at various bistatic geometries. The resulting bistatic image was found to be of superior quality when a comparison with monostatic counterpart was performed. Several conclusions concerning image artefacts were risen.

C. BSAR WITH SPACEBORNE TRANSMITTER

Recent years witnesses availability of spaceborne BSAR campaign due to numbers of advanced satellite SAR sensors being deployed, from pioneer ERS to current TerraSAR-X. Different BSAR variants have been applied to a range of applications. For example, the spaceborne receiver case is best for large area ground monitoring with the aid of spaceborne interferometry. Airborne receiver case is useful in battle surveillance and ground-based receiver case is best for small area ground monitoring.

C.1 SPACEBORNE TRANSMITTER/GROUND-BASED RECEIVER

Cazzani [18] reported a ground-based stationary bistatic SAR system with geostationary TV satellite transmission. The signal processing issue such as signal compression and stop-go assumption has been taken into account. A preliminary image has been obtained with resolution at order of 10 meters. It could be predicted that such a system is promising for differential interferometry. Scientists in UPC conducted a large number of works with ground based SAR and spaceborne transmitter of opportunity [19]-[25], named “SABRINA”. They used radar satellite

such as Envisat, ERS-2 and TerraSAR-X as the transmitter and placed the self-built receiver on a building roof to monitor nearby terrains. The experimental prototype has three channels mounted the receiver, one is for direct signal reception, the other two are potentially used for image and interferometry. From this system, they got the single look complex image [19][24][25] and single pass interferogram [20][21][22]. The obtained DEMs were compared with SRTM. The results demonstrated the validity of this system. A bistatic SAR along-track interferometry (ATI) for moving objection detection was also obtained with such a system [23]. Preliminary results have been given, providing the ability of moving target indication in terms of position and velocity using this kind of configuration. The discussions were also given with regard to relationship between baseline length and unambiguous velocity. Whitewood [26] examined the same variant of BSAR configuration for imagery feasibility study in UCL. System hardware, potential radar performance, image processing algorithm and obtained bistatic image are described and analyzed. Additional potential applications such as DPCA have been proposed by using another antenna.

Radar imaging remains an on-going problem, and the investigations about bistatic artefacts are appearing in the open literatures. Tore described a methodology of surface characterization by using multistatic GNSS SAR in [27]. Surface reflectivity dependence on illumination angle has been examined. This illustrates the feasibility of using reflected GNSS signals for environmental remote sensing. Reuter [28] introduced a stationary SAR receiver system using TerraSAR-X as a transmitter of opportunity. This system featured with high bandwidth up to 300 MHz, which resulted in range resolution less than 1m. A reference image was obtained and compared with monostatic counterpart, demonstrating peculiarities of bistatic mode. In this final form, The system will be developed as an interferometer. Wang reported

a Chinese spaceborne/stationary bistatic SAR experiment, signal processing and image results in [29]. In the measurement, transmitter is Chinese satellite "YaoGan-1" and receiver is fixed on the ground. Modified CSA was applied to focus the data. The major conclusion is that, after comparing with monostatic spaceborne image from the same satellite, bistatic image yielded better SNR, better vegetation detect-ability but severe shadowing effects.

C.2 SPACEBORNE TRANSMITTER/AIRBORNE RECEIVER

Guttrich [30] discussed concept of a space-based surveillance radar by using hybrid bistatic SAR configuration, where the signal is transmitted from a geo-synchronous satellite and received by unmanned airborne vehicles (UAV) or other satellites. It was observed that such configurations can provide either airborne moving target indication or ground moving target indication and they were much more cost-effective compared with an equivalent monostatic system. [31][32][33] examined a double sliding spotlight bistatic SAR configuration, where the transmitter is satellite TerraSAR-X and receiver PAMIR is a wide band (150 MHz) SAR sensor mounted on the plane. The resulting bistatic image with BP algorithm verified that the non-stationary bistatic SAR with double sliding spotlight mode is possible. After comparison between monostatic SAR image and bistatic counterpart, different shadowing, shortening and scattering effects have been observed, which could be used for target classification and image interpretation. In [34][35], another airborne SAR sensor, namely, F-SAR was tested together with TerraSAR-X. Such a configuration has potential for numerous prospective applications. System hardware, synchronization and imaging algorithm were described. Image analysis based on comparison with monostatic SAR image were provided in detail, which outlined several peculiarities of bistatic mode

such as higher SNR, different scattering mechanisms, different Doppler information and different geometric mappings. Once again, using the same equipments as in reference [33], Walterscheid and Espeter presented a wide bandwidth (300MHz) bistatic spaceborne-ariborne forward-looking SAR campaign and image results in [36][37]. In these works, iso-range and iso-azimuth contours were examined, suggesting expected values of range and cross-range resolution. In such a configuration, bistatic image was given finally, demonstrating good agreement with ground truth and resolution analysis. Takashi [38] introduced a bistatic spaceborne/airborne SAR experiment developed in Japan. In his article, the transmitter is a Japanese satellite ALOS and receiver is an airborne 28MHz band width SAR sensor Pi-SAR-L. A resulting experimental image was presented and three key observations were pointed out with regard to BSAR peculiarities after comparing with monostatic image of the same area: higher SNR, coarse azimuth resolution, different target detection capability.

C.3 SPACEBORNE TRANSMITTER/SPACEBRONE RECEIVER

Prati [39] proposed a passive geosynchronous bistatic SAR system with objective of differential interferometry. The signal is fired from a DAB satellite and is received by a geosynchronous satellite. Proof of concept performed via radar capacity analysis such as spatial resolution and link budget demonstrated feasibility of such a configuration. Mittermayer [40] discussed the system feasibility for spaceborne interferometry using Cartwheel and Envi-Sat. The advantage was that ASAR's standard image mode is attractive as the height measurement was expected to have less fluctuation. The drawback was the practical implementation and Doppler Centroid estimation. By simulation experiment, it could be observed that in such a

bistatic image mode, height error could be controlled. Lee [41] and Girard [42]described a concept of tandem mission for earth observation using RADARSAT-2 and RADARSAT-3. The design and operational issues were discussed. It has been demonstrated that this tandem mission was able to get a high accuracy DEM product by achieving high resolution imagery provided adequate orbit control was adequate. Errico [43] discussed the system concept of BISSAT mission for earth observation, where an active radar satellite (ENVISAT, COSMO/SkyMed) was used as a primary SAR source and a number of small satellites as passive receivers. The technical issues such as orbiting synchronization and antenna synchronization were addressed. Furthermore, he presented the analysis of system performance for oceanographic applications with BISSAT. It was suggested that, for larger azimuth angle of propagation and baseline, the performance could be greatly improved. Krieger [44][45] provided a comprehensive description of single-pass SAR interferometry to map and monitor the earth surface using TanDEM-X and further with TanDEM-L. The system overview, proof of concept, interferometric performance and DEM products have been presented and evaluated. In addition, aimed at global acquisition of Three-dimensional (3-D) forest structure and systematic observations of glacier movements, twin L-band satellites, namely, TanDEM-L was proposed. An outlook on such a configuration in terms of future advanced SAR concepts and developments was provided. In [46][47], Rodriguez reported a TanDEM-X experiments and associated interferometry products, in the purpose of validating and calibration of TanDEM-X in terms of capability of bistatic imaging and interferogram acquisition. The final obtained repeat-pass interferogram and single pass interferogram demonstrate the feasibility of TanDEM-X as an good interferometer.

1.4 Space surface bistatic SAR with GNSS

1.4.1 Definition of SS-BSAR with GNSS

Here we discuss a particular type of bistatic SAR, where the transmitter is GNSS satellite of opportunity, and receiver could be spaceborne, airborne, mounted on a land vehicle or fixed on the surface of the earth (Fig. 1.4). If the receiver is stationary, the aperture is synthesized by the motion of the source while measurement are made. We refer all the configurations mentioned above as SS-BSAR with GNSS.

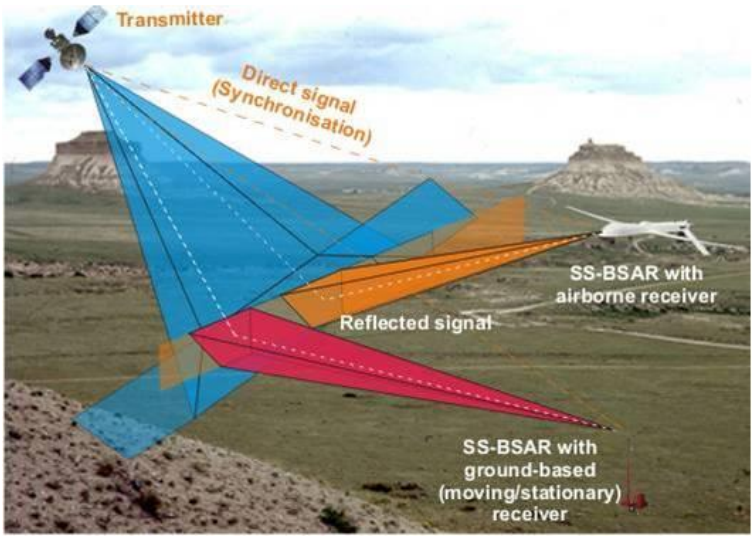

Figure 1.4: SS-BSAR with GNSS engagement geometry

The high-level operation principle of SS-BSAR with GNSS is much the same with that of other spaceborne BSAR systems. However, employment of GNSS as the transmitter of opportunity allows a number of unique characteristics compared with other spaceborne BSAR systems:

- SS-BSAR with GNSS is more cost-effective, due to that we do not need to build radar transmitter, and the receiver is a standard low cost GNSS receiver.
- As such a system is in passive mode, receiver is safely concealed of enemies even at small stand-off distance.

- Fast revisit period, all-day, all weather monitoring is possible, as there are large number of satellites and quick revisit time (8 days) for a single satellite.
- Such a system can provide reliable operation, since GNSS rarely fails, and when it does, can be known in advance.
- As the configuration is bistatic, the target area may be observed from an optimal direction, which may be problematic in monostatic SAR.
- SSBSAR performances such as power budget and resolution are inferior to what are achieved with a imaging satellite. But are expected to be adequate for earth observation if long integration time is employed.

1.4.2 Previous published work

The University of Birmingham (UOB) has done an extensive work in the area of SS-BSAR with GNSS, both on analytical and experimental level. The previous work concentrated on fundamental radar performance analysis and signal processing in moving receiver case. The ambiguity function and resolution analysis of such a system were examined in [48][49]. The power budget and interference level evaluation could be found in [50][51]. Interferometric applicability [52] and surface change detection [53] were studied. The image algorithm modified for SS-BSAR with GNSS could be referred to [54]-[58], where three different configurations have been considered, namely: SS-BSAR with stationary receiver, with parallel transmitter-to-receiver trajectory (different velocities), and generalized SS-BSAR. Signal synchronization algorithm could be found in [59][60]. [61][62] summarized the work.

1.5 Problem statement and contribution

This thesis is dedicated to the case of SS-BSAR with GNSS and a stationary receiver (Fig. 1.5). Such a system was first studied in 2008 [63]. After preliminary investigation of its radar performances such as satellite availability, resolution and power budget, it has theoretically shown that such a system is promising for local area Coherent Change Detection (CCD) at long integration time acquisition (in the order of minutes). To implementing CCD, the first and foremost step is the image formation.

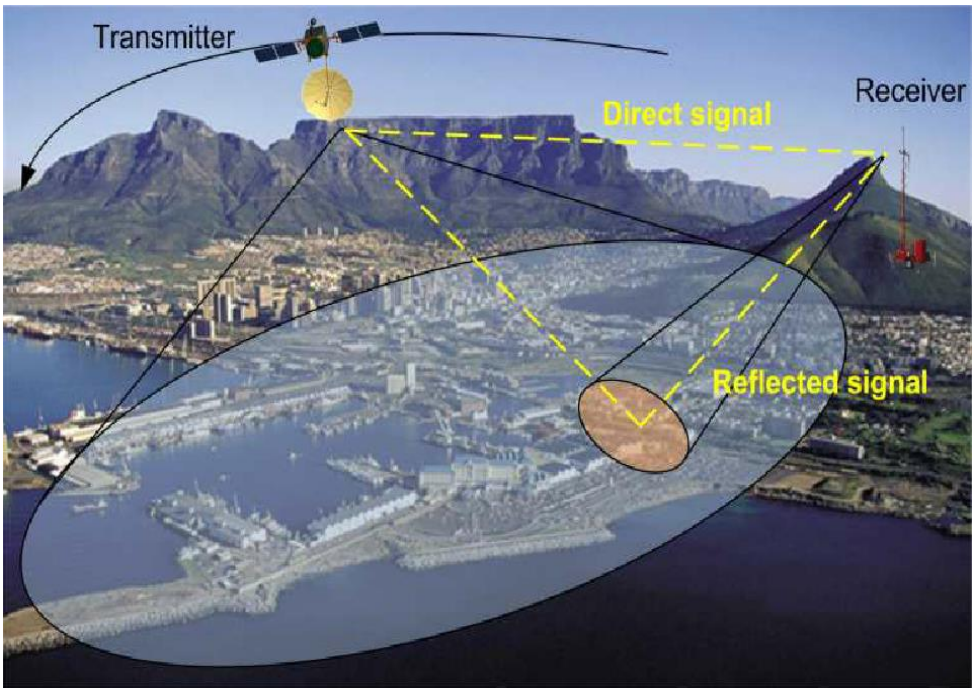

Figure 1.5: SS-BSAR with GNSS and stationary receiver

The main objective of this thesis is to demonstrate imagery capability of passive bistatic SAR with GNSS satellite as transmitter of opportunity and a ground based stationary receiver. The major challenge of this task is that such a BSAR system is a novel technology, combining diverse subjects i.e. passive mode, navigation satellite, poorer radar performences, non-cooperative transmitter, asymmetric geometry. These include:

- Lack of knowledge of coordinate processing for such a radar system

- Like any bistatic radar, synchronization between transmitter and receiver is required in our system for coherent SAR processing. In addition, due to long integration time applied, the raw data size will be up to (13Gbyte) and phase error accumulated will be considerable. As such, a robust and more efficient synchronization algorithm than old one [60] is required to accommodate such problems.
- Again as long integration time is applied, satellite transmitter's trajectory will no longer be linear, resulting in the failure of frequency domain algorithm (sub-aperture technology can be used, but will be outmatched in terms of image focusing accuracy). Moreover, How to integrate the synchronized signal parameter to the time domain algorithm will be investigated.

This PhD thesis considers all the techniques and aspects with regard to image formation from raw data and associated application using SS-BSAR with GNSS as a transmitter of opportunity and a stationary receiver, which could be illustrated using block diagram shown in Fig. 1.6.

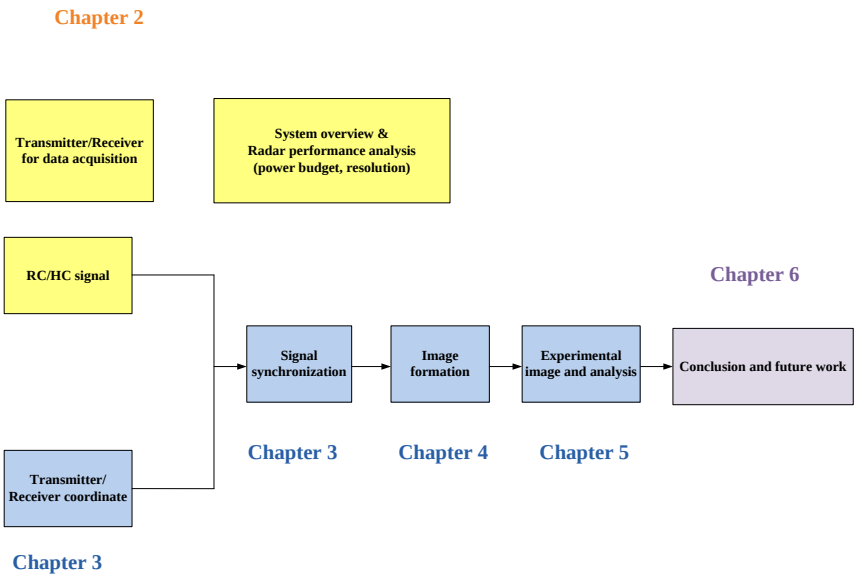

Figure 1.6: Flow chart of thesis contents

These include

- Examination of the radar performance of SS-BSAR with GNSS and a stationary receiver, including power budget and resolution analysis. In terms of resolution, a careful work has been conducted for PSF analysis at long integration time on both theoretical and experimental level [64].
- Understanding of the coordinate processing for image purpose, this includes coordinate standard, coordinate extraction, coordinate interpolation and coordinate transformation. This part is adopting everything that already known to our system with modifications accordingly.
- Development of a fast and accurate signal synchronization algorithm for SS-BSAR with GNSS, especially beneficial for stationary case. This algorithm increases the efficiency by more than 3 times and preserves the same performance as the previous one [65].
- Development of a modified BP algorithm for SS-BSAR with stationary receiver. The key technique lies in how the synchronized results integrated to the conventional bistatic BP algorithm. Through simulation, we found that, by properly reference signal generating, the target point response are well focused after 2-D compression.
- Four representative experiments were conducted: prototype experiment, feasibility study experiment, Vale village experiment and Metchley park experiment. Experimental results and analysis were presented. It has been demonstrated that all the images were well focused, and different ground features well observed from images [66][67].Moreover, resolution and power budget calculation is examined practically.

With regard to publications during PhD period, seven journals and four conference paper (author and co-author) have been published or accepted. A list of those is attached in Appendix E.

1.6 Thesis outline

Chapter 2 provides an overview of the passive BSAR with GNSS and stationary receiver system. In this part, the transmitter parameters and receiver equipments are described in details. Justification has been given for the GLONASS as the transmitter. The system performance such as power budget and resolution are analytically derived and simulated.

Chapter 3 describes the proposed synchronization algorithm for our system, aimed at dealing with large size data during experiment. In this chapter, the signal pre-processing (i.e. coordinate processing) as well as both conventional algorithms and proposed algorithm are discussed. Comparisons between these two are provided by using experimental results.

Chapter 4 reports the modified back-projection imaging algorithm used in our system. A literature review of image formation algorithm is given at first place, stating the necessity of development of a this imaging algorithm. Then a detailed analytical expression is given. The algorithm is finally verified with simulation and compared with theoretical counterpart.

Based on the theoretical radar performance analysis and signal processing algorithms discussed in the first four chapters, the experimental image results and analysis are

presented in Chapter 5. The philosophy of the experimental designing was stated at first place. Then the SS-BSAR images acquired during my PhD and associated discussions are given.

Chapter 6 summarizes the main findings and conclusions of this thesis followed by the possible future works that could be worked with this system.

CHAPTER 2

SYSTEM OVERVIEW AND EXPERIMENTAL SPECIFICATION

2.1 Introduction

This Chapter provides a system overview (topology, transmitter and receiver) and experimental specifications of a specific SS-BSAR system, where the transmitter is GNSS and receiver is stationary near the earth's surface. The aim is to give a outline of our system configuration, how it works and what performance (power budget and resolution) it can achieve. The system topology is described initially together with unique characteristic of such a configuration. The existing GNSS is outlined briefly. It is suggested that GLONASS outperforms others in current status. A detailed description of GLONASS transmitter parameters then follows. The equipment used for data collection is then described briefly. Finally, the radar performances including power budget and spatial resolution are examined.

2.2 System configuration

This thesis focuses on SS-BSAR imaging using GNSS as transmitter of opportunity and a fixed receiver (Fig. 2.1). The transmitter moves along its orbit and fires signal

continuously to the earth's surface. The receiver is located near the ground (e.g. on the mountain, or on the roof of a buildings, etc.) and pointing to targeting area. By coherent signal processing on the collected GNSS signal reflected from this area. Its objects and terrain can be reconstructed on a SAR image.

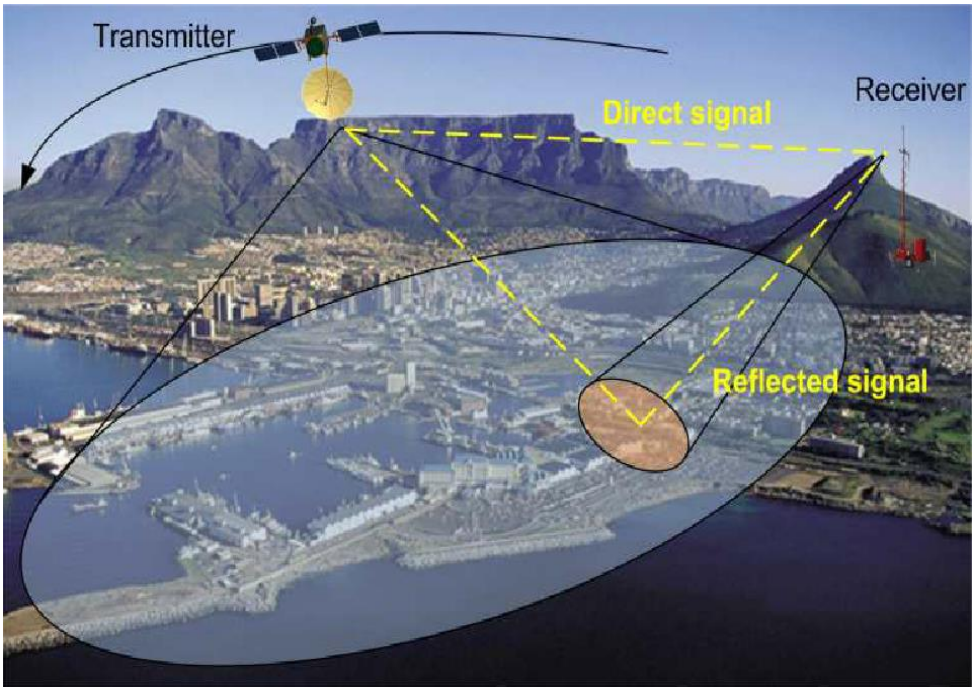

Figure 2.1: SS-BSAR with GNSS and stationary receiver

It is noteworthy that SS-BSAR assumes the use of any spaceborne transmitter, either radar imaging satellite (e.g. TerraSAR-X) or other satellites such as DAB satellite, GNSS and communication satellite, etc. GNSS as the transmitter is considered in this thesis. The reasons are multiple. Even though GNSS are obviously outmatched by radar satellites in terms of radar performance (power budget, resolution), theoretical calculations [63] has confirmed the system feasibility when long dwell times (at least 5mins to provide an azimuth resolution of 2-3m) are considered. Moreover, GNSS transmitters use atomic clocks for signal generation, which are highly accurate and introduce minimal phase noise. Finally, and perhaps most importantly, GNSS are satellite constellations, allowing persistent monitoring of a given area from multiple

aspect angles simultaneously and therefore unimpeded by local landscape. Besides, the architecture of satellites within the same GNSS constellation, combined with the inter-operability between different constellations, allows the use of simultaneous, multi-static imaging of a given area. It is expected that this mode of operation will be a new emerging technology in its own right, since it will not only enhance the overall system performance, but also provide additional and new types of area information.

Such a system may be used for persistent ground deformation monitoring. The first and foremost step is SS-BSAR imaging and it is the core of this thesis.

2.3 Illuminator

2.3.1 GNSS satellites

GNSS is the common name of satellite-based systems that provide navigation, positioning and time transfer, etc. with global coverage. The most well-known of GNSS are GPS from United States, GLONASS from Russia, Galileo from European Union and Beidou from China.

GPS [70] is the first global position satellite system developed by USA in last 70th. It was intended to provide earth surface positioning for both military and civil services. The fully deployed constellation consists of 24 satellites within six planes (each has 4 satellites). All the satellites use the same carrier frequency, the difference between each satellite is its own pseudo-random coded employed. Beside navigation message, GPS ranging code consists of two kinds of pseudo-random codes, i.e. C/A-code and P code. C/A code is used for users to get the existence and coarse information of the satellites. P-code is short for Precision code and is used for more precise navigation.

The ultimate positioning accuracy will be 100 m for civil use and 10 m for military use.

GLONASS [71] is another GNSS operated by Russia. It began to develop in 1976 and 24 satellites are in operation at current status. Like GPS, all the 24 satellite are distributed over three orbital planes, differs by 120 degree in between. Each satellite operates at an inclination angle of 64.8 degrees with the speed of 3953 m/s. The frequency scheme GLONASS used is quite different to GPS, i.e. each satellite has its own carrier frequency. This kind of frequency scheme is called Frequency Division Multiple Access (FDMA) technique. Same with GPS, GLONASS ranging code also consists of P-code and C/A code navigation message, which have similar contents but different chip rate and coding structure. The P-code and C/A code are the same for all the satellites. The ultimate positioning accuracy of GLONASS will be up to 1m.

Galileo [72] is a newly developed GNSS by EU in past decades. The main aim is to provide high precision positioning service to the Europe Zone and even all over the world for its own right. It is currently being developed by several countries within European Union (EU). Full constellation of satellites will consist of 30 vehicles, however only four are on the sky up to now. Like GPS, same frequency is applied for all satellites. Galileo ranging code consists of primary code, secondary code and navigation message. Primary code is the same for all satellites, while secondary code is unique for every satellite. The accuracy of Galileo will be better than 4m and 8m along horizontal direction and vertical direction respectively if two bands signals are measured simultaneously.

Beidou [73] is a new and fast-growing GNSS developed by China. It started at 1980 and up to now, according to latest news, 15 satellites have been operated and regional Beidou system has been covering China and neighbouring regions. Global services won't be offered until 2020. The full constellation would consist of 35 satellites, where 5 would be geo-stationary satellite and other 30 would be non-geostationary. Similar to GPS and Galileo, Beidou's ranging signal is comprised of two kinds of sseudo-random code and all the satellites share the same frequency band. A high localization accuracy of 10 meter would be provided free of charge, and a licensed service would be more accurate. However, little are known about other technical parameters from open sources.

The parameters of GNSS satellite transmitters are listed in Table 2.1

GNSS	GPS	GLONASS	Galileo
Channel	L1	L1	E5a/b
Central Frequency (MHz)	1575.42	1602.5625-1615.5	1191.795
Chip Rate (M/s)	C/A: 1.023 P-code: 10.23	C/A: 0.511 P-code: 5.11	10.23
Antenna gain (dBi)	13.5	11	15
Beam width	38	36	38-40
Power output (W)	50	50	50
Min power received (dBW)	-158	-155	-155
Orbit altitude (km)	20180	19130	23222
Power Density (dBW/	-127	-128	-126

m^2)			

GNSS usually have several channels for signal transmission. However, this thesis only considers L1 channel for GPS and GLONASS, as well as E5a/b for Galileo

Table 2.1: Parameters of GNSS transmitters [74]

It could be noted that, after comparing statuses of these four existing navigation satellite systems, the most preferable one we can use currently as our transmitter is GLONASS. The reasons are that the GPS can't provide good reasonable resolution (1.023MHz signal bandwidth results in minimum range resolution of 100m). Galileo only has 4 satellites and it is in testing stage, where a stable operation can't be guaranteed. Nevertheless, when Galileo is fully operational, it will be the best. Beidou 's global coverage is not performed until 2020. This PhD thesis is based on GLONASS as the transmitter of opportunity, the parameters of experimental system will be given in following Sections.

2.3.2 GLONASS transmitter parameters

The GLONASS satellite transmits navigation signal in two bands, L1 (1.6GHz) and L2 (1.2GHz). FDMA is used in both bands, different GLONASS satellite transmit signal at different carrier frequency. The frequency intervals between neighbouring sub-bands are 562.5 KHz and 437.5 KHz for L1 band and L2 band respectively. The satellites frequency follows equations below:

$$f_{L1} = 1602MHz + k \times 562.5kHz \tag{2.1}$$

$$f_{L2} = 1246MHz + k \times 437.5kHz \tag{2.2}$$

where k is number of channel, from -7 to +13. More information about GLONASS carrier frequencies is described in Appendix A

Both L1 band and L2 band signals could be used, in our research, however, only L1 band signal is concerned in this thesis.

2.3.3 GLONASS signal structure

GLONASS satellites provide two types of navigation signals like other navigation system, standard accuracy signal and high accuracy signal. Standard accuracy signal is also called C/A code. High accuracy signal is called precision code (P-code). The block diagram of GLONASS signal is shown below:

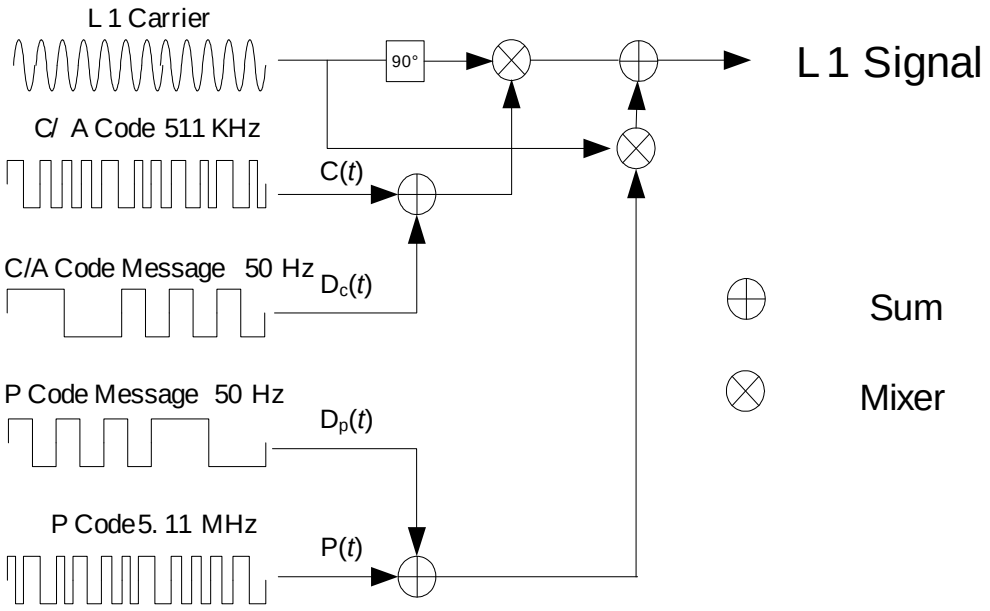

Figure 2.2: GLONASS L1 signal structure [74]

The simplified mathematical formula of the GLONASS L1 signal, neglecting the signal amplitude could be written as:

$$Y(t) = P(t)D_P(t)\cos(\omega_c t + \varphi) + C(t)D_c(t)\sin(\omega_c t + \varphi) \qquad (2.2)$$

where *Y* is the L1 signal, *P(t)* is the P-code, $D_p(t)$ is the P-code navigation message, ω_c is L1 frequency, φ is initial phase, *C(t)* is the C/A code, $D_C(t)$ is the C/A code navigation message.

C/A code is a binary bit sequence generated by a nine bit shift register (Fig. 2.3), which could be described by a polynomial of $1 + x^5 + x^9$. The clock frequency is 511 kHz and the code is 511 characters long, indicating that the code duration is 1 milliseconds.

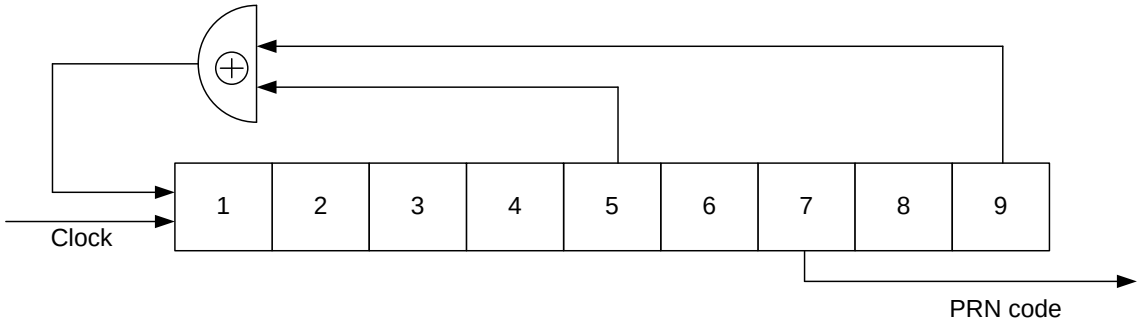

Figure 2.3: GLONASS C/A code generator [71]

P-code is a shortened m-sequence of binary bits, derived by a twenty five bit shift register (Fig. 2.4), which is mathematically presented as $1 + x^3 + x^{25}$. The clock frequency is 5.11 MHz and the code is 33554431 characters long, indicating that the code duration is 6.566 seconds. The final used P-code is 1 second long after signal truncating.

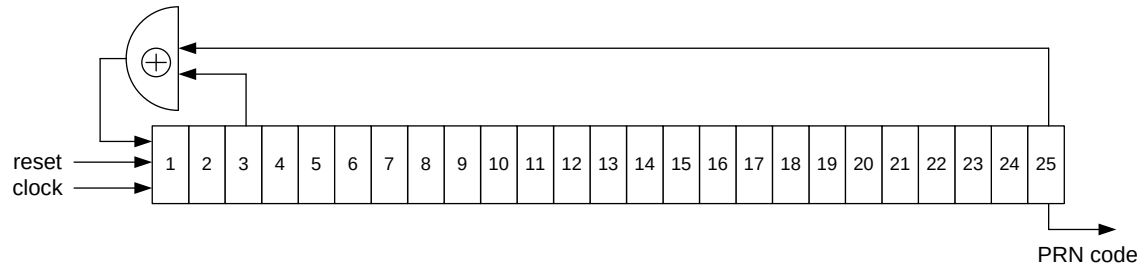

Figure 2.4: GLONASS P-code generator [71]

Navigation message is scrambled to the C/A code and P-code with module 2 adding operation. The sampling interval is 20 milliseconds.

It is noteworthy that, due to higher chip rate of P-code than C/A code and navigation message, P-code will be used in our system for image formation, due to larger resolution expected. Other components will either be removed or served as a systematic noise.

2.4 Receiver equipments

The receiver prototype comprises a two-channel super-heterodyne receiver. Both channels are identical. The receiver can be split in three stages (Fig. 2.5(a)): radio frequency (RF), intermediate frequency (IF) and baseband. The RF part consists of an amplifier with gain of 35dB. Down-conversion to the IF stage is achieved by mixing the RF signal with the output of a frequency synthesizer. It is at this stage that signal amplification with gain of 100dB and filtering is performed. The frequency down-converter is tuneable and can be adjusted to the carrier frequency of any GNSS satellite. Therefore, this system can be seen as a generic tool for recording any GNSS signal for a variety of remote sensing applications. The baseband region is where quadrature demodulation is performed. The signal is down-converted to baseband by a second frequency synthesizer (140Hz). Both frequency down-converters use the same reference clock. Quadrature outputs from each channel are then digitized at Analog-to-Digital Converter (ADC) and stored to a PC with a sampling frequency of 50MHz, so all signal processing operations are done offline. A photograph of the receiver is shown in Fig. 2.5 (b).

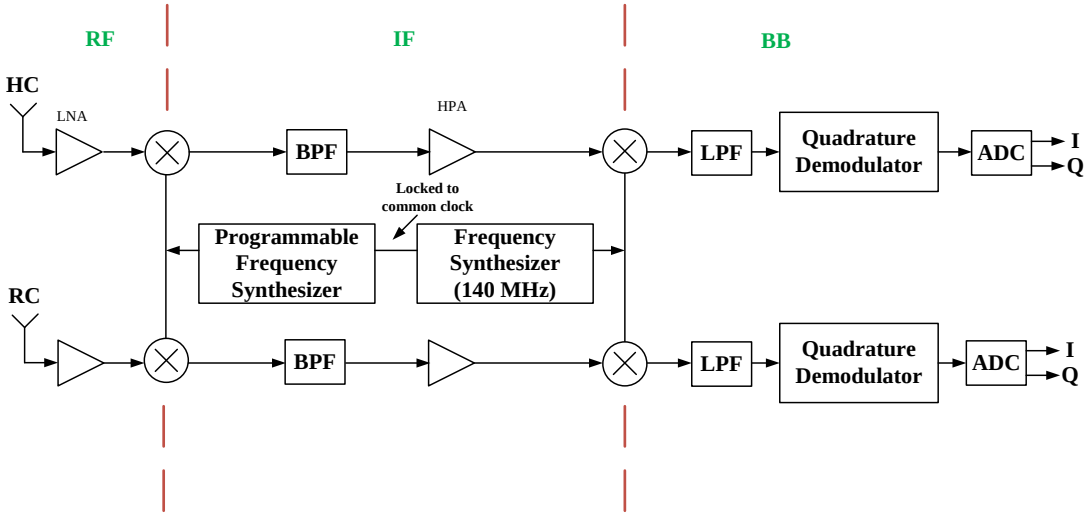

(a)

(b)

Figure 2.5: (a) Block diagram of receiver, (b) Photograph of receiver from outside

It could be seen that three channels may be used (red circles) for data collection. Two channels (1, 3) are usually used as heterodyne channel (HC) and radar channel (RC), another channel (2) could then be used for other potential application such as interferometry, etc.. Heterodyne channel receives signal directly from satellite, the collected signal is used for synchronization between transmitter and receiver (see

chapter 3). Radar channel receives signal reflected from target area with the purpose of image formation.

Two different types of antennas are used for HC signal and RC signal reception respectively. A low-gain HC antenna is applied to receive the direct signal from the satellite (Fig. 2.6(a)). It has the gain of 5 dBi and beamwidth of $60^0 \times 60^0$(horizontal, elevation). The broad beamwidth antenna ensures that the satellite is within its field of view for the whole dwell time. A helical RC antenna is used to receive satellite signal reflections from an area of interest (Fig. 2.6(b)). It has the gain of 16 dBi for main-lobe and -12 dBi for back-lobe, and its -3dB beam width is 30×30^0 (horizontal, elevation).

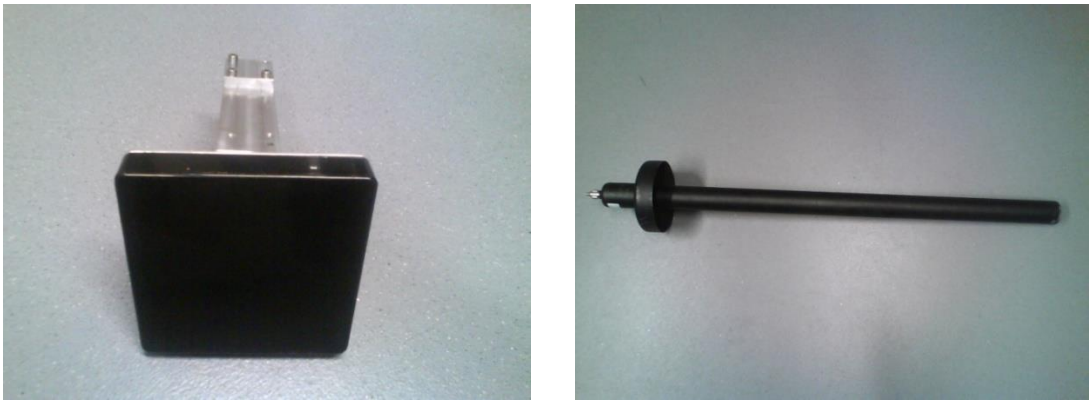

(a) (b)

Figure 2.6: (a) HC low-gain antenna, (b) RC helical antenna

2.5 Experimental specification

2.5.1 Power budget

This section presents the power budget calculation of fixed receiver SS-BSAR with GLONASS transmission from theoretical point of view. Power received for both RC and HC are considered. Moreover, the calculation of SS-BSAR image SNR is discussed.

In general, we assume the GLONASS satellite signal performs uniform power flux density coverage on the earth's surface:

$$\rho = \frac{P_t G_t}{4\pi R_{st}^2} \tag{2.3}$$

where P_t is the power output from satellite (W), G_t is the transmitter antenna gain in dBi, and R_{st} is the distance between satellite and receiver or target on the earth.

A. HC SNR

HC receives signal directly from satellite, it is free from clutter and multipath. In this case, the received signal is only corrupted by systematic noise. The power budget for the HC is actually a line of sight (LOS) communication link power calculation. The signal power at receiver input is the product between power flux density and antenna effective aperture. From antenna theory, the effective aperture of heterodyne channel antenna is

$$A_h = \frac{G_h \lambda^2}{4\pi} \tag{2.4}$$

where G_h is the HC antenna gain (dBi), λ is the wavelength of GLONASS signal.

Thus, the signal power arriving at HC is given by.

$$P_h = \rho \times A_h = \frac{P_t G_t G_h \lambda^2}{(4\pi)^2 R_{st}^2} \tag{2.5}$$

On the other side, the receiver noise power is defined as:

$$P_n^h = kT_s B_n F \tag{2.6}$$

where k is Boltzmann constant with the value of $1.3806505\times10^{-23} J/K$. B_n and T_s are noise bandwidth and thermal noise temperature of the system, F is noise factor of the receiver.

Finally, the HC SNR will be the ratio between signal power over system noise, which could be expressed as:

$$\frac{S}{N_h} = \frac{P_h}{P_n^h} = \frac{P_t G_t G_h \lambda^2 \eta}{(4\pi)^2 R_{st}^2 k T_s^h B_n F} \tag{2.7}$$

where η is assumed to be system loss factor, which is estimated to be 0.5 (taking into account of various factors such as integration loss, processing loss, antenna polarization loss, etc.).

B. RC SNR

Unlike direct signal reception in HC, the received signal power at RC is the product of two-way transmission, which consists of power transmission between transmitter to target and target to receiver.

The total reflected signal power from target object could be given as the product between power flux density of GLONASS transmitted signal (ρ) and Radar Cross-Section (RCS (σ_b)) of this object:

$$P_{ta} = \rho \times \sigma_b \tag{2.8}$$

Then, assuming the target object is the illumination source, with power of P_{ta}, the power flux density at radar channel antenna should be given as:

$$\rho_r = \frac{P_{ta}}{4\pi R_{tr}^2} \tag{2.9}$$

Therefore, the signal power at RC receiver (main-lobe) input could be product between power flux density at radar channel antenna (ρ_r) and antenna size (A_{rm}):

$$P_{rm} = \rho_r \times A_{rm} = \frac{P_t G_t G_{rm} \lambda^2 \sigma_b \eta}{(4\pi)^3 R_{st}^2 R_{tr}^2} \tag{2.10}$$

where G_{rm} is the antenna gain at main-lobe.

It is noteworthy that GLONASS signal will be also absorbed by RC antenna back-lobe directly as well. Similar to HC, signal power arriving at RC back-lobe is given by

$$P_{rb} = \frac{P_t G_t G_{rb} \lambda^2}{(4\pi)^2 R_{tr}^2} \tag{2.11}$$

where G_{rb} is the RC antenna back-lobe gain.

Assuming both heterodyne channel and radar channel have the same system thermal noise, which refers to (2.6), the SNR of radar channel signal from main-lobe and back-lobe could be expressed respectively as:

$$\frac{S}{N_{rm}} = \frac{P_r}{P_n^r} = \frac{P_t G_t G_{rm} \lambda^2 \sigma_b \eta}{(4\pi)^3 R_{st}^2 R_{tr}^2 k T_s^r B_n F} \tag{2.12}$$

$$\frac{S}{N_{rb}} = \frac{P_r}{P_n^r} = \frac{P_t G_t G_{rb} \lambda^2 \eta}{(4\pi)^2 R_{st}^2 k T_s^r B_n F} \tag{2.13}$$

C. SAR image SNR

The GNSS ranging signal, after collected by RC, is then re-formatted into 2-D, i.e. range and azimuth directions. Imaging is formed by signal compression along both range and azimuth, which can yield gain up to hundreds dB.

The range compression gain is achieved based on the considerable difference between chip duration $(1/B)$ and pulse length (T_c):

$$G_{rc} = \frac{T_c}{1/B} = B \times T_c \tag{2.14}$$

where B is chip rate of pseudo-random signal. T_c is the signal pulse length. For example, The chip rate of GLONASS P-code used in our experiment is 5.11 MHz and pulse length is 1 millisecond. It is worth noting that if the signal were a sine wave, the

product of signal bandwidth and signal duration would equal unity, giving no compression gain. If the signal were a chirp signal, the signal bandwidth would increase linearly with the signal duration, the compression gain could be written as $k_r \times {T_c}^2$, where k_r is the chirp rate.

On the other hand, the azimuth compression gain is the number of integrated signals accumulated, which is given by:

$$G_{ac} = \frac{T_{total}}{T_c} \tag{2.15}$$

where T_{total} is the total dwell time on target.

The SNR improvement at imaging stage is attributed to both ranging compression and azimuth compression, given by:

$$G_{img} = G_{rc} \times G_{ac} = B \times T_{total} \tag{2.16}$$

Therefore, The SNR of HC image could be written as:

$$\frac{S}{N_{img,h}}(dB) = \frac{S}{N_h}(dB) + G_{img}(dB) \tag{2.17}$$

The SNR of target at a given range in RC image acquired from main-lobe could be calculated by:

$$PB_{img,rm}(dB) = \frac{S}{N_{rm}}(dB) + G_{img}(dB) \tag{2.18}$$

Again, the SNR of image acquired at RC antenna back-lobe could be written as:

$$\frac{S}{N_{img,rb}}(dB) = \frac{S}{N_{rb}}(dB) + G_{img}(dB) \tag{2.19}$$

Consider the parameters of GLONASS transmitter and receiver (Fig. 2.6) listed in Table 2.2, Eq. (2.17), (2.18) and (2.19) could be written as:

$$\frac{S}{N_{img,h}}(dB) = 43 + 10log10(5.11 \times T_{total}) \tag{2.20}$$

$$PB_{img,rm}(dB) = 42 + 10log10(\frac{\sigma_b}{R_{tr}^2}) + 10log10(5.11 \times T_{total}) \tag{2.21}$$

$$\frac{S}{N_{img,rb}}(dB) = 26 + 10log10(5.11 \times T_{total}) \tag{2.22}$$

It is noteworthy that GNSS satellite power density varies with satellite number and its position, the calculation presented here is for illustration of the method.

Parameter	symbol	information
Transmitting power density	ρ	1.29×10^{-13}(w/m^2)
Range between satellite and receiver	R_{st}	19130km
HC antenna gain	G_{rh}	5dBi
Radar channel antenna main-lobe gain	G_{rm}	15dBi
Radar channel antenna back-lobe gain	G_{rb}	-12dBi
Range between target and receiver	R_{tr}	0-1km
Transmitting signal wavelength	λ	0.1873m
Boltzmann constant	k	1.38×10^{-23} J/K
Experimental dwelling time	T_{total}	300s
Loss factor	η	0.5
System noise temperature	T_s^r	290Kelvin
System noise bandwidth	B_n	5.11MHz
Signal bandwidth	B	5.11MHz
Noise factor	F	1.5

Table 2.2: Experimental prototype parameters [74]

The theoretical evaluations of HC image and RC image SNR are presented in Fig. 2.7. Fig. 2.7(a) shows the gain obtained at image formation stage through 2-D signal compression. It can be seen that 300s dwell time enable 91.86 dB gain on raw data. Fig. 2.7(b) shows HC image SNR at varying dwell time, observation of the result curve shows that the response of receiver at HC image is expected to be 74.86 dB higher than noise floor if dwell time of 300s is applied. This is quite high due to

noise-free, scattering-free environment. Fig. 2.7(c) shows the RC image SNR, it could be found that even the signal is received from antenna back-lobe with gain of -12dBi, the direct reception enable noise floor be lower than 60 dB if dwell time 300s is applied. Fig. 2.7(d) examines SNR of target with different RCS (i.e. $10m^2$, $50m^2$, $100m^2$and $200m^2$) at a given range in RC image. Inspection of this plot indicates that the power budget limits the maximum range detected, but an object with RCS of $50m^2$ can be detected up to 1km from the receiver by our system. Moreover, after comparing Fig. 2.7(b) and (c), the intensity of response at receiver acquired from RC antenna back-lobe is normally higher than echo intensity reflected from targets through RC antenna main-lobe if the targets are more than 100m from the receiver. The SS-BSAR image demonstrated in Chapter 5 will verify this conclusion.

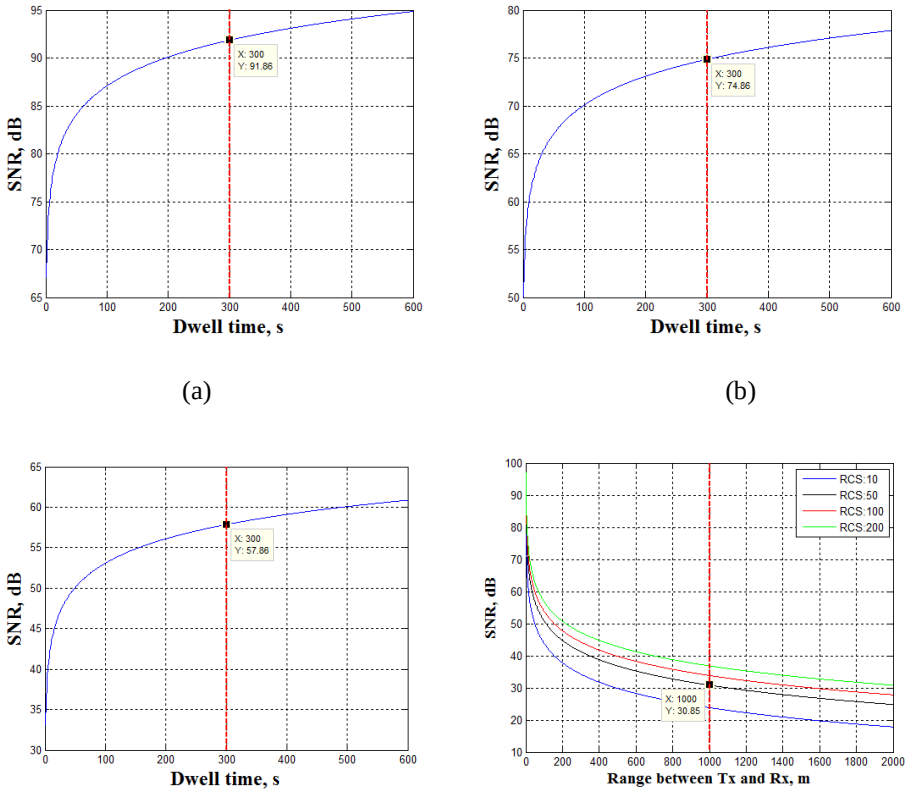

Figure 2.7: (a) 2D macthed filter compression gain in image formation, (b) HC image SNR vs. dwell time, (c) RC image SNR vs. dwell time, (d) RC image power budget calculation

The simulation results demonstrate that the power budget limits the maximum range, but it is quite adequate at distance up to 1km if essentially long integration time up to 5 minutes is employed, where even a small scatterer may be detected.

2.5.2 Ambiguity function and resolution analysis

A. Generic SSBSAR ambiguity function

The general system geometry of fixed receiver bistatic SAR is shown in Fig. 2.8.

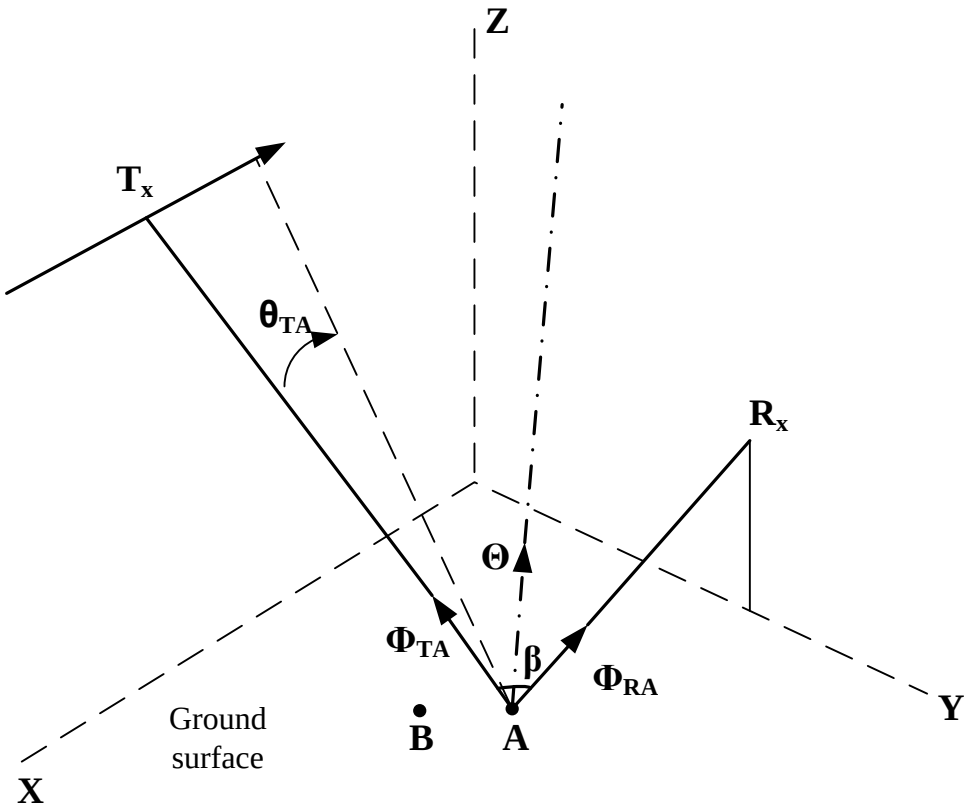

Figure 2.8: General geometry of SS-BSAR with stationary receiver [74]

In Fig. 2.8, A is a target of interest and B is an arbitrary point target close to A. Transmitter is flying along T_x and receiver is located at R_x. $\Phi_{TA}$is unit vector from A to transmitter, and $\Phi_{RA}$is unit vector from A to receiver. β is the bistatic angle relative to point target A. $\theta_{TA}$is the rotation angle of transmitter with regards to starting position during dwell time.

To study the SAR spatial resolution, two methods are widely employed [49]. One is Point Spread Function (PSF), which provides the SAR system response, given that there is only a single point target. The other is the Generalized Ambiguity Function (GAF), which is more commonly used for general radar system resolution analysis. Here, GAF is used for BSAR analysis. The analytical expression can be written as [49]:

$$\begin{aligned}\chi(A,B) &= e^{(j2\pi f_c \tau_{BA})} \int \bar{P}(f) e^{(j2\pi f \tau_{BA})} df \cdot \int \bar{M}_A(u) e^{(j2\pi f_{dc} u)} du \\ &= e^{(j2\pi f_c \tau_{BA})} \cdot p(\tau_{BA}) m_A(f_{dc}) \end{aligned} \quad (2.23)$$

where f_c is the radar working frequency, f is the fast-time frequency component, u is slow-time time component, f_{dc} is the Doppler chirp rate difference between A and B. τ_{BA} is the time delay difference between A and B. $\bar{P}(f)$and $\bar{M}_A(u)$ are normalized range signal power spectrum and normalized azimuth signal envelope respectively. $p(\tau_{BA})$ and $m_A(f_{dc})$ are Inverse Fourier Transform (IFT) transformation of $\bar{P}(f)$and $\bar{M}_A(u)$.

Rewritten using coordinate vector, Eq. (2.23) could be rewritten as [49]:

$$\chi(A,B) \approx e^{\left(j2\pi \frac{[\Phi_{TA}+\Phi_{RA}]^T(\overrightarrow{B-A})}{\lambda}\right)} p\left(\frac{2\cos\left(\frac{\beta}{2}\right)\Theta^T(\overrightarrow{B-A})}{c}\right) m_A\left(\frac{2\omega_E \Xi^T(\overrightarrow{B-A})}{\lambda}\right) \quad (2.24)$$

where operation T stands for vector transposition, $\overrightarrow{B-A}$ stands for a vector from A to B, Θ is the unit vector in the direction along the bisector of β , ω_E and Ξ are the equivalent angular speed and direction respectively. λ is the radar wavelength.

The range resolution and azimuth resolution denoted by δ_τ and δ_a respectively are written by:

$$\delta_\tau = \frac{0.886c}{2\cos(\beta/2)B} \quad (2.25)$$

$$\delta_a = \frac{0.886\lambda}{\omega_E T_{dwell}} = \frac{0.886\lambda}{\theta_{TA}} \tag{2.26}$$

where B is the bandwidth of ranging signal and $\theta_{TA}$is the rotation angle of platforms relative to target.

Inspection of Eq. (2.25) and (2.26) indicates that, on one hand, the range resolution is highly dependent on bistatic angle, i.e., the larger the bistatic angle is, the poorer the range resolution will be. If bistatic angle is zero, where the monostatic case applies, Eq. (2.25) will become $\delta_r = \frac{0.886c}{2B}$, which coincides with classical range resolution expression in [75]. On the other hand, the azimuth resolution is inversely proportional to rotation angle of platforms relative to target. In the stationary receiver case, rotation angle is accredited only to the transmitter movement. There will be no azimuth resolution if the satellite is flying perpendicular to the X-Y plane toward point A, where the rotation angle of transmitter is always zero. The following texts show the simulation results of both range and azimuth resolution in case of two representative stationary receiver BSAR configuration, i.e. 'quasi-monostatic' geometry and general geometry. The illustration of Two-dimesional (2-D) bistatic geometry for simulation is shown in Fig. 2.9.

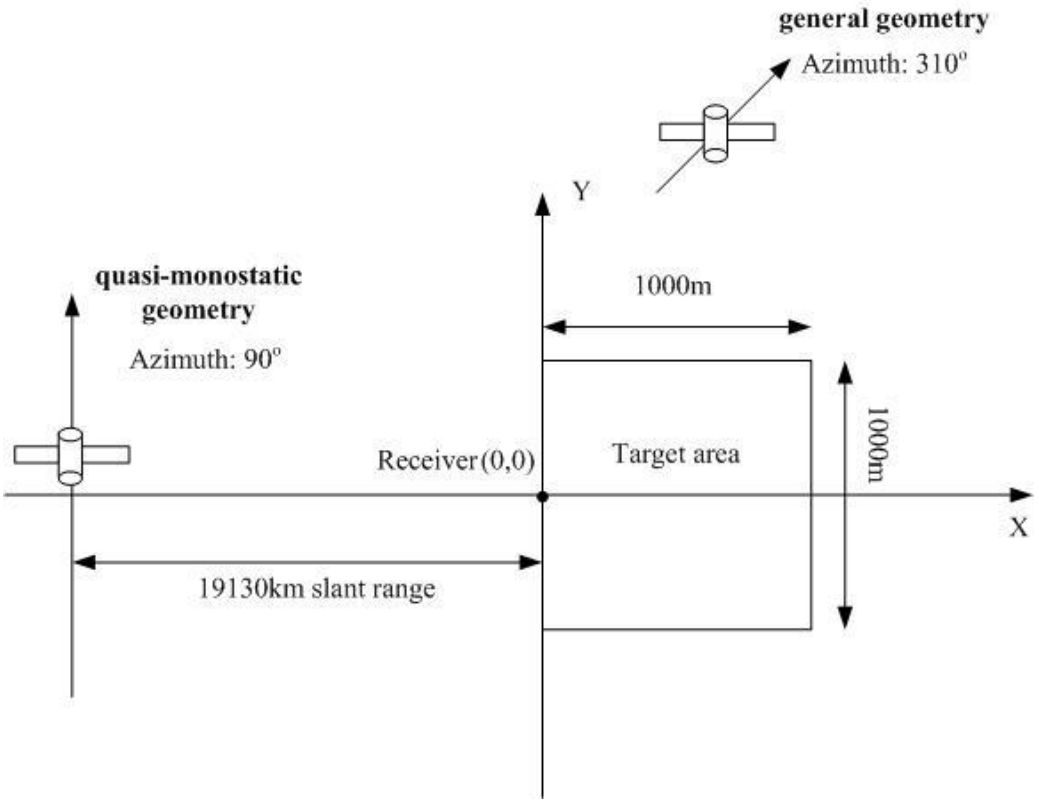

Figure 2.9: 2-D SS-BSAR configuration [74]

In Fig. 2.9, Receiver is located at grid coordinate origin, pointing to the positive X axis. Target area is a 1000m×1000m square, whose left side coincides with Y axis. Quasi-monostatic case is a kind of bistatic configuration that the satellite's synthetic aperture center is on the extension line of target to receiver, and its flying path is perpendicular to this line. It can be observed that in such configuration, transmitter and receiver are at the same side of target area, allowing small bistatic angle. General case has the same content with that defined in [4] i.e. transmitter is flying in arbitrary path. It is noteworthy that the satellite azimuth marked in Fig. 2.9 is measured at synthetic aperture center with regard to Y axis.

Fig. 2.10 shows the simulated range and azimuth resolution results for both geometries mentioned above. It could be observed that range resolution of quasi-monostatic geometry (Fig. 2.10(a)) is symmetric for upper part and lower part, as

expected, due to its symmetric bistatic configuration along X axis. In general geometry, however, it is not the case (Fig. 2.10(c)). Moreover from (a), the range resolution becomes better approaching X axis due to decreasing bistatic angle when the target is located closer to X axis. Comparing range resolution values between quasi-monostatic geometry and general case shows that better range resolution can be obtained by SAR acquisition in quasi-monostatic geometry, where the bistatic angle is less compared to general case.

With regard to the azimuth resolution, little variation is observed for both quasi-monostatic geometry (Fig. 2.10(b)) and general case (Fig. 2.10(d)) for a whole target area. These results are expected, due to that in both types of geometries, the Doppler variations are dominated by transmitter movement relative to target location. Since large difference of transmitter-to-target range against targeting size, given a ratio of 20000km to 1000m, the Doppler variation for the whole area will be trivial.

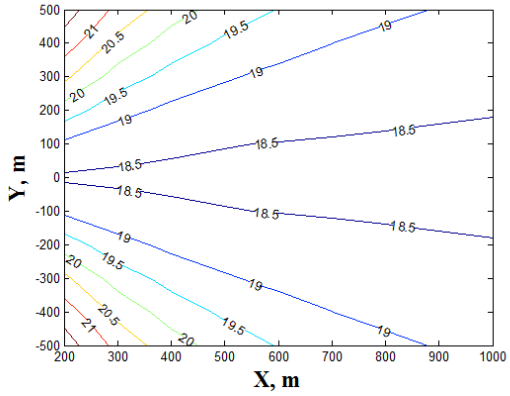

(a)

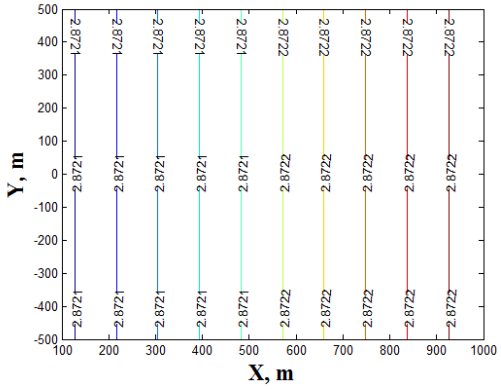

(b)

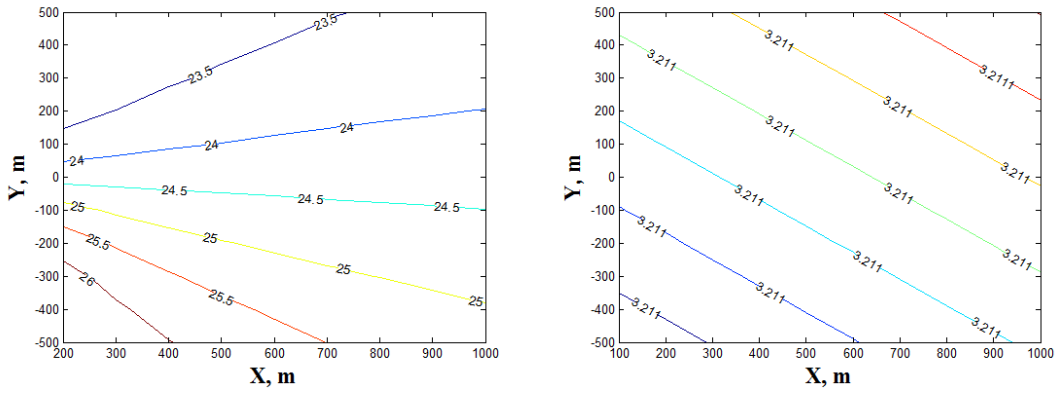

(c) (d)

Figure 2.10: (a) Range resolution of quasi-monostatic geometry, (b) Azimuth resolution of quasi-monostatic geometry, (c) Range resolution of general geometry, (d) Azimuth resolution of general geometry

B. Ambiguity function for BSAR with GNSS and stationary receiver at long integration time

In the case of long integration time SS-BSAR, the transmitter trajectory is no longer linear. Eq. (2.23) will be not valid and a modified formula for GAF is given by Liu [63].

$$\chi(A,B) = e^{(j2\pi f_c \tau_{BA})} \int P\left(\tau_{BA} + \frac{f_{dc}}{f_c} \cdot u\right) \widetilde{M}_A(\bar{u}) e^{(j2\pi f_{dc} u + j\pi f_{dr} u^2)} du \qquad (2.27)$$

where the parameters have the same meaning with those of Eq. (2.23). f_{dr} is Doppler Centroid variation between A and B.

Comparing Eq. (2.27) to (2.23), separation of this formula into range and azimuth cannot be found directly, as azimuth variation is coupled with range variation in $P\left(\tau_{BA} + \frac{f_{dc}}{f_c} \cdot \bar{u}\right)$, while in Eq. (2.23), it is not at all.

In terms of definition of range and azimuth resolution, it is well known that range resolution is defined when Doppler variation of neighbouring targets is zero, i.e.

$f_{dc} = 0$, and azimuth resolution is defined when time delay difference of neighbouring targets is zero, i.e. $\tau_{BA} = 0$. Following this, the range and azimuth resolutions are given by [64]:

$$\chi_r(A,B) = P(\tau_{BA})\left|\widetilde{M}_A(u)e^{(j\pi f_{dr}u^2)}du\right| \tag{2.28}$$

and

$$\chi_a(A,B) = \left|\int P\left(\frac{f_{dc}}{f_c}\cdot u\right)\widetilde{M}_A(\bar{u})e^{(j2\pi f_{dc}u + j\pi f_{dr}u^2)}du\right| \tag{2.29}$$

The modified ambiguity function for long dwell time has been verified using simulation and experimental data. The experiments used the same equipments and signal processing algorithm as described in Chapter 3, 4 and 5. Two experiments of different dwell time duration, i.e. 5 minutes and 10 minutes were conducted to verify our proposed formula and indicate increasing difference when dwell time becomes longer. The experimental equipment and set-up are the same with prototype experiment in chapter 5.

Fig. 2.11 shows the theoretical and experimental image for 5 minutes dwell time. Comparison of the responses demonstrates that apart from little difference at side-lobe between old and new formulas, others are quite identical. Moreover, high level similarity between theoretical and experimental results can be observed, suggesting that both old algorithm and new algorithm are valid at 5 minute dwell.

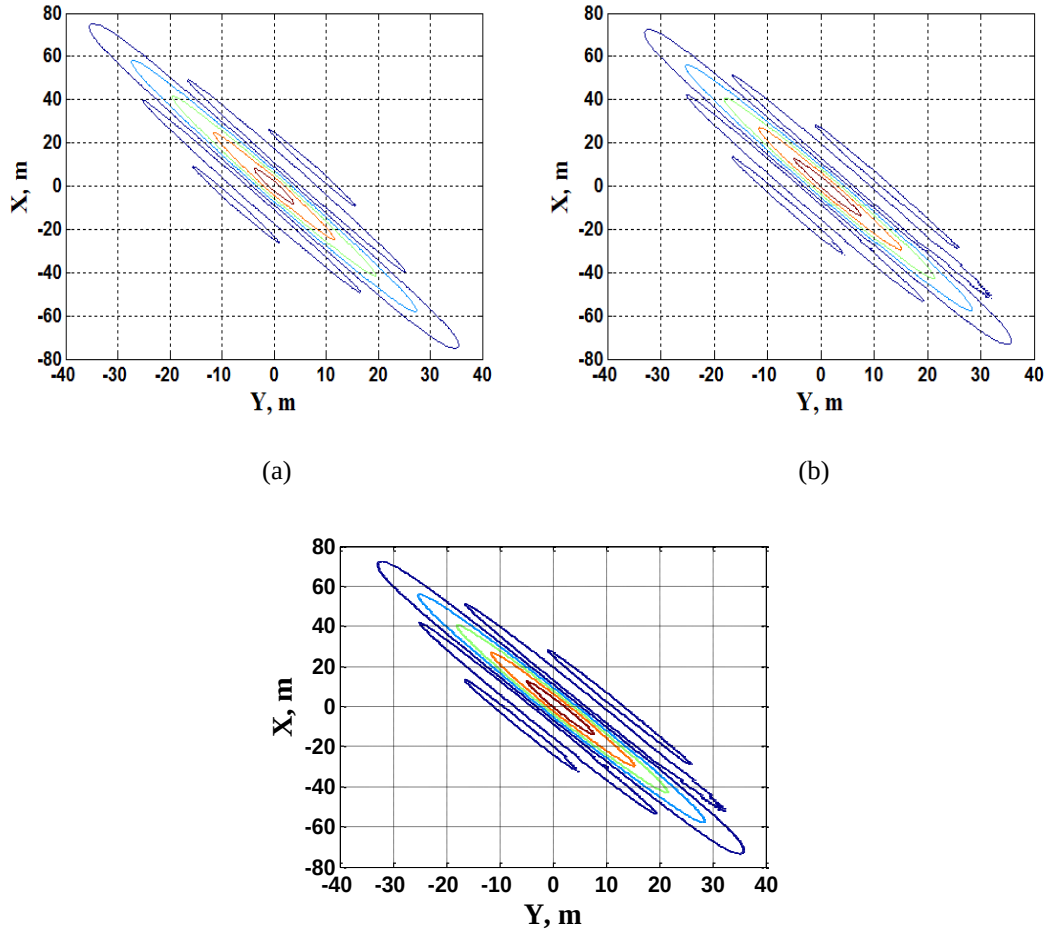

(a) (b)

(c)

Figure 2.11: Results for 5 minutes dwell time: (a) Ambiguity function from old formula, (b) Ambiguity function from new formula, (c) Experimental image [64]

Fig. 2.12 shows the corresponding results for 10 minutes dwell time. Observation of these PSFs found significant difference between old PSF (Fig. 2.12(a)) and new PSF (Fig. 2.12(b)) in terms of mainlobe size (i.e. the mainlobe of old PSF is narrower than new one), while new PSF has high coincidence with experimental PSF (Fig. 2.12(c)). The comparison well verifies the validity of Eq. (2.27).

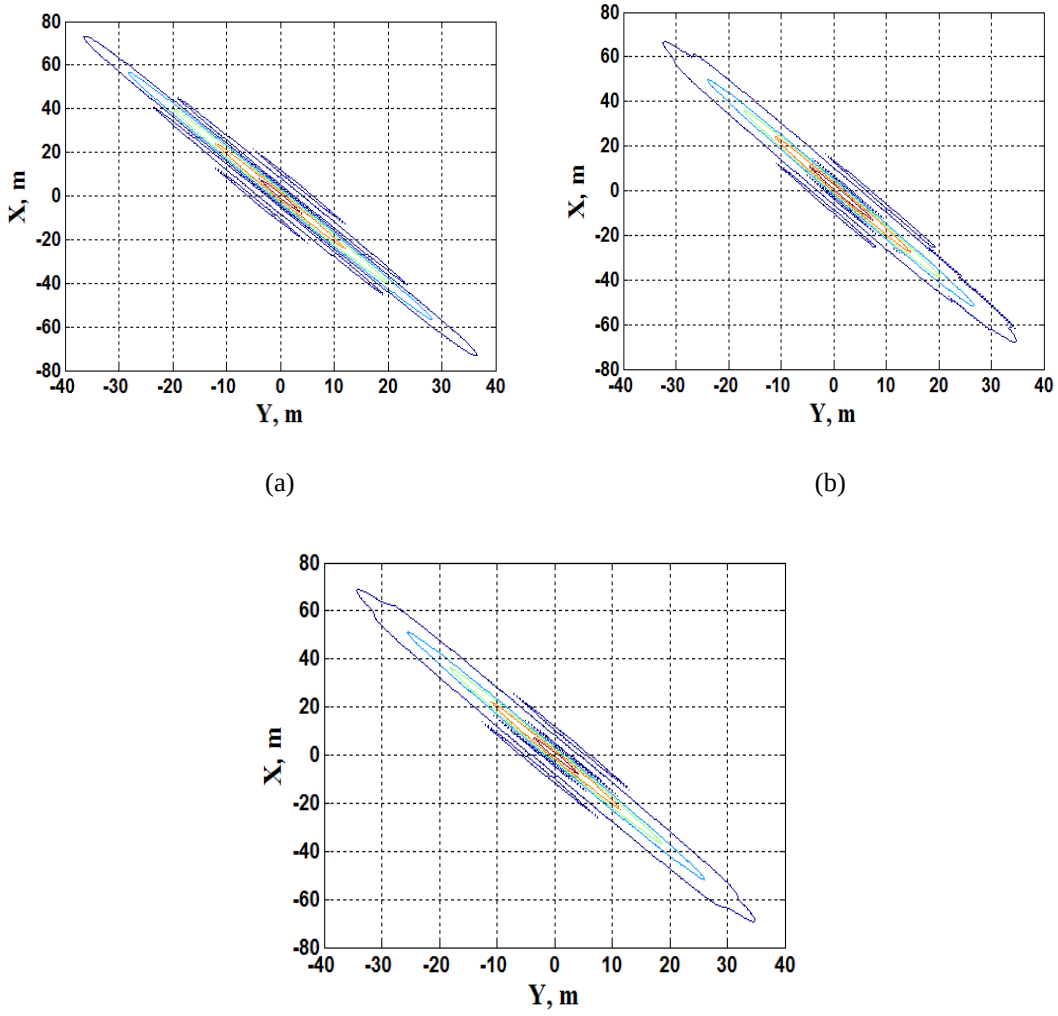

Figure 2.12: Results for 10 minutes dwell time: (a) PSF from old formula, (b) PSF from modified formula, (c) Experimental PSF [64]

Finally, the range and azimuth resolution comparison by using old formula, proposed formula and experimental result measured at corresponding PSF plots at different dwell time is examined.

Inspection of Fig. 2.13(a) justifies the validity and necessity of proposed formula for GAF calculation, especially when the dwell time is longer than 5 minutes. It can be observed that range resolution using old formula is almost a constant value with dwell time and have more deviation with experimental value as the dwell time increases.

This is expected, due to that range resolution is affected by both fast-time and slow-time variations in Eq. (2.28). In contrast, azimuth resolutions obtained from old formula, new formula and experimental measurement have high agreement with the dwell time changing. This is also expected due to that the second order term of phase in Eq. (2.29) can be neglected even if dwell time (u) is large.

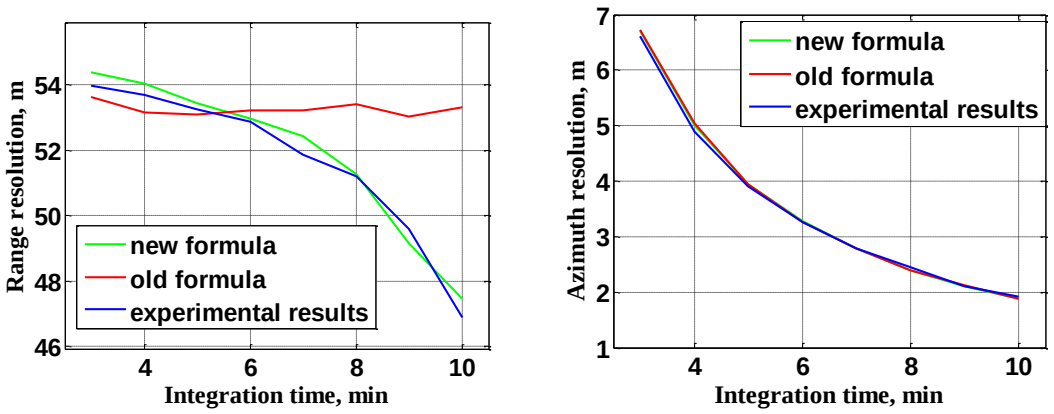

(a) (b)

Figure 2.13: Comparison among old formula, proposed formula and experimental results for (a) Range resolution, (b) Azimuth resolution [64]

This section described the classical bistatic resolution solution and extended PSF equation in the case of long dwell time. The simulation of classical resolution shows that, in small target area such as our case, range resolution and azimuth resolution will not vary much. In addition, the optimal range resolution is achieved at quasi-monostatic case. An extended PSF formula has been derived for long dwell time bistatic SAR. It has been verified both theoretically and experimentally that the novel formula become more effective if the dwell time is larger than 5 minutes, where the classical formula will not be valid, and especially for range resolution.

2.6 Conclusion

This chapter provides a systematic coverage of SS-BSAR with GNSS and a stationary receiver including satellite parameters, transmitted signal, receiver hardware prototype and radar performance. Among three global navigation satellite systems, GLONASS was chosen as our transmitter. The receiver was a self-built low cost RF receiver. The power budgets of both HC and RC were analyzed. Simulation has proved that our system can see signals up to the order of kilometres. With regard to resolution, a new PSF model has been proposed at long dwelling time. A simulation and real experiment have been applied to verify its better performance than old one, especially when the dwelling time is beyond 5 minutes.

CHAPTER 3

SIGNAL SYNCHRONIZATION

3.1 Introduction

An important problem inherent in bistatic radar system is synchronization between transmitter and receiver. In monostatic radar, the transmitter and receiver are mounted together, using the common oscillator source. In bistatic radar system, however, the geometric separation of transmitter and receiver makes it necessary to consider the phase errors introduced by two independent frequency sources employed. Due to the radar signal processing is a coherent approach, therefore, it is required that, for bistatic radar system, the transmitter and receiver must be synchronized.

Synchronization in a BSAR could be classified into three categories which we call spatial, time, and Doppler/phase synchronisation. Spatial synchronization ensures that both the transmitting and receiving antenna illuminates the same area of interest simultaneously. Time synchronisation is required so that the time of measurement is accurately known or recorded (in order to provide spatial synchronisation, or extract

co-ordinates for image formation etc.). Doppler/phase synchronization maintains coherence between the transmitter and the receiver.

In SS-BSAR with GNSS, spatial synchronization is not required due to the large satellite antenna footprint. However, time and Doppler/phase synchronization are absolutely essential. During the motion of a platform, the instantaneous time and Doppler and phase of the transmitted signal with respect to a fixed point on the ground vary. However, these parameters are affected by the fact that the transmitter and receiver do not share the same clock and local oscillator. This means that the true instantaneous time delay is corrupted by clock slippage between the transmitter and receiver clocks, whereas the true phase measurements are affected by local oscillator drift. Unless compensated, these effects lead to range and azimuth phase errors, which can cause severe image defocus, as well as shifts to the target's true location [76]-[84]. This problem is even more acute for SS-BSAR with GNSS and a fixed receiver, since in this configuration long dwell times are required to achieve a sufficiently high azimuth resolution. As the dwell time increases, oscillator drifts and clock slippage become increasingly more severe.

The purpose of signal synchronization is to provide a time delay/Doppler/phase reference for the received signal, so that at its output clock slippage and oscillator drift are removed. Solutions to the signal synchronization problem for BSAR have been proposed by a number of authors. Tian etc. [85][86] used phase locked loops (PLL) to track the Doppler and phase of the direct signal. Wang etc. [87]-[89] used GPS-based techniques to achieve time and phase synchronization on dedicated BSAR platforms. Lopez etc. [90]-[92] performed signal synchronization for SS-BSAR with Envisat as the transmitter and a fixed receiver. The common factor in all of the

reported research is the fact that signal synchronization is performed on signals emitted from radar satellites. The signals they emit are chirp signals with significant power levels. This means that in some cases it may even be possible to extract the direct signal time delay and phase without any complex signal processing.

The approaches described above are not applicable to passive SS-BSAR with GNSS. The first reason is that the GNSS ranging signals are much more complex than the chirp radar signals. The second reason is that the power level of GNSS signals in the target area is significantly less than that of imaging radar signals. Even if a dedicated receiver channel is built to record the direct satellite signal with an antenna pointed towards the satellite, the signal-to-noise ratio (SNR) at the output of the antenna can be as low as -40 dB [93]. This means that tracking algorithms particular to GNSS are required to maximize SNR before any information is extracted.

For the above reasons, signal synchronization based on GNSS signal tracking for navigation purposes is a more suitable approach for the proposed topology. The concept behind this is that in order for GNSS to provide positional information, the propagation delay, Doppler and phase from the received signal need to be tracked in order to extract the navigation message of the satellite anyway. There is a multitude of literature on this topic. Elliot, Nel and Tsui [94]-[96] report the use of hardware-based tracking techniques using delay lock loop, frequency lock loop and phase lock loop for acquisition and fine parameter tracking in real-time. However, processing in our case is done offline, and therefore the added hardware complexity is unnecessary. For this reason, software-based techniques such as those described by Tsui [96] are more desirable.

Saini etc. from University of Birmingham developed a synchronization algorithm in 2006, aiming at moving receiver SSBSAR with GLONASS signal processing [59][60]. This algorithm is based on the Block Adjustment of Synchronizing Signal (BASS) algorithm [96] to detect the delay, Doppler, phase and navigation message of the received GLONASS signal. The algorithm was verified by experimental testing and led to the first passive SS-BSAR image with GNSS as transmitters of opportunity. However, this algorithm was computationally expensive. In the moving receiver case, the computational burden was not so obvious due to the relatively small integration time, which was around 30-40s. Nevertheless, as mentioned before, integration times are at least ten times longer for the stationary case in order to generate the same azimuth resolution so processing times were significantly increased.

The motivation of this chapter comes from the points mentioned above. Although synchronization techniques for bistatic radar/SAR are well developed, none of them fits our passive GNSS-based system. Moreover, the already existing algorithm for this purpose is inefficient. As such, it is necessary to develop a new synchronization algorithm with considerable efficiency and flexibility to respond to the requirements of our system.

This chapter presents a newly developed synchronization algorithm for passive SS-BSAR with GNSS transmitters of opportunity. The generic algorithm can be applied to any GNSS satellite, by taking into account the differences in their ranging signals. Section 3.2 briefly introduces the coordinate processing, which is the part of synchronization and also essential for image formation. It is consisted of transmitter and receiver coordinates extraction, coordinate interpolation and transformation.

Section 3.3 describes the concept of signal synchronization in general. Then in Section 3.4 it outlined the previous algorithm [60] used for SS-BSAR. Sections 3.5 and 3.6 contain detailed descriptions of the adjustments to the generic algorithm for SS-BSAR with GLONASS and Galileo as the transmitters, respectively. Each Section presents the ranging signals used, as well as analytical derivations of the algorithms. Section 3.7 presents the synchronization results of GLONASS and Galileo using experimental data. Both contains existing algorithm results and proposed algorithm results. Conclusion for this chapter is mentioned in section 3.8.

3.2 GLOASS synchronization algorithm overview

3.2.1 Coordinate processing

Coordinate defines the positions of transmitter, receiver and targeting objects relative to a reference point. It is essential and important for signal synchronization and image formation for radar system. High precision coordinate ensures accurate synchronization outputs and high quality target response focusing (assuming other aspects are correct). The coordinate processing consists of three steps: coordinate extraction with time alignment, Coordinate transformation and Coordinate interpolation. The flow-chart applied to SS-BSAR system is shown in Fig. 3.1.

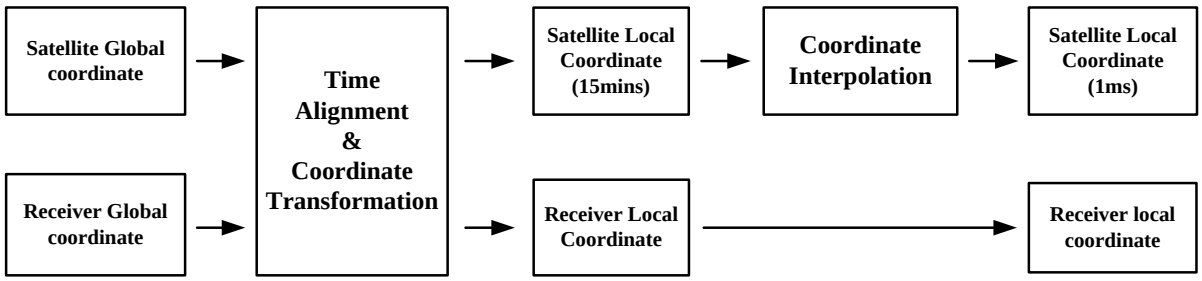

Figure 3.1: Coordinate processing flow-chart for SS-BSAR

Satellite coordinate and receiver coordinate raw data were extracted at the first place. Satellite coordinate is obtained from International GNSS Service (IGS) resource [97], sampled at interval of 15 minutes, and receiver coordinate could be read from handset GPS receiver. Both data sets are in global Cartesian format, where the origin of the coordinate is defined at mass center of the Earth, XY-axis aligns with the equatorial plane, and the X-axis is along the prime meridian. It is noteworthy that data sets from different resource may have different time standard, for example, IGS coordinate is in Coordinated Universal Time (UTC) time standard [98], while World Geodetic System 84 (WGS84) is in GPS time standard [99]. As such, satellite and receiver coordinates will be aligned where necessary.

The next step is coordinate transformation. The idea behind is that due to image is usually formed and presented at local coordinate frame, which is defined relative to the location of observation. Coordinate transformation from global data set to local counterpart is required. Helmert algorithm is applied in our system for such a purpose, the details of Helmert algorithm is in Appendix B

Finally, it could be understood from Chapter 2 that the PRI applied in our system equals to the code length at 1 millisecond. As such, interpolation of raw data will be implemented to up-sampling it from 15 minutes interval to 1 millisecond. In our case, Lagrange interpolation and power polynomial fitting were performed on satellite coordinate. The analytical expressions of them are enclosed in Appendix C.

On completion of these three steps, the translated coordinates of satellite transmitter and receiver will pass through to the synchronization and image formation stages.

3.2.2 Received signal model

The signal received in the HC is a long, continuous stream of data. After quadrature demodulation, it can be written as [74]:

$$s(t) = P[t-\tau(t)]D_P[t-\tau(t)]e^{[j(\omega_d(t)t+\phi(t))]} + j \times C[t-\tau(t)]D_c[t-\tau(t)]e^{[-j(\omega_d(t)t+\phi(t))]} \quad (3.1)$$

In Eq. (3.1), τ is the instantaneous signal propagation delay, ω_d is the Doppler frequency associated with the relative motion between the satellite and the HC, and ϕ is the signal overall phase information. We will consider the phase term more closely later on in the analysis.

For SAR processing, the HC signal in Eq. (3.1) is divided and reformatted into 2-D data array with a proper PRI of 1ms. This signal can be written as a function of fast-time (t_n) and slow-time (u) as:

$$s(t,u) = P[t_n-\tau(u)]D_P[t_n-\tau(u)]e^{[j(\omega_d(u)t_n+\phi(u))]} + j \times C[t_n-\tau(u)]D_c[t_n-\tau(u)]e^{[-j(\omega_d(u)t_n+\phi(u))]} \quad (3.2)$$

Here t_n is from 0 to 1ms and u is in the range from –T/2 to T/2, T is the integration time.

3.2.3 Synchronization concepts

This Section describes the generic method for finding the HC signal parameters to be used for synchronization in SS-BSAR with GNSS transmitters. These parameters are the direct signal time delay, Doppler and phase. If the GNSS signal contains a navigation message, which is the message navigation satellites transmit for positioning information, then the synchronization algorithm should extract it.

The principle of using the direct signal to provide synchronization is used in most bistatic SAR systems. However, in SS-BSAR with GNSS the process of extracting the required parameters is essentially different. What is also different is the way the synchronization parameters are used as a reference for the RC.

In conventional BSAR systems, either the transmitting or the receiving platform (or both) are radar platforms. One of the implications in such a configuration is that both the direct and reflected signal powers are significantly high. In many cases this allows a direct measurement of some parameters through techniques like signal envelope detection, or even a direct comparison between the direct and reflected signals to extract any receiver artefacts.

This is not possible in our system. Based on the signal power and our receiver parameters, the SNR is -17 and -16 dB for GLONASS and Galileo [74], respectively. Since the signal is buried under noise, a tracking algorithm based on matched filtering should be used as a basis for estimating the direct signal delay, Doppler and phase at the HC. On the other hand, the RC cannot be used at all for parameter estimation, since the SNR is sufficiently high at the output of the image formation algorithm, i.e. after 2-D SAR processing.

After tracking the HC parameters, the delay, Doppler and phase errors are found by comparing the tracked parameters to the ones theoretically predicted from the transmitter and receiver coordinates. These errors are removed from the RC using a matched filtering operation in the range direction. Since this operation is a correlation in the range direction, it can be combined with the range compression step of any image formation algorithm. The signal used to compress the RC data is a locally

generated signal which contains the tracked errors found from the HC, the tracked delay and any possible navigation message. This is done because of the high noise level corrupting the received HC signal. Since oscillator drift is common to both channels, it is removed at the output of this stage. Note that it is not necessary to extract the HC delay errors. The time delay of the local signal is the tracked delay, which contains the nominal signal delay plus clock slippage. Since clock slippage is common to both channels, at the output of the range compression it is removed, and the delay in the RC is measured relative to the signal delay of the HC.

It should be noted here that even though the need for synchronization and its general concept are the same regardless of the GNSS used, the signal structure of different GNSS systems is very different, so the particular tracking algorithm needs to be tailored accordingly and this gives rise to different challenges.

3.3 Existing synchronization algorithm

As mentioned before, different GNSS systems have different signal structures. However, their signal structures have some common factors. Each satellite ranging signal is usually the combination of two pseudo-random sequences with a Phase Shift Keying (PSK) modulation, called the spreading codes. It is also possible, but not necessary as we will see later on, for the ranging signal to be modulated by a navigation message used for positioning, which is also a PSK signal. From these three signals, only one has a bandwidth wide enough to be used for radar purposes. That is one of the spreading codes, which we will refer to as the primary code. The other spreading code will be referred to as the secondary code. The generic tracking algorithm attempts to estimate the delay, Doppler and phase of the desired code. The

delay is easy to track if a filter matched to the code is used. The problem lies in the Doppler and phase tracking. That is because the phase of the primary code does not only contain propagation phase delay from the transmitter to the receiver. It also contains phase transitions due to the combination of the primary code with the secondary code and the navigation message.

This problem is not new in communications engineering, and in fact this is where the original synchronization algorithm [60] was derived from. This algorithm used communication signal processing techniques to track the parameters of the unwanted spreading code and the navigation message. As soon as these parameters were estimated, the unwanted codes were removed. Any navigation message present was decoded by looking at the overall tracked phase. Upon removal, the parameters of the desired code were tracked with a high degree of precision. Delay tracking was performed using a software-based Delay-Locked Loop (DLL), whereas the frequency and phase were tracked using BASS method. A block diagram of this algorithm is shown in Fig. 3.2.

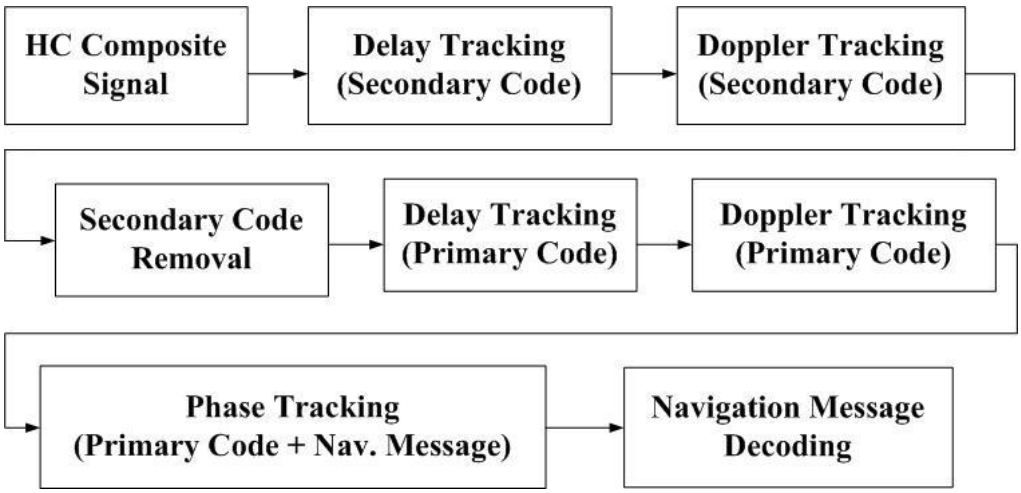

Figure 3.2: Conventional synchronization algorithm block diagram

This algorithm was found to be very accurate and contributed to high-quality imagery for the moving receiver SS-BSAR case, where dwell times are in the order of 30-40s. However, due to the fact that it was based on communications engineering principles, it involved tracking and decoding three signals (the two spreading codes and the navigation message), whereas for radar imaging only one signal was needed. Moreover, the BASS algorithm is a frequency search algorithm. Since the maximum Doppler expected from GNSS is a few tens of kHz [74], this meant a significantly large search window. Thus, even though highly accurate, the algorithm was computationally expensive. This effect was found to be more severe in the fixed receiver case, where dwell times are at least ten times longer.

3.4 Proposed synchronization algorithm

The Proposed synchronization algorithm focuses on the radar outputs which are necessary for imaging, while at the same time taking into account the GNSS signal peculiarities. That is, the delay, Doppler and phase of the spreading code used for imaging only. The generic block diagram of the algorithm is shown in Fig 3.3.

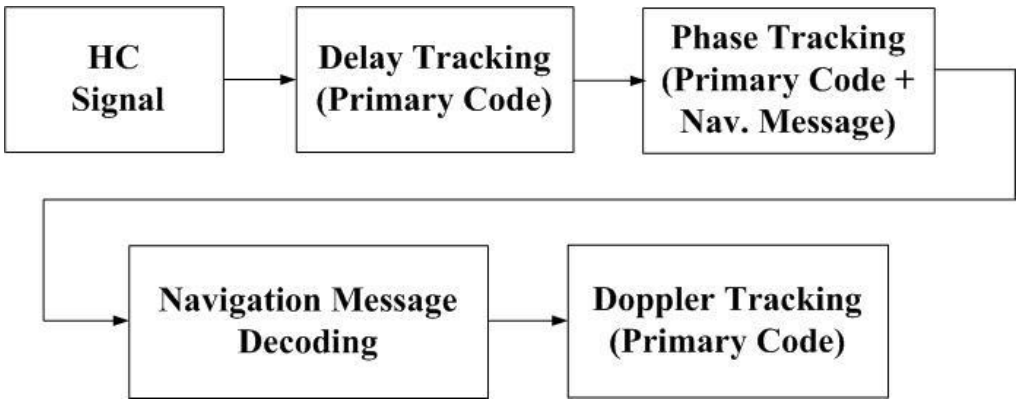

Figure 3.3: Generic block diagram of new synchronization algorithm

The algorithm is based on the fact that both spreading codes are pseudo-random and the navigation message is random, and therefore they are mutually uncorrelated. This

means that after matched filtering is used on the desired code, the other two signals have properties equivalent to noise or, more strictly speaking, interference. At the output of the matched filter, the code has been compressed in range and the signal delay can be estimated from the location of the correlation peaks. Signal delay consists of propagation time delay plus clock slippage effects.

The phase in the range correlation peaks consists of propagation phase delay, which varies smoothly with slow-time, phase errors due to oscillator drift, and abrupt phase transitions (ideally 180 degrees) due to the presence of the interfering signals. Phase transition removal is achieved by an appropriate phase threshold which varies with slow-time, and is aided by the expected signal phase history, derived from the transmitter and receiver positions. This eliminates the need for a frequency search algorithm such as BASS. It should be noted here that use of the instantaneous transmitter-receiver positions implies that synchronization should be done offline. This is not a restriction for the previous tracking algorithm.

The description provided above aimed to provide a general overview of the new tracking algorithm. Of course, adjustments for the different GNSS have to be made. In the following Sections, we will present the tracking algorithms developed for GLONASS as well as Galileo.

A block diagram of the algorithm for GLONASS synchronization is shown in Fig. 3.4.

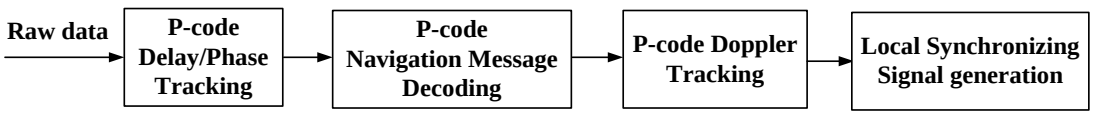

Figure 3.4: Block diagram of new synchronization algorithm for GLONASS

In the previous algorithm, the Doppler frequency of the P-code was calculated via the C/A-code. The coarse frequency tracking step was the most computationally expensive step, since it was a two-dimensional search algorithm tracking the C/A-code in delay with a coarse frequency span of 20 kHz, in accordance with the maximum Doppler expected from a GNSS satellite [96].

In the new algorithm, we skip the C/A code synchronization and track the P-code directly. The instantaneous P-code delay at each PRI is obtained by matched filtering in the fast-time direction. The phase of the range-compressed signal includes the instantaneous P-code propagation phase delay, phase errors and phase transitions due to the P-code navigation message. A phase transition detector can decode and remove the navigation message. Finally, the phase errors can be identified by comparing the tracked phase history to the theoretically expected phase history. The P-code Doppler can then be found from the instantaneous phase difference between adjacent PRIs.

Each block of the algorithm in Fig. 3.4 is described in detail in the following sub-Sections.

3.4.1 P-code delay tracking and phase extraction

The first step in the algorithm is range compression of the HC signal at each PRI. The concept of range compression is the convolution between HC signal and conjugated time-reversed locally generated P-code in time domain. In practice, however, it is implemented in the frequency domain (Fig. 3.5).

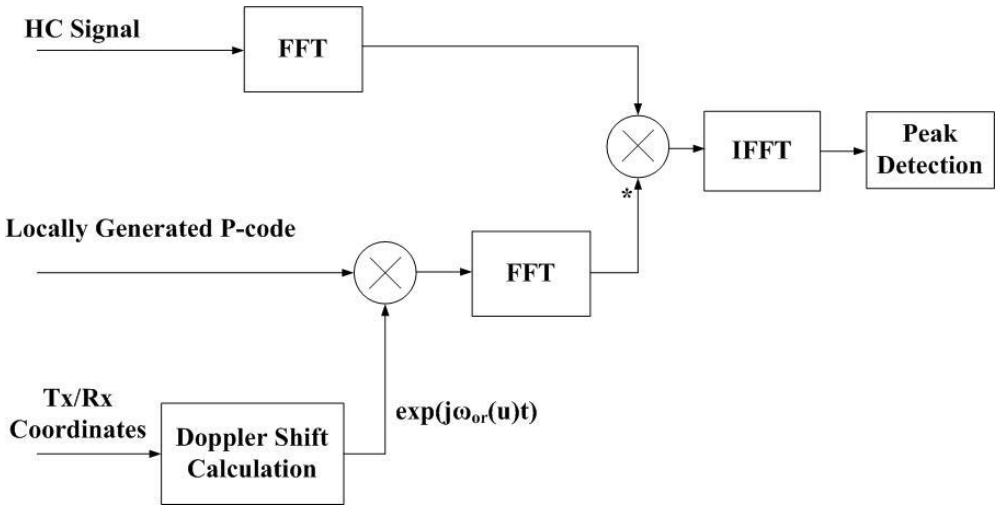

Figure 3.5: Block diagram of frequency domain range compression

The reference function for the range compression is a locally generated P-code, which is shifted in Doppler. The added Doppler shift is calculated from the instantaneous transmitter and receiver co-ordinates. The purpose of the added Doppler is to provide a better matching between the received (Eq.(3.1)) and reference waveforms and to simplify phase tracking and discrimination.

The reference signal could be expressed as:

$$s_{ref}(t_n, u) = P(t_n)e^{[j(\omega_{or}(u)t_n)]} \tag{3.3}$$

where ω_{or} is the coordinate estimated Doppler frequency in each PRI.

The correlation between the received HC signal and the reference signal could be written as:

$$\begin{aligned} C(t_n, u) &= s(t_n, u) \circledast s_{ref}(t_n, u) \\ &= CF_P[t_n - \tau(u)]D_P[t_n - \tau(u)]e^{[j(\omega_e(u)t_n + \phi(u))]} \\ +j \times P(t_n)e^{(j\omega_{or}(u)t_n)} &\circledast C[t_n - \tau(u)]D_C[t_n - \tau(u)]e^{[-j(\omega_e(u)t_n + \phi(u))]} \end{aligned} \tag{3.4}$$

where $CF_P[t_n - \tau(u)]$is the cross-correlation function between received signal (P-code part) and local generated P-code. $\omega_e = \omega_d(u)-\omega_{or}(u)$. In practice, the maximum ω_e found has been 50 Hz. The first term in (3.4) is the range-compressed P-code, with the added Doppler/phase errors and the navigation message. The second term is the correlation between the P-code and the C/A-code. Since these two codes are pseudo-random sequences, they are mutually uncorrelated. Even though the correlation between the two signals is not zero in practice, its level is quite low and will therefore be neglected hereafter. This means that Eq. (3.4) can be simplified as:

$$C(t_n, u) = s(t_n, u) \circledast s_{ref}(t_n, u)$$

$$= CF_P[t_n - \tau(u)]D_P[t_n - \tau(u)]e^{[j(\omega_e(u)t_n+\phi(u))]}$$

$$= CF_P[t_n - \tau(u)]e^{[j(\omega_e(u)t_n+\phi_P(u)+\phi_e(u)+\phi_n(u))]} \quad (3.5)$$

note that in Eq. (3.5), the navigation message D_P has been expressed as a phase function ϕ_n. This is because the message is a Binary Phase Shift Keying (BPSK) signal, and therefore its values (1 or -1) can be thought of as a phase change of +180 or -180 degrees.

The location of the correlation peak in Eq. (3.5) gives us an estimate of the instantaneous P-code delay $\tau(u)$. Looking at the exponential factor, we can state that the correlation peak contains four individual phase terms. The first one, $\omega_e(u)t_n$ varies linearly with time. However, a maximum ω_e of 50 Hz gives a maximum phase of 2.8 degrees at $t_n = 1$ms (the end of the PRI) and can therefore be neglected. The second term, $\phi_p(u)$, is the nominal phase history. The third term, $\phi_e(u)$, encompasses all types of phase errors, these are due to oscillator drift, atmospheric errors etc. It is the term we want to estimate so we can remove it from the RC data. The final term,

$\phi_n(u)$, is associated with the navigation message. The next steps in the algorithm aim to discriminate between these phase terms and extract them. Since these phase terms are extracted from the peak of the compressed pulse, phase noise is low (-24 dB)(Fig. 3.6) and therefore will be neglected in future calculations.

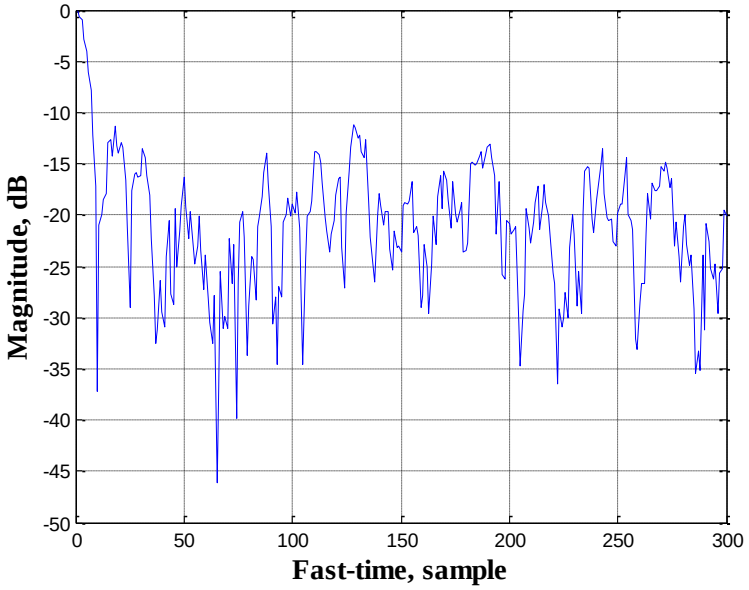

Figure 3.6: Range compressed HC signal

3.4.2 Phase error extraction and navigation message decoding

Following range compression, the tracked phase at the peak of each compressed pulse is extracted via:

$$\Phi(u) = \tan^{-1}\left\{\frac{Im\{C[\tau(u),u]\}}{Re\{C[\tau(u),u]\}}\right\} \tag{3.6}$$

From Eq. (3.5), Eq. (3.6) can be written as:

$$\Phi(u) = \omega_e(u)t_n + \phi_p(u) + \phi_e(u) + \phi_n(u) \approx \phi_p(u) + \phi_e(u) + \phi_n(u) \tag{3.7}$$

What is required is to discriminate between the phase errors given by the second term and phase transitions given by the third term of Eq. (3.7). This can be of specific use if one wants to analyse the phase errors individually, or to decode the navigation

message and extract positioning information. To do this, we first take the phase difference between adjacent azimuth positions (or PRIs), i.e.:

$$\Delta\Phi(u) = \Phi(u + PRI) - \Phi(u\ ) = \Delta\phi_p(u) + \Delta\phi_e(u) + \Delta\phi_n(u) \qquad (3.8)$$

The phase difference is computed because it allows an easier detection of phase transitions due to the navigation message. If adjacent navigation bits have a different polarity, the resulting phase transition is 180 or -180 degrees. If the polarity is the same, there is no phase change.

An example of $\Delta\Phi(u)$ is shown in Fig. 3.7 for experimental data. In this figure phase transitions due to the navigation message are clearly visible. Smaller phase fluctuations are due to $\phi_e(u)$. By detecting the location of the phase transitions, we can establish the form of the navigation message. To detect the transitions, a detection threshold is set, shown as the dashed line in Fig. 3.7. This detection threshold is defined by $\Delta\phi_p(u)$ plus a constant of $\pi/2$.

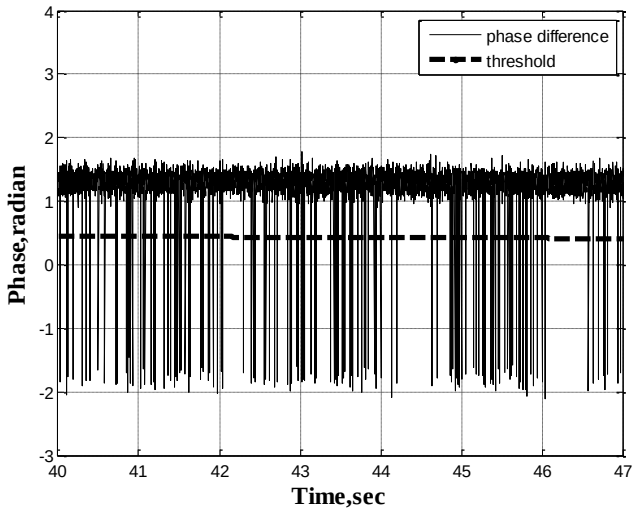

Figure 3.7: Tracked phase difference and threshold for navigation bit decoding

To sum up, the overall phase difference curve is following a smooth line during the integration time, however, if there is a navigation message change, a obvious peak will occur. We could decode the navigation message by following these big spikes.

Up to now, the signal delay, Doppler, phase and navigation message of heterodyne channel have all been extracted. Synchronization between transmitter and receiver could be achieved by generating a local reference signal with all the parameters. This part is peculiar to our system compared with any other BSAR or monostatic SAR system in terms of range compression in stage of image formation. We would like to introduce it in Chapter 4, where the image formation for GNSS based SS-BSAR is detailed.

3.4.3 Computational complexity of old and new algorithms

Here, we give an overall analysis of computational complexity of old and proposed synchronization algorithms, based on our own developed software platforms. Suppose one complex multiplication and one complex addition both occupy one operational count. Then N-order Fast Fourier Transform (FFT) and Inverse Fast Fourier Transform (IFFT) required $Nlog_2N$ complex additions and $0.5Nlog_2N$ complex multiplications [101], which sums up to occupy $1.5Nlog_2N$ operational counts. The numbers of sum/subtract and FFT/IFFT by using old algorithm and new algorithm for one PRI data are listed in Table 3.1.

Algorithm type	Operation type	Secondary code tracking	Primary code tracking
Old algorithm	Sum/Subtract/ Multiplication/Division	$\frac{55}{6}N - \frac{1}{3}$	$4N$
	FFT/IFFT	3	6
New algorithm	Sum/Subtract/ Multiplication/Division	0	$2N$
	FFT/IFFT	0	3

Table 3.1: Number of sum/substract and FFT/IFFT in old and new algorithms

where N is the sampling point number at one PRI, which is equal to 50000. It is noteworthy that the factional number appeared in old algorithm secondary code tracking is due to longer data ($6PRI$ data) required for fine Doppler tracking [60].

Therefore, for M minutes data, the total operational counts by using old and new algorithms can be given by

$$CC_{old} = 790000 \times M \times N + 810000 \times M \times Nlog_2N - 20000M \quad (3.9)$$

$$CC_{new} = 120000 \times M \times N + 270000 \times M \times Nlog_2N \quad (3.10)$$

In our experiment, given the dwelling time is 5 minutes, the operational counts for old algorithm and new algorithm are 3.36×10^{12} and1.08×10^{12}. It could be observed that, from theoretical point of view, new algorithm is more than three times fast than old one. The real measurement will be provided from experiment in section 3.4.4.

3.4.4 GLONASS signal synchronization experimental result

The GLONASS raw data used to demonstrate synchronization was acquired on the roof of school of Electrical, Electronic and Computer Engineering of UOB. The experiment parameters are listed in Table 3.2:

Parameter	Value
Transmitting satellite	GLONASS COSMOS 737
Signal carrier frequency	1601.4375MHz
*Satellite's azimuth angle	80^{o}-72.3^{o}
*Satellite's elevation angle	42.9^{o}-43.5^{o}
Ranging signal bandwidth	5.11MHz
Integration time	600s

Table 3.2: GLONASS experimental parameters

* Satellite azimuth angle is measured with regards to North direction, while its elevation angle is measured relative to location of observation

Fig. 3.8 shows the GLONASS signal synchronization outputs using new algorithms. Fig. 3.8(a) shows the estimated Doppler history calculated from transmitter and receiver positions. Fig. 3.8(b) shows the tracked P-code delay. It can be observed that the tracked delay is a smooth line, indicating time delay of every PRI was well tracked. The ellipsoids in Fig. 3.8(c) indicates the phase shift of tracked slow-time signal within a arbitrary duration, which was resulted from navigation message. It can be seen from Fig. 3.8(d) that, due to navigation message, the signal spectrum is severely corrupted. The results of navigation message decoding and removing are shown in Fig. 3.9. Ellipsoids in Fig. 3.9(a) illustrate the cross sections between phase difference and set threshold, indicating the positions of navigation bits. Decoded

navigation messages at corresponding positions are shown in Fig. 3.9(b). After removing navigation messages, the phase becomes periodic without transition (Fig. 3.9(c)). The full slow-time signal spectrum after navigation message removal is shown in Fig. 3.9(d). Subsequently, the Doppler will be estimated as the difference of neighbouring phase after navigation bits removal (Fig. 3.9(e)). The variation in the Doppler result is observed, this is due to C/A code as interference and various receiver noise.

Comparing Fig. 3.8(d) and Fig. 3.9(d), it can be observed that after navigation message removal, the signal spectrum is flat top shape, implying a chirp like signal in time domain. In addition, comparing between Fig. 3.8(a) and Fig. 3.9(e), it could be found that there is a nearly constant offset between estimated Doppler and tracked Doppler. This offset may be due to hardware clock slippage and atmosphere artefacts. Nevertheless, it could be cancelled in range compression stage described in Chapter 4.

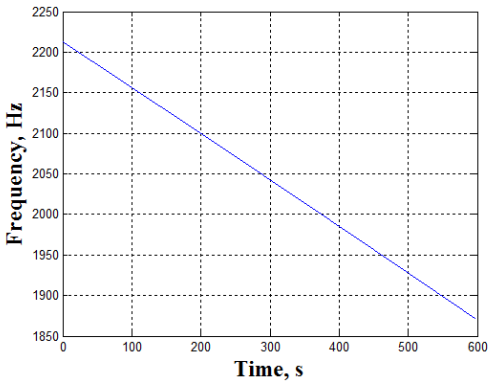

(a)

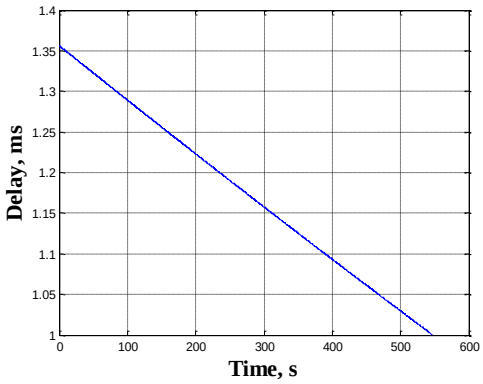

(b)

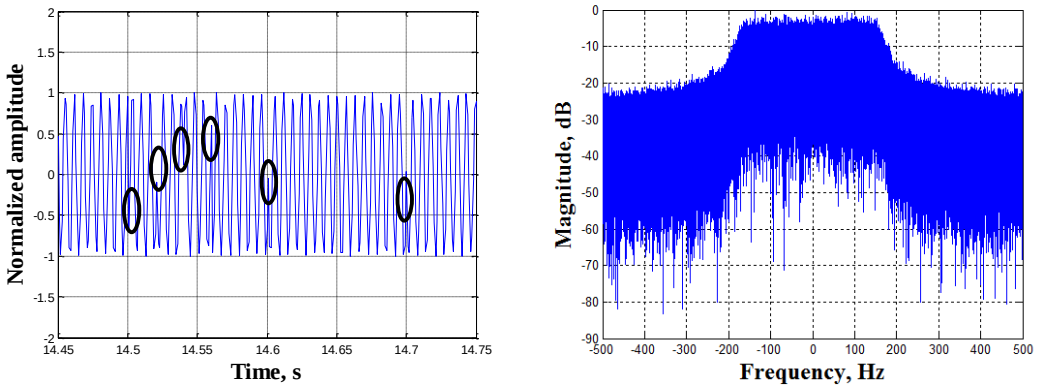

(c) (d)

Figure 3.8: Synchronization results of new algorithm (a) Estimated Doppler history from coordinates, (b) Tracked P-code delay, (c) Tracked P-code slow-time phase with navigation message, (d) Tracked P-code slow-time signal spectrum with navigation message

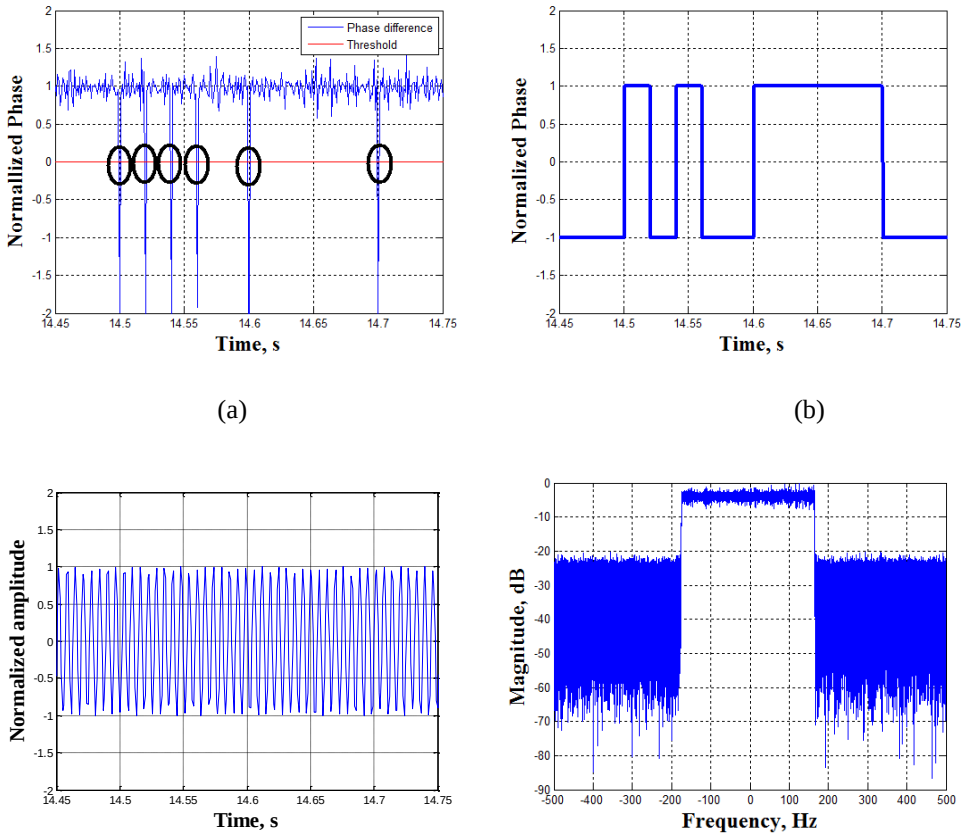

(a) (b)

(c) (d)

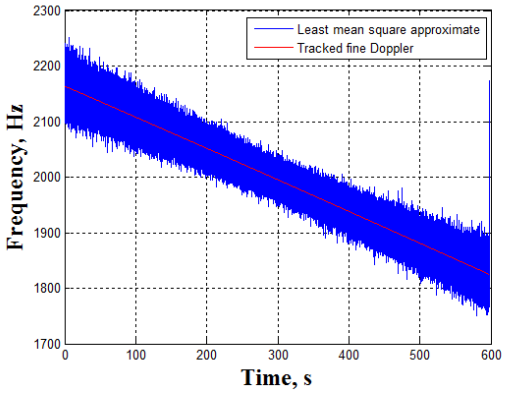

(e)

Figure 3.9: Synchronization results of new algorithm (a) Tracked P-code phase difference and threshold, (b) Decoded navigation message, (c) Tracked P-code slow-time phase without navigation message, (d) Tracked P-code slow-time signal spectrum after removing navigation message, (e) Tracked P-code Doppler

Next we examine the synchronization results comparison between old and new algorithm. Fig. 3.10(a) – (c) shows the difference of tracked P-code delay, Doppler and slow-time signal spectrum after navigation message removal. It could be found that there are trivial differences between old and new synchronization outputs. Due to the old algorithm has been fully calibrated [60], it could be concluded that the new algorithm ensures good performance.

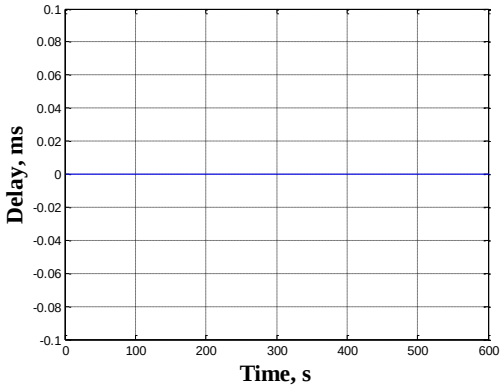

(a)

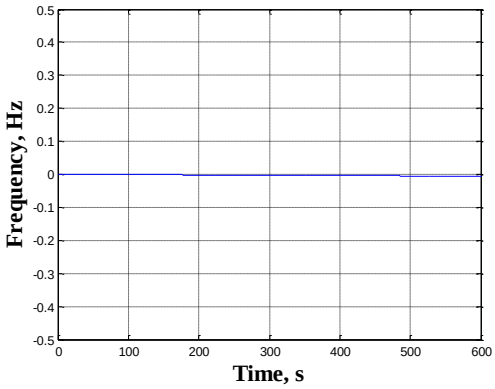

(b)

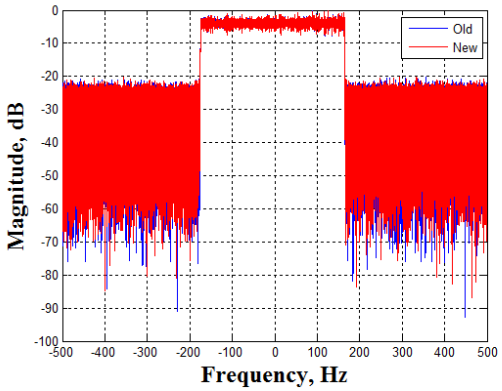

(c)

Figure 3.10: Synchronization results from old and new algorithms (a) Tracked P-code delay, (b) Tracked P-code Doppler, (c) Tracked P-code slow-time signal spectrum after removing navigation message

Regarding computational complexity, old algorithm took 29 hours, while new one only took 8.5 hours, which is more than 3 times faster than old one, accords with our theoretical expectation.

Based on the tracked parameters from both synchronization algorithms, two local synchronizing signals were generated to compress the HC data in range. Following this operation, two images were generated using the same back-projection algorithm (will be detailed in Chapter 4). The experimentally obtained PSFs were also compared to the theoretically expected one for this imaging scenario (Fig. 3.11). This PSF was calculated using Eq. (2.27) in Chapter 2.

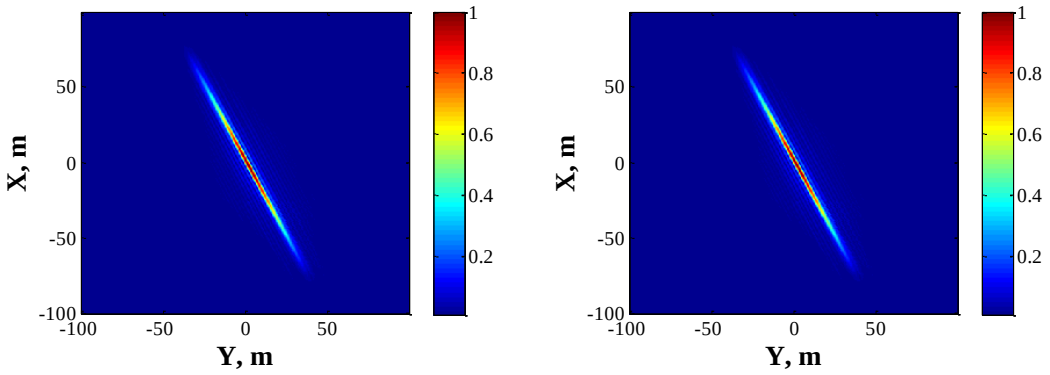

(a) (b)

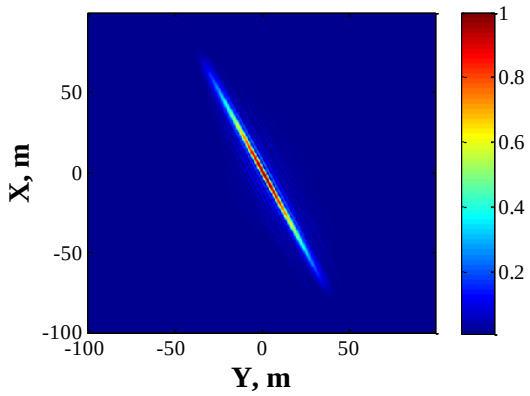

(c)

Figure 3.11: PSF obtained using (a) Old algorithm, (b) New algorithm, (c) Theoretical formula

Comparison of both experimentally obtained PSFs with theoretically expected one indicates proper focusing. Moreover, the two experimental PSFs are identical, indicating validity of the new approach.

3.5 Synchronization algorithm extended to Galileo

3.5.1 Algorithm description

The Galileo transmitted signal structure is described in Appendix D. In receiver part, E5a and E5b signals are separated by applying different local oscillator in hardware part due to different carrier frequency of these two signals. The received E5b-Q signal in HC after quadrature demodulation could be expressed as (see Appendix D):

$$s(t_n,u) = -S_{E5b-Q}[t_n-\tau(u)]e^{[j(\omega_d(u)t_n+\phi(u))]}$$
$$= -P[t_n-\tau(u)]S[t_n-\tau(u)]e^{[j(\omega_d(u)t_n+\phi(u))]} \quad (3.11)$$

where $P[*]$ is primary code and $S[*]$ is secondary code. Other parameter definitions are aligned with those in Eq. (3.2).

Primary code and secondary code should be looked as an entity when forming imaging, however, for synchronization, due to random allocated secondary code sequence, secondary code should be tracked at beginning. The block diagram of Galileo signal synchronization by new algorithm is shown in Fig. 3.12:

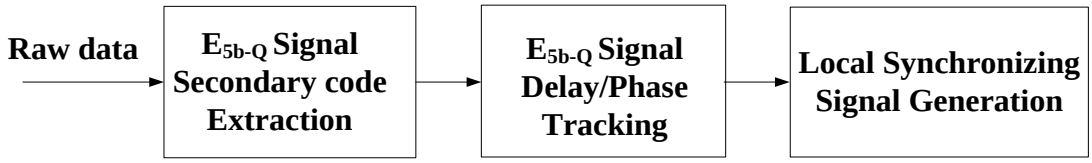

Figure 3.12: Block diagram of new synchronization algorithm for Galileo

The synchronization of Galileo signal is a little different of that of GLONASS signal due to different signal properties. It consists of three steps:

1. Find the secondary code.

The philosophy behind finding E5b-Q signal secondary code as the first step is as follows: Our pulse width is 1ms, unlike navigation message with bandwidth of 50 Hz, the secondary code with bandwidth of 1000 Hz will seriously deteriorate tracking due to possible phase shift of every PRI.

So it is essential to find its starting position for signal descrambling. In this stage, one dimensional matched filter between received signal and local generated secondary code with cycling shift varying from 1bit to 100 bits will tell the secondary code.

2. After stripping of secondary code, signal delay and phase tracking could be obtained by matched filtering between received raw data and local generated $E_{5b\text{-}Q}$ signal with Doppler shift by calculation from coordinates.

3. Local synchronizing signal could be generated with the same method in GLONASS part.

3.5.2 Galileo signal synchronization experimental result

The Galileo data used to demonstrate Galileo signal synchronization was acquired on the roof of School of Electrical, Electronic and Computer Engineering of UOB. Same as above, only HC signal synchronization is demonstrated here. It should be noted that E5b-Q signal is used for tracking due to absence of navigation message and can decrease the processing complexity.

The experimental parameters are listed in Table 3.3

Parameter	Value
Transmitting satellite	Galileo GIOVE-A
Signal carrier frequency	1207.14MHz
*Satellite's azimuth angle	44^o-50^o
*Satellite's elevation angle	73^o-74^o
Ranging signal bandwidth	10.23MHz
Integration time	2 minutes
Estimated slow-time Doppler bandwidth	43Hz

Table 3.3: Galileo experimental parameters

*Satellite position has the same meaning with that in Tab. 3.2

Fig. 3.13(a) – (f) show the Galileo signal synchronization results using new algorithm. Fig. 3.13(a) shows the estimated Doppler history of received SAR raw data resulted from satellite motion relative to receiver. Fig. 3.13(b) is the tracked secondary code.

Fig. 3.13(c) and (d) are tracked delay and slow-time signal real part. Fig. 3.13(e) and (f) are tracked slow-time signal spectrum and tracked Doppler.

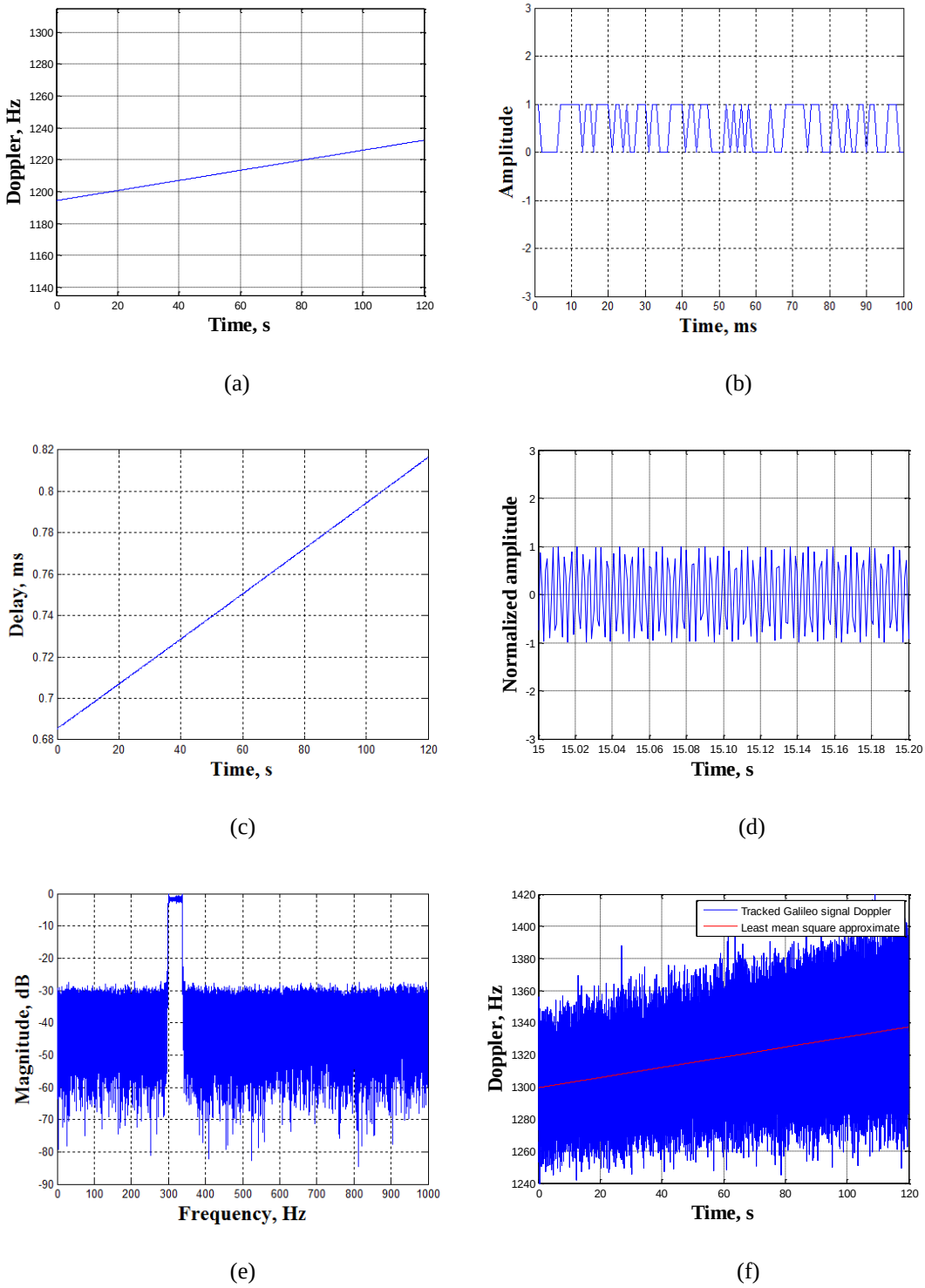

Figure 3.13: Synchronization of new algorithm (a) Estimated Doppler history from coordinates, (b) Extracted secondary code, (c) Tracked Galileo signal delay, (d) Tracked Galileo signal slow-time phase, (e) Tracked Galileo signal slow-time signal spectrum, (f) Tracked Galileo signal Doppler

It is instructive to compare synchronization outputs from old and new algorithm for performance evaluation. Fig. 3.14 shows the delay difference, Doppler difference and slow-time signal spectrum comparison. Little variations are observed between old and new results.

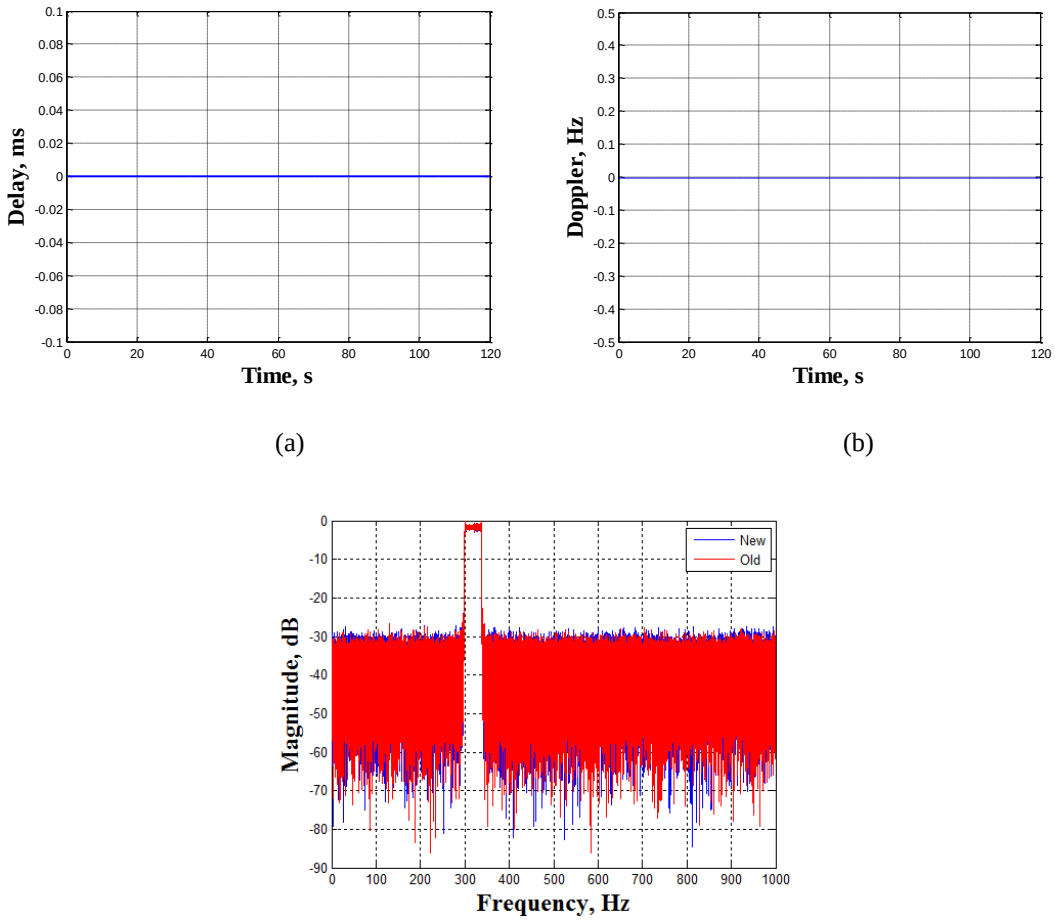

(a) (b)

(c)

Figure 3.14: Synchronization results from old and new algorithms (a) Tracked Galileo signal delay, (b) Tracked Galileo signal Doppler, (c) Tracked Galileo signal slow-time signal spectrum after removing navigation message

Regarding algorithm efficiency, the processing time using old algorithm and new algorithm are 5.78 hours and 1.70 hours.

It is, however unfortunate that up to now the Galileo coordinates with sufficient accuracy have not been publicly released. Therefore testing synchronization algorithm through final imaging products as in the GLONASS case is not possible. However, in the GLONASS testing, it was found that if the old and new synchronization results coincides, so do the imaging outputs, therefore, by observing the similarity of the synchronization outputs of two algorithms above, the same imaging performance can be expected.

3.8 Conclusion

This article presented a new generic signal synchronization algorithm for SS-BSAR with GNSS transmitters and a fixed receiver. The generic algorithm can be applied to any GNSS transmitter, by taking into account the different GNSS signal properties. In this paper, signal synchronization algorithms were derived for the GLONASS and Galileo systems. Moreover, in theory it can be applied to any type of receiver, moving or stationary, as it is independent of the delay/Doppler dynamics. The proposed approach was tested using experimental data and compared to a previously derived algorithm. Both synchronization algorithms were compared on the basis of their synchronization outputs, as well as the final image products yielded where appropriate. The new algorithm was found to have the same level of high accuracy as the previous one, but being more than three times faster.

CHAPTER 4

IMAGE FORMATION ALGORITHM

4.1 Introduction

Bistatic SAR image formation algorithm has been developed and discussed for decades. It can be divided into two categories: time domain algorithm and frequency domain algorithm.

The time domain algorithm derives from original thoughts of forming the image by direct 2-D matched filter between raw data and conjugate of replica of echo signal [102], which is known as Time Domain Correlation (TDC) algorithm. It gives the best reconstruction accuracy. Sometimes, a faster variant, called Back Projection (BP) algorithm is used alternatively. Instead of performing 2-D correlation pixel by pixel, BP achieves block-by-block range compression for every azimuth bin before azimuth matched filter implemented.

The time domain algorithm has good phase preservation and is exempt from bistatic geometry limit. However, such algorithms suffer from high computational loads, due to their processing is based on point-to-point.

The need to improve processing efficiency exploits frequency domain image formation algorithms, where block efficiency has been achieved. Taking into account of the algorithm limit, the frequency domain algorithms could be classified into several categories. Some methods converts bistatic data to equivalent monostatic data before a classical monostatic processing algorithm being applied to form bistatic image. The idea is to replace two platforms with a monostatic platform right in the middle of the baseline. The representative algorithm developed in such kind is called Dip Moveout (DMO) method [102][103]. Some algorithms translate two hyperbolic model of bistatic range history to single hyperbolic range history model before a monostatic algorithms being performed [104]. Mathematical manipulation and approximation are applied instead of raw data pre-processing mentioned above. By solving a multiple parameter equations, equivalent range history, velocity and squint angle will be obtained between bistatic and monostatic counterparts. Some develop apparent analytical 2-D point target spectrum and design proper matched filter according to the signal response in frequency domain [105]-[111]. The most representative methods are Loffeld Bistatic Formula (LBF) [105][109] and Method of Series Reversion (MSR) [106][111]. By applying Principle Of Stationary Phase (POSP), relationship between the Stationary Phase Point (SPP) and frequency component can be obtained. Substitute it to the 2-dimensional phase spectrum, we can arrive at apparent phase spectrum. The accuracy of this algorithm depends on the number of terms that expanded. Some use numerical calculation to obtain high precision 2-D spectrum [112]-[121]. All the frequency domain algorithms mentioned

above may largely improve the efficiency, however, they suffer from following drawbacks. Due to the 2-D spectrum is derived under proper approximation and expansion, the precision of 2-D spectrum depends on how real the approximation is and how many orders of expansion. Moreover, due to approximation, phase information may not be fully preserved after image focusing. In addition, those algorithms may not be valid if imaging scene is too large. This is due to 2-D spectrum is usually derived for the target at scene center, which may not accommodate targets far from scene center. Perhaps the most important issue is that those frequency domain algorithms cannot be used for translational variant geometry (definition in chapter 1). The most active period for the BSAR imaging algorithm development was from 2003 to 2009, while afterwards, SAR community have been concentrating on system development and verification [20,32,34,36,44,46].

To accommodate one-stationary configuration like us (belongs to translational variant geometry), a number of frequency domain algorithms are being discussed. They are sub-aperture Range-Doppler (RD) algorithm [122], improved Nonlinear CS (NLCS) [123][124] and modified Omega-K [125]. In sub-aperture algorithm, the full aperture has been divided into several sub-apertures where the straight line transmitter trajectory assumption in each is met. After its 2-D spectrum derived, signal is compressed by conventional RD algorithm. The drawback is its inadequacy in processing large scene imaging. Improved NLCS performs imaging by implementing a nonlinear scaling in range domain, while azimuth compression is implemented with fitted azimuth matched filter, followed by residual error compensation. It can handle large swath and large squint angle case, however, also suffers from high complexity in practical utilization. It is well noteworthy that, due to IFFT/IFT operation required

in frequency domain algorithm, the radar platform movement path is needed to be straight, otherwise, frequency domain will fail.

In SS-BSAR with GLONASS and stationary receiver, due to long integration time required to get sufficient SNR and satisfactory resolution, the transmitter is no longer assumed to be a straight line. Therefore, implementation of frequency domain algorithm is a challenge.

This chapter describes the modified BP algorithm used in stationary receiver SS-BSAR with GNSS transmission from both analytical and simulation level. Section 4.2 outlines the conventional back-projection theory and algorithm realization. Section 4.3 presents the geometry of fixed receiver SS-BSAR system and signal model. A mathematical description of bistatic BP implementation has been given step by step. Section 4.4 presents the fixed receiver SS-BSAR imaging simulation in two scenarios, followed by conclusion of this chapter in Section 4.5.

4.2 Back-projection algorithm overview

BPA was originally used in Computer-aided Tomography (CAT) technique for medical imaging [126]. Early stage of BP algorithm applications in SAR was used in monostatic spotlight SAR image focusing [127]. Recent years has witnessed the use of BP algorithm in bistatic spotlight and stripmap configuration [34]. The analytical expression of monostatic BP algorithm could be derived from TDC. Let's discuss how BP algorithm works analytically. The Illustration of monostatic SAR BP algorithm is shown in Fig. 4.1.

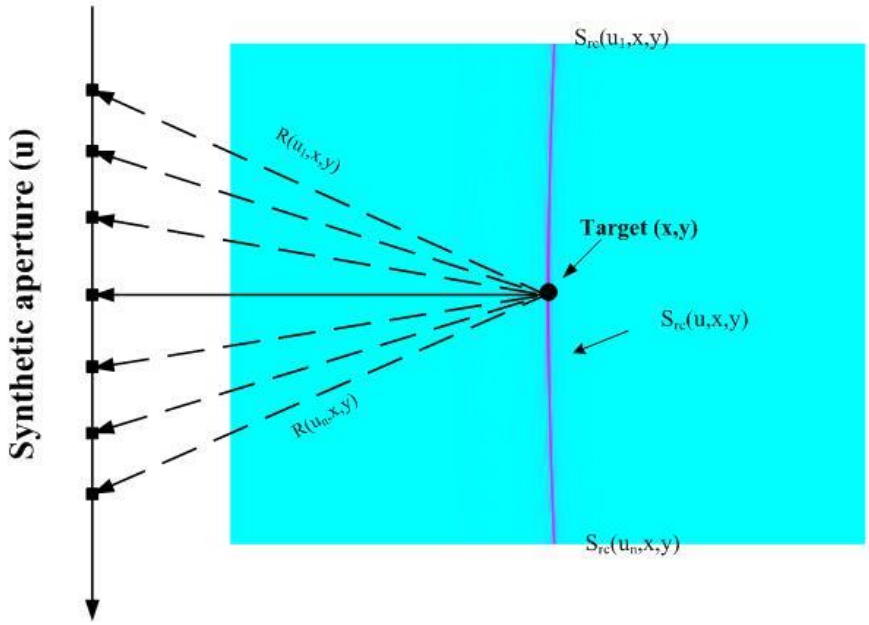

Figure 4.1: Illustration of monostatic SAR BP algorithm

In Fig. 4.1, the radar platform moves straight down. Green colour background represents the imaging area, where we assume there are a number of scatterers distributed randomly. Denote the transmitted signal $s(t,u)$, where t is fast time and u is slow time, the SAR signal received for an arbitrary point target scatter $(x,y,0)$is denoted as:

$$p[t-\frac{R(u,x,y)}{c}] \tag{4.1}$$

where $R(u,x,y)$ is the round-trip distance between radar and target.

The TDC processor correlates transmitted signal $s(t,u)$ with echo signal $p[t-\frac{R(u,x,y)}{c}]$. The output is the response at the target point (x,y), which could be written as:

$$f(x,y)=\int_u \int_t s(t,u)p^*[t-\frac{R(u,x,y)}{c}]\,dtdu \tag{4.2}$$

Let's have another look at Eq. (4.2), if we define range compressed signal as:

$$s_{rc}=s(t,u)*p^*(-t) \tag{4.3}$$

where * is convolution operation.

Combining Eq. (4.2) and (4.3), we obtain

$$f(x,y) = \int_u s_{rc}[\frac{R(u,x,y)}{c}, u]\, du$$

$$= \int_u s_{rc}[t_n(u), u]\, du \qquad (4.4)$$

where $t_n(u) = \frac{R(u,x,y)}{c}$ is the round-trip delay of the echo signal from target at (x, y).

Observation of Eq. (4.4) found that, target response of a target could be recovered by adding fast time back-projection curve in each slow time location. Figure 4.2 shows the block diagram of back-projection implementation:

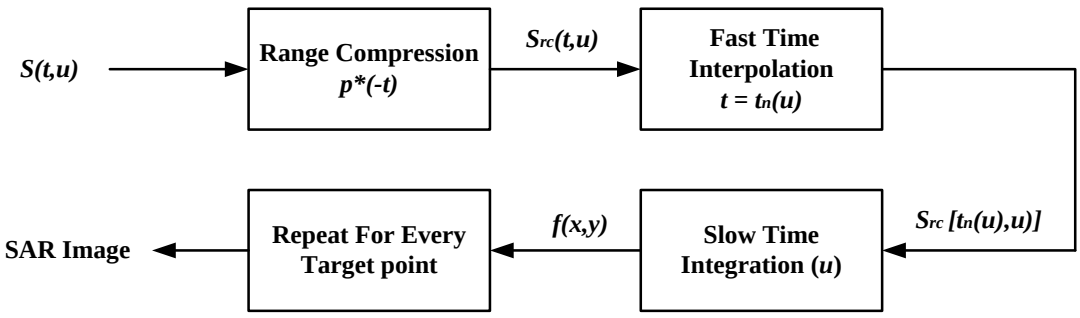

Figure 4.2: Block diagram of back-projection algorithm [75]

To implement BP algorithm in practice, range compression is performed on raw data for every azimuth bin. Then the range history for a target point is mapped to all range compressed signal by fast-time interpolation. Finally, the interpolated values on all the azimuth bins accumulate coherently to get the response of this target point. To form a full image, the processes mentioned above will be repeated for all the pixels in the scene.

The BP algorithm suffers from inefficiency as mentioned before. Assume we have Msamples along azimuth and the pixel number in the imaging scene is$(N \times N)$, then the total computational complexity will be $O(M \times N^2)$. Fast BP [128] has been discussed to improve processing efficiency, however, it's not used in this these and omitted here.

4.3 Back-projection algorithm for SS-BSAR with a fixed receiver

4.3.1 Geometry and received signal

The stationary receiver bistatic SAR geometry is shown in Fig. 4.3. Transmitter is flying along its orbit with average height of 20000km, which could be denoted as (x_t, y_t, z_t). Receiver is located at (x_r, y_r, z_r). The target area is within X-Y plane.

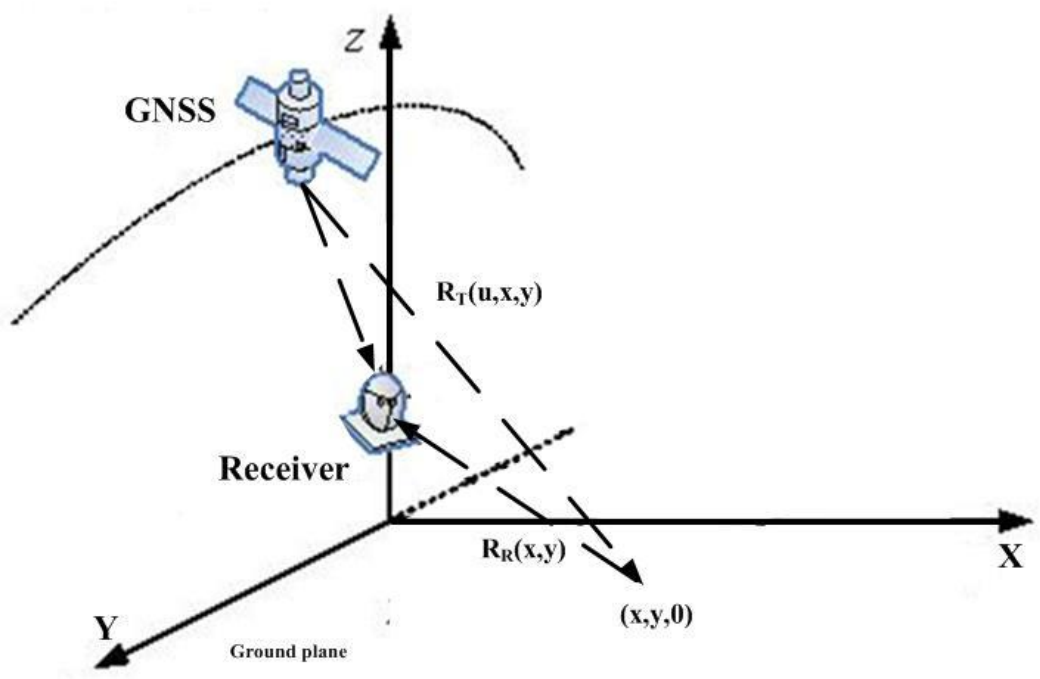

Figure 4.3: Geometry of SS-BSAR with GNSS and stationary receiver

Assume a point target is located at $(x, y, 0)$, the received signals reflected from this area after quadrature demodulation could be expressed in 2D format (fast-time (t) and slow-time (u)):

$$s(t,u) = P[t-\tau_2(u,x,y)]D_P[t-\tau_2(u,x,y)]e^{[j(\omega_{d2}(u,x,y)t+\phi_2(u,x,y))]} + j \times C[t-\tau_2(u,x,y)]D_C[t-\tau_2(u,x,y)]e^{[-j(\omega_{d2}(u,x,y)t+\phi_2(u,x,y))]} \quad (4.5)$$

where

$$\tau_2(u,x,y) = \frac{R_R(x,y)+R_T(u,x,y)}{c}$$

$$R_R(x,y) = \sqrt{(x_r-x)^2+(y_r-y)^2+z_r^2}$$

$$R_T(u,x,y) = \sqrt{(x_t-x)^2+(y_t-y)^2+z_t^2}$$

$$R_b(u,x,y) = \sqrt{(x_r-x_t)^2+(y_r-y_t)^2+(z_r-z_t)^2}$$

$$\phi_2(u,x,y) = \phi_{e2}(u,x,y) + \phi_{p2}(u,x,y)$$

$$\omega_{d2}(u,x,y) = \Delta\phi_2(u,x,y)/2\pi$$

τ_2 is the round-trip delay, R_R is receiver to target range, $R_T$is transmitter to target range, $R_b$is the baseline between transmitter and receiver. ϕ_2 and ω_{d2} are phase and Doppler of received signal, ϕ_{e2} and $\phi_{p2}$are phase noise and phase caused by wave propagation.

4.3.2 Image formation algorithm description

As BP algorithm is well known in SAR community, the emphasis of this Section is to show how the synchronized parameters are integrated into BP algorithm to get final image. Fig. 4.4 shows the block diagram of modified BP algorithm.

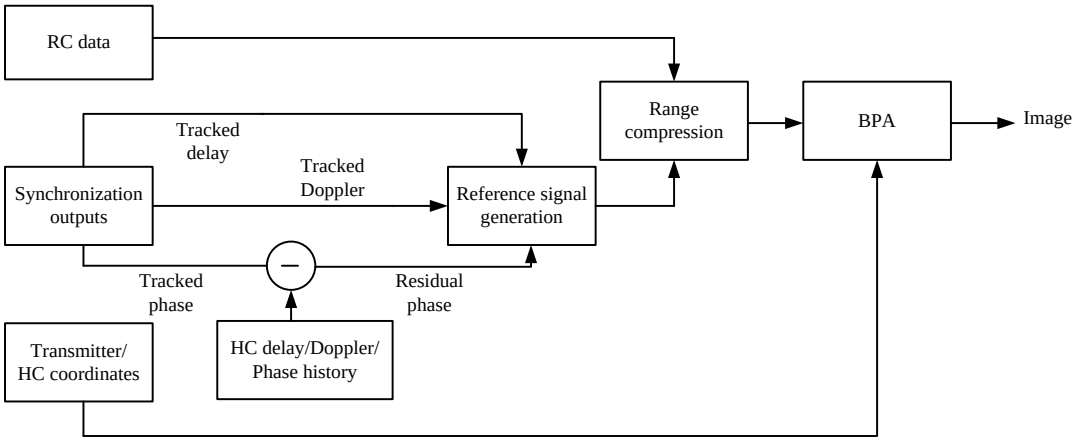

Figure 4.4: Block diagram of modified BP algorithm for SS-BSAR

The image formation algorithm consists of two steps:

A. Range compression

Range compression is the most essential and critical part of image formation in GNSS-based SS-BSAR system. The idea is to correlate receiver radar signal with properly designed local reference signal for every azimuth, to make signal compression at range direction while preserving the phase for azimuth compression. The local reference signal is generated using synchronization outputs (delay, Doppler, phase and navigation message) of HC signal.

$$s_{sync}(t_n, u) = P[t_n - \tau(u)]D[t_n - \tau(u)]e^{(j\omega_d(u)t_n)}e^{(j[\Phi(u)-\phi_p(u)-\phi_n(u)])} \quad (4.6)$$

where $\tau(u)$is the synchronized time delay of HC signal. $\omega_{or}(u)$is the coordinate calculated angle velocity. $\Phi(u)$is the tracked phase of HC signal. ϕ_p is the coordinate calculated phase and $\phi_n$is the tracked navigation message phase of HC signal.

According to Eq. (4.6), the local generated reference signal has the same delay of tracked HC signal delay, its Doppler frequency will be transmitter/HC antenna coordinate calculated Doppler history, and its phase term will be the output of

subtraction of tracked HC signal phase by coordinate calculated phase and tracked navigation message.

Using Eq. (3.7), the reference signal can be written in the other way.

$$s_{sync}(t_n, u) = P[t_n - \tau(u)]D[t_n - \tau(u)]e^{(j\,\omega_d(u)t_n)}e^{(j\phi_e(u))} \quad (4.7)$$

The signal after range compression between Eq. (4.5) and Eq. (4.7) could be written as:

$$s_{rc}(t, u) = s(t, u, x, y) \circledast s_{sync}(t_n, u)$$

$$= CF_P[t - (\tau_2(u, x, y) - \tau(u))] \times$$

$$e^{[j(\phi_{P2}(u,x,y)+\phi_{e2}(u,x,y)-\phi_e(u,x,y)+(\omega_{d2}-\omega_{d1})t_n+((\tau_2(u,x,y)-\tau(u))\pi)]}$$

$$+j \times P[t_n - \tau(t)] \circledast C[t - (\tau_2(u, x, y) - \tau(u))] \times$$

$$e^{[j(\phi_{P2}(u,x,y)+\phi_{e2}(u,x,y)-\phi_e(u,x,y)+(\tau_2(u,x,y)-\tau(u))\pi)]} \quad (4.8)$$

Note that the cross correlation of C/A code and P-code will be zero, second term in equation will disappear, only first term remains.

$$s_{rc}(t, u) = CF_P[t - (\tau_2(u, x, y) - \tau(u))] \times$$

$$e^{[j(\phi_{P2}(u,x,y)+\phi_{e2}(u,x,y)-\phi_e(u,x,y)+(\omega_{d2}-\omega_{d1})t_n+(\tau_2(u,x,y)-\tau(u))\pi)]} \quad (4.9)$$

There are four items in exponential terms:

The first item $\phi_{P2}(u, x, y)$ is the propagation induced phase history of one single target $(x, y, 0)$, which contributes the synthetic aperture to the image.

The second item $\phi_{e2}(u, x, y) - \phi_e(u, x, y)$ is the difference of phase errors caused by receiver noise, atmosphere artefacts, etc. between HC and RC. The value should be approximately zero due to they are common for both channels.

The third item $(\omega_{d2} - \omega_{d1})t_n$ is the accumulated Doppler difference between HC and RC received signal. As the orbit height is much larger than the target area and Doppler are contributed only by the motion of satellite, this term will be zero.

The fourth item $(\tau_2(u,x,y) - \tau(u))\pi$ is navigation message phase differences between two channels, i.e. RC and HC. As the navigation message is the same for RC and HC at transmission side, therefore, This value depends on the difference between the ranges of RC and HC. As the navigation message interval is 20 milliseconds, the minimum range difference to make a phase shift will be $D_{min} = light\ speed \times 20ms = 6000km$. In our configuration, however, since it unlikely for the range difference be larger than 6000km. Therefore, $(\tau_2(u,x,y) - \tau(u))\pi$ will be zero.

Following explanation mentioned above, the range compressed signal is simplified as:

$$s_{rc}(t,u) = CF_P[t - (\tau_2(u,x,y) - \tau(u))] \times e^{[j\phi_{P2}(u,x,y)]} \qquad (4.10)$$

Inspection of Eq. (4.10) indicates that the phase error has already been eliminated in the range compressed signal, only remaining propagation phase. Moreover, it can be found that in range domain, the targets are located at $(x, y, 0)$, while in azimuth domain, proper matched filter will be applied to achieved compression with $e^{[j\phi_{P2}(u,x,y)]}$.

B. Back-projection

Following range compression, bistatic BP algorithm described in Section 4.2 will perform the azimuth compression. First an interpolation operation will be applied on the fast-time signal for all the targets

The interpolation index of targets found on the fast-time signal are given by

$$Ind_{interp}(u,x,y) = \left[\frac{R_R(x,y)+R_t(u,x,y)-R_b(u,x,y)}{c}\right] \times f_{ADC} \quad (4.11)$$

where f_{ADC} is the sampling frequency of ADC.

Combining Eq. (4.10) and (4.11), the range compressed signal from target $(x, y, 0)$ in azimuth bin (u) after interpolation could be written as

$$s_{rci}(u) = CF_P[\ Ind_{interp}(u,x,y)] \times e^{[j\phi_{P2}(u,x,y)]} \quad (4.12)$$

Next, the azimuth matched filter is designed. Given that the exponential term of range compressed signal, i.e. Eq. (4.12) only consists of propagation induced phase, the azimuth matched filter will be the conjugate of this term, but calculated using transmitter and receiver coordinates.

$$s_{azi}(u,x,y) = e^{(j2\pi f_c \frac{R_R(x,y)+R_t(u,x,y)-R_{center}}{c})} \quad (4.13)$$

where f_c is satellite signal carrier frequency and R_{center} is the slant range between synthetic aperture center and scene center.

The azimuth compression between Eq.(4.12) and (4.13) gives the response at single target point $(x, y, 0)$.

$$f(x,y,0) = \int_{-T/2}^{T/2} s_{rci}(u) s_{azi}{}^*(u,x,y)du$$

$$= \int_{-T/2}^{T/2} CF_P[\ Ind_{interp}(u,x,y)] e^{(j2\pi f_c \frac{R_{center}}{c})} du \quad (4.14)$$

Moreover, it can be observed that the propagation phase at scene center is well preserved.

4.4 Simulation results and analysis

In this section, we verified the operational functionality of proposed image algorithm in fixed receiver SS-BSAR system from simulation point of view. The transmitting

signal with bandwidth of 5.11MHz and platform elevation of 19130 km is assumed in this simulation to imitate the real GLONASS scenario. The integration time is assumed to be 300 seconds and receiver is at origin. The simulation takes into account of common receiver and atmosphere artefacts in RC and HC, which will be present in reality. Also path loss and geographic terrain variation are neglected.

Two kinds of bistatic geometries are being considered, as described in Fig. 2.9, i.e. quasi-monostatic geometry and general geometry.

The performance of image formation algorithm is evaluated by comparing simulated image with theoretical counterpart modelled by Eq. (2.27)

4.4.1 Quasi-monostatic geometry

The 2D quasi-monostatic geometry is shown in Fig. 4.5.

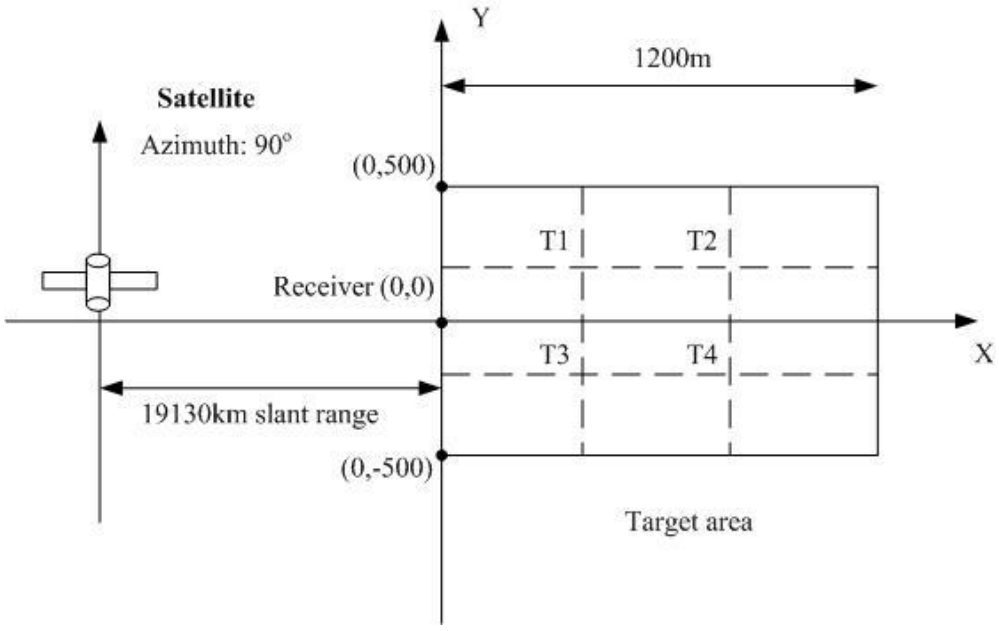

Figure 4.5: 2-D illustration of SS-BSAR in quasi-monostatic geometry

As seen in Fig. 4.5, Satellite is flying along a straight line parallel to Y axis. Receiver is located at (0, 0), pointing towards X direction. The simulation parameters are listed in Table 4.1.

Parameter	Value
Satellite	GLONASS COSMOS 737
Satellite velocity	4000 m/s
Carrier frequency	1601.4375MHz
Nominal signal bandwidth	5.11MHz
Transmitter height	19130 km
Satellite azimuth angle at synthetic aperture center	90º
Satellite elevation angle at synthetic aperture center	45º
Integration time	300 seconds

Table 4.1: Quasi-monostatic geometry simulation parameters

The satellite azimuth angle and elevation angle in Table 4.1 have the same contents with marked in Fig. 2.9.

The target area is in X-Y plane, from 0 to 1200m along X axis and -500 m to 500 m along Y axis. We assume there are 4 point targets in the area, being distributed evenly as shown in Table 4.2.

Target point	X-axis position (m)	Y-axis position (m)
T1	400	200
T2	800	200
T5	400	-200
T6	800	-200

Table 4.2: Target points locations in simulation

We assume synchronization has already been completed and go directly to image formation using BP algorithm. The echo signals after range compression as well cross-section along fast-time direction are shown in Fig. 4.6.

It can be observed from Fig. 4.6(a) that after range compression, the echo energy along fast-time direction is concentrated to the two Range Cell Migration (RCM). It is expected, due to that the simulation scenario employed small target scene and quasi-monostatic geometry, the RCMs from different targets with same X-axis positions can be seen the same. The centers of RCMs are located at 67 and 135 sample point along fast-time domain, which corresponds to 400m and 800m along X (range corresponding to one sample is light speed (3×10^8 m/s) times sample duration (2×10^{-8}s), which is 6 meters, therefore 67 sample and 135 sample correspond to 400 and 800 m.). Moreover, Fig. 4.6(b) and (c) show that the half width of range compression signal along fast-time direction is 10 samples, which coincides with theoretical expectation of single pulse after compression (the number of sample in one chip is 1/5.11MHz/1/50MHz). Section 4.42 will demonstrate the RCM acquired from general geometry, its difference to here will be notified.

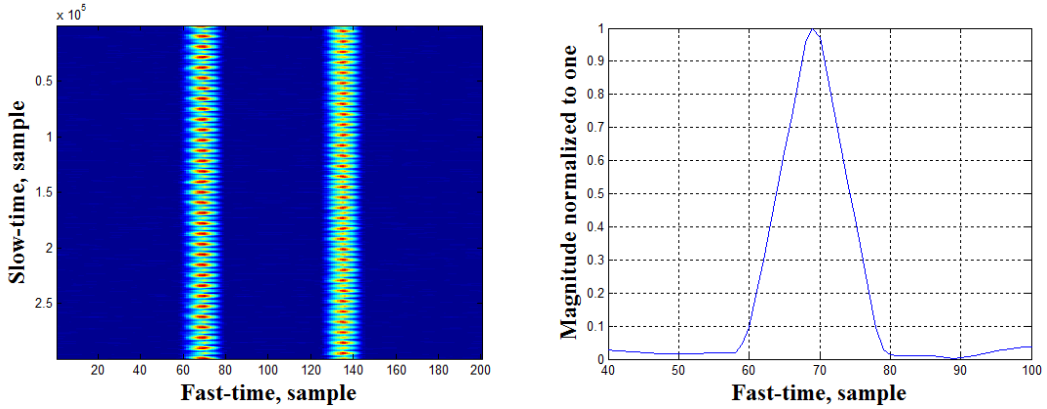

(a) (b)

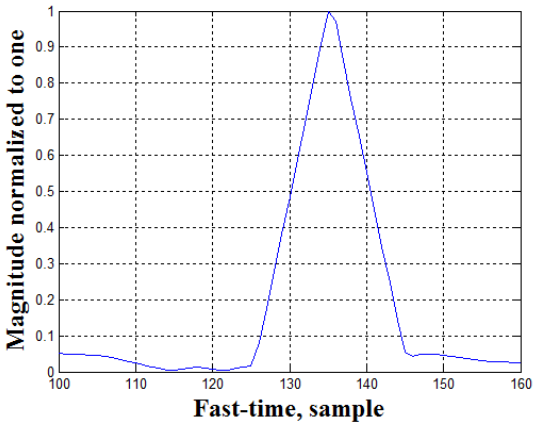

(c)

Figure 4.6: (a) Range compressed signal, (b) Cross-section of left RCM along fast-time,

(c) Cross-section of right RCM along fast-time

The obtained SS-BSAR image simulated in quasi-monostatic geometry is shown in Fig. 4.7.

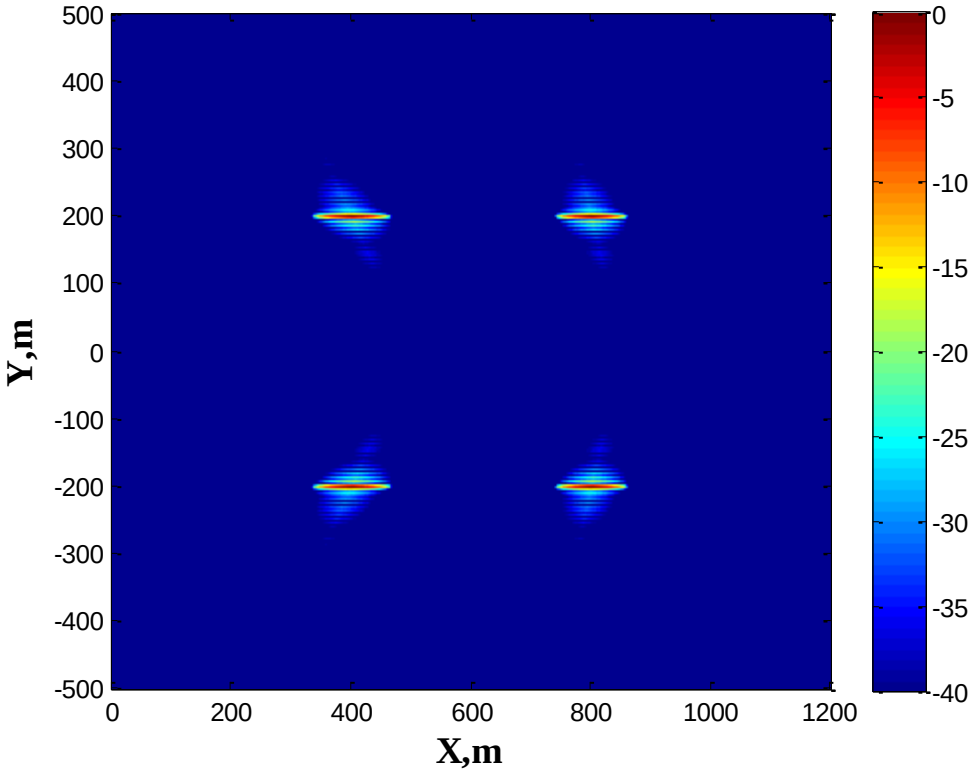

Figure 4.7: Simulated SS-BSAR image

It can be observed that image of each targets are well focused at corresponding positions. In addition, the similar flashes for all the targets indicate similar 2-D resolutions of them.

The enlargements of targets T1 and T4 are shown in Fig. 4.8. It could be found that their main-lobes have high level of similarity. The differences lie at the side-lobes, whose orientations present the iso-range curve. Their corresponding cross sections in X and Y direction are shown in Fig. 4.9 and 4.10.

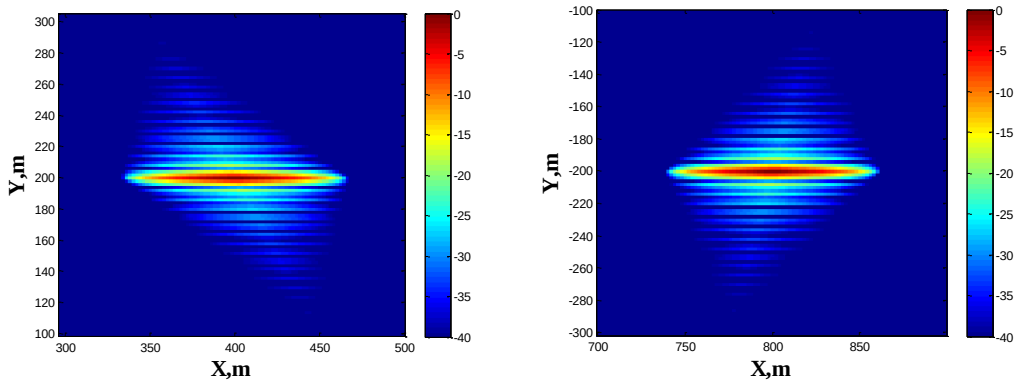

(a) (b)

Figure 4.8: Enlargement of (a) Target T1, (b) Target T4

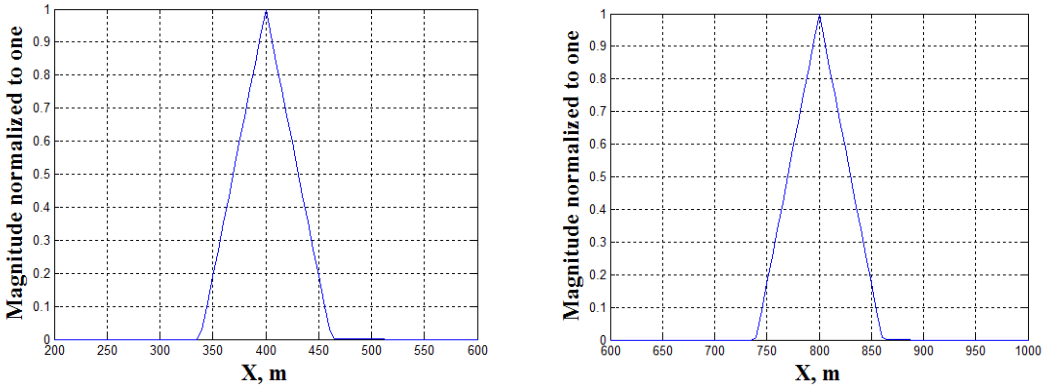

(a) (b)

Figure 4.9: Cross Sections along X direction for (a) Target T1, (b) Target T4

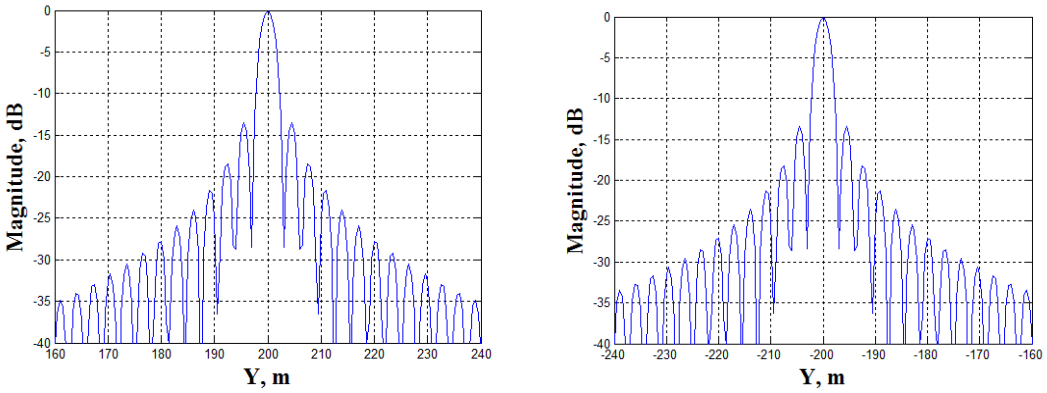

(a) (b)

Figure 4.10: Cross Sections along Y direction for (a) Target T1, (b) Target T4

Inspections from Fig. 4.8 to Fig. 4.10 show that the responses of Target 1 and Target 4 are very similar and they are located where they should be. The cross Sections along two directions are both highly agreed with theoretical expectation. Due to that along X axis, the correlation output of satellite transmitting signal is a rectangular, while along Y axis is a sinc where chirp is applied.

The resolution of obtained image is examined by measuring -3dB width of cross section along the direction you are interested. Response of target T1 is inspected at cross Sections along X and Y direction. Comparison between simulated results and theoretical results measured by Eq. (2.27) are shown in Fig. 4.11

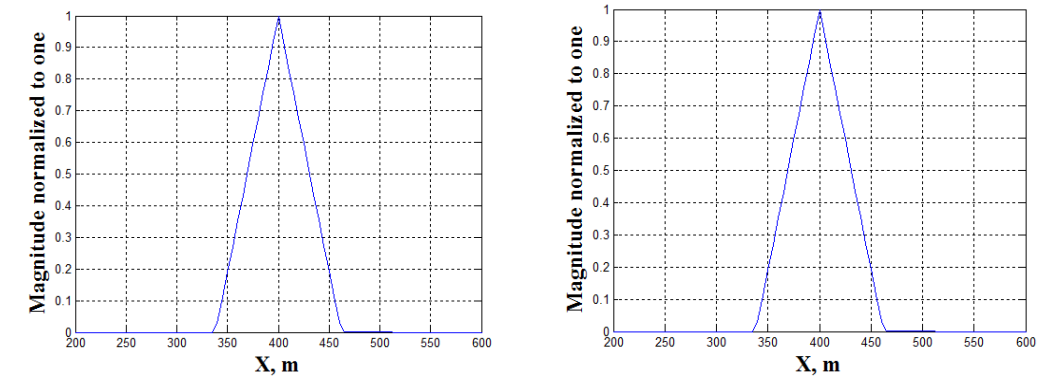

(a) (b)

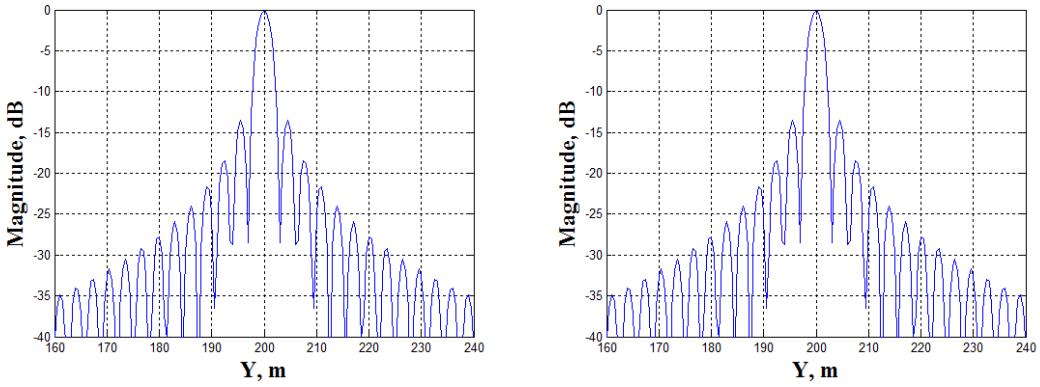

(c) (d)

Figure 4.11: Cross Sections of Target 1: (a) Simulated result along X direction, (b) Theoretical result along X direction, (c) Simulated result along Y direction, (c) Theoretical result along Y direction

The -3dB widths measured in Fig. 4.11 are listed in Table 4.3.

	-3dB width along X (m)	-3dB width along Y (m)
Theoretical result	35.2	2.7
simulation result	35.2	2.7

Table 4.3: Theoretical and simulated resolution along X and Y directions

Inspection of Fig. 4.11 and Table 4.3 shows high level of similarity between simulation and theoretical counterpart, therefore verifying correct functionality of our BP simulation.

4.4.2 General geometry

Then we come to the imaging simulation implementation using real orbit data. The 2-D bistatic configuration is shown in Fig. 4.12.

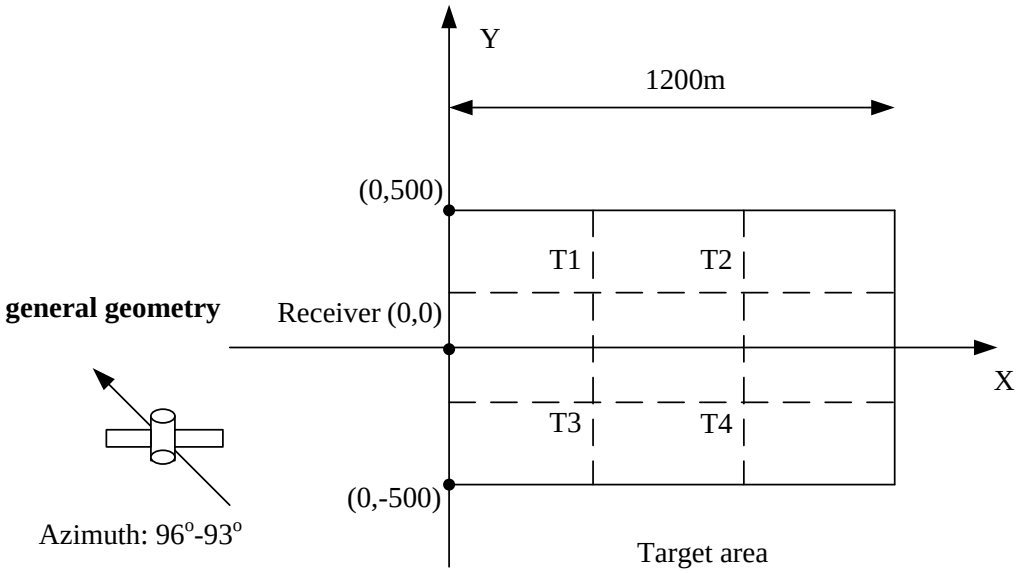

Figure: 4.12: 2-D illustration of SS-BSAR in general geometry

Real orbit data is from GLONASS 736, the simulation parameters are listed in Table 4.4.

Parameter	Value
Satellite	GLONASS 736
Carrier frequency	1600.3125MHz
Satellite signal used	P-code (L1)
Signal bandwidth	5.11MHz
Satellite elevation angle	$65^o - 49^o$
Satellite azimuth angle	$96^o - 93^0$

Table 4.4: General geometry simulation parameters

The locations of 4 targets (i.e. T1, T2, T3, T4) are the same with before and listed in Table 4.2.

The signal after range compression as well as cross section along fast-time domain is shown in Fig. 4.13.

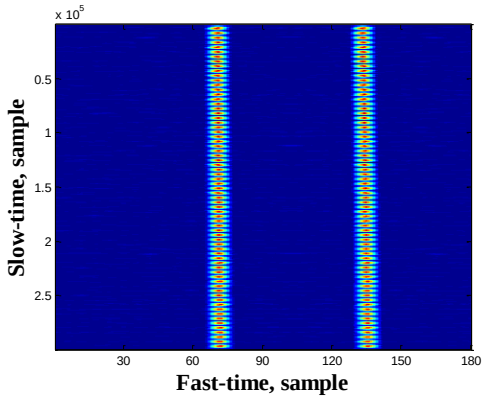

(a)

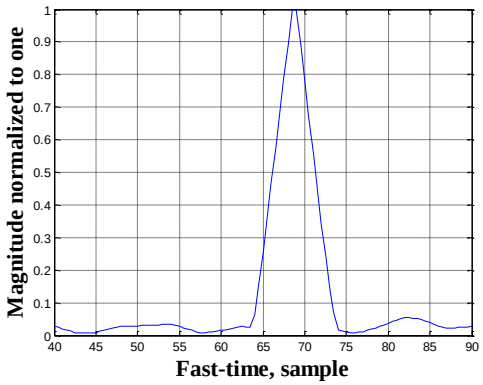

(b)

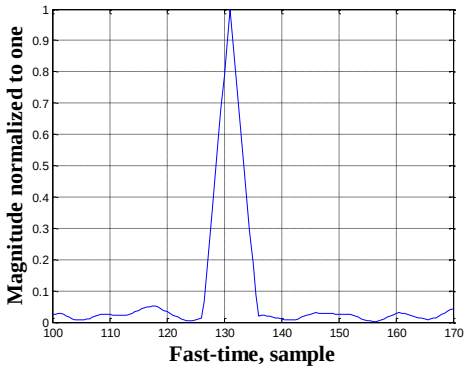

(c)

Figure 4.13: (a) Range compressed signal, (b) Cross-section of left RCM along fast-time, (c) Cross-section of right RCM along fast-time

Inspection of Fig. 4.13(a) shows that the RCMs have similar width with those of quasi-monostatic geometry. This is accredited to the general geometry here employed has the similar bistatic geometry with quasi-monostatic geometry.

The obtained SS-BSAR image simulated in general geometry is shown in Fig. 4.14.

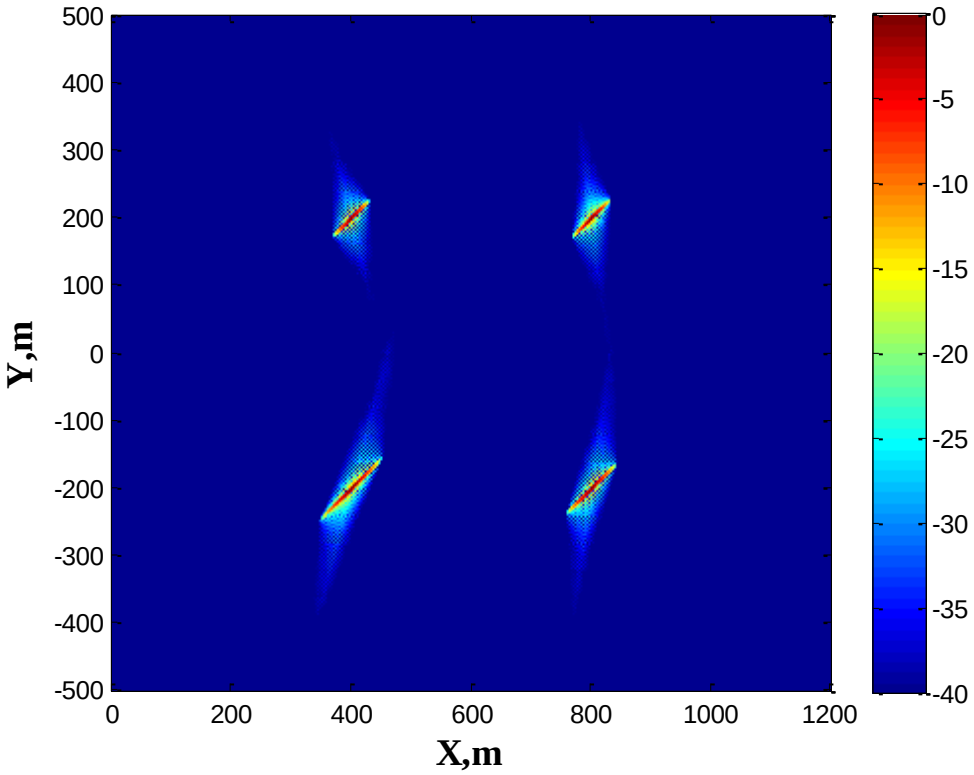

Figure 4.14: Simulated SS-BSAR image

It could be observed from Fig. 4.14 that four target points are separated apart and located at its corresponding positions. Moreover, the size of the flash is different for each target. This is expected due to that in general geometry, targets at different positions will result in different bistatic angle, thereafter yielding different size.

The enlargements of targets T1 and T4 are shown in Fig. 4.15. Their corresponding cross sections in X and Y direction are shown in Fig. 4.16 and 4.17.

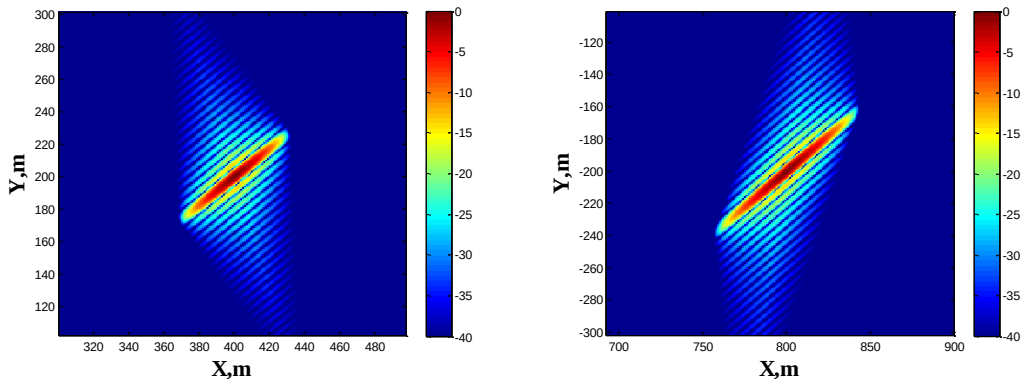

(a) (b)

Figure 4.15: Enlargement of (a) Target T1, (b) Target T4

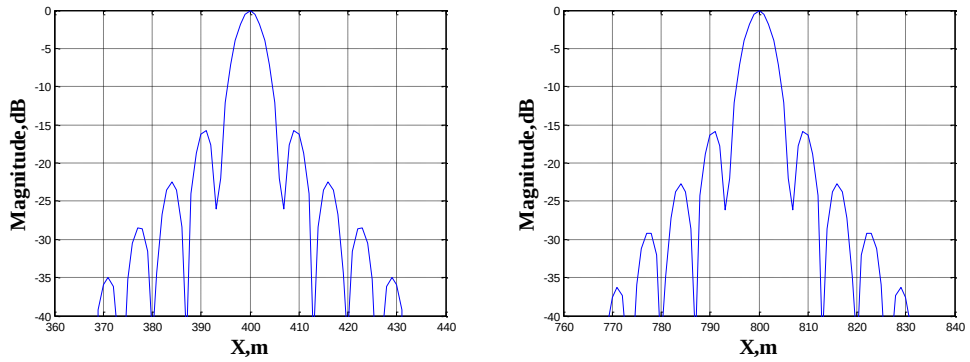

(a) (b)

Figure 4.16: Cross sections along X direction for (a) Target T1, (b) Target T4

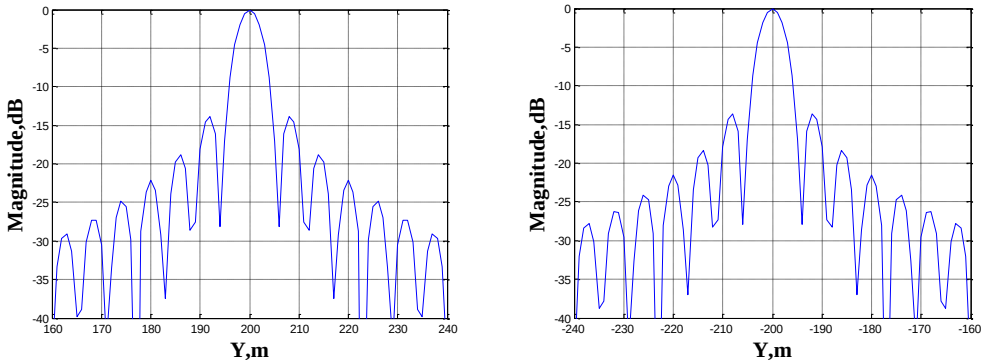

(a) (b)

Figure 4.17: Cross sections along Y direction for (a) Target T1, (b) Target T4

Inspection of Fig. 4.16 and 4.17 shows that the cross Sections of both targets along X are no longer triangles and along Y no longer sinc function (the Peak Sidelobe Ratio

(PSLR) is 13.6 for sinc function), as expected due to 2-D responses of the target is coupling here, which was not serious in quasi-monostatic case. Moreover, the discrepancy in targets response cross-sections between T1 and T4 verifies the space variant characteristics of general configuration Bistatic SAR.

Same with quasi-monostatic case, the resolution of obtained image is examined by measuring -3dB width of cross section along the direction you are interested. Response of target T1 is inspected at cross sections along X and Y directions. Comparison between simulated results and theoretical results are shown in Fig. 4.18.

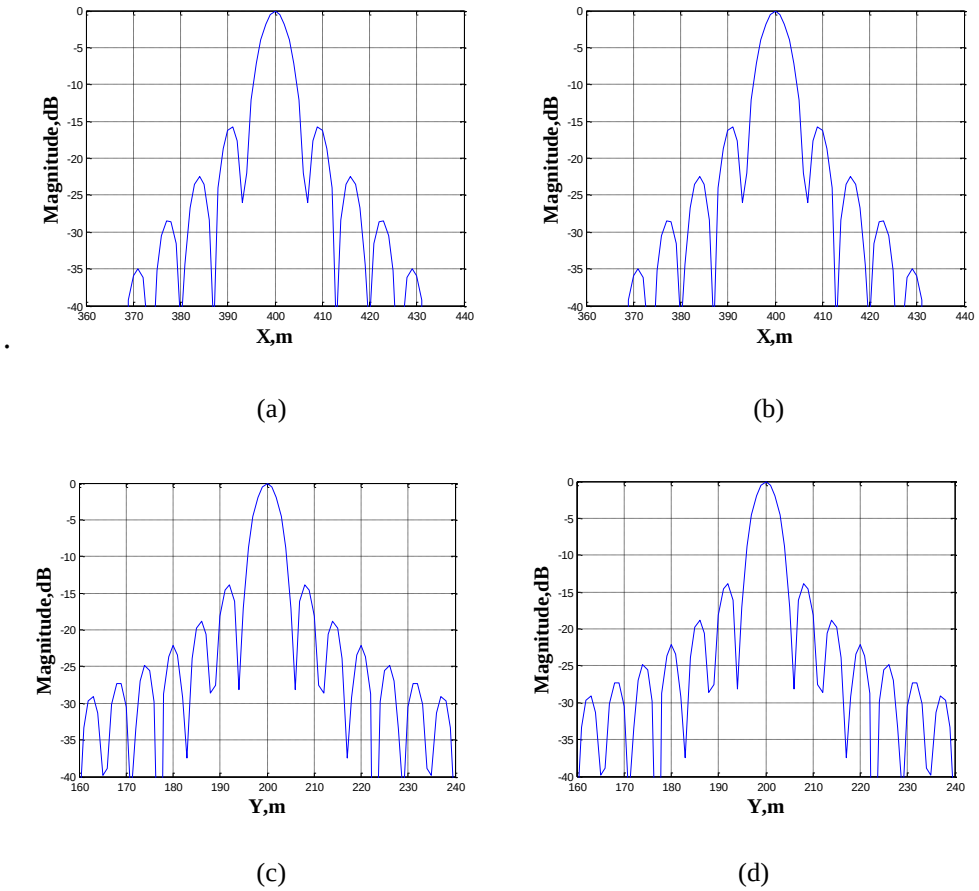

Figure 4.18: Cross sections of Target 1: (a) Simulated result along X direction, (b) Theoretical result along X direction, (c) Simulated result along Y direction, (c) Theoretical result along Y direction

The -3dB widths measured in Fig. 4.19 are listed in Table 4.5.

	-3dB width along X direction (m)	-3dB width along y direction (m)
Theoretical result	5.2	4.8
simulation result	5.2	4.8

Table 4.5: Theoretical and simulated resolution along X and Y directions

Inspection of Fig. 4.18 and Table 4.5 shows good accordance between simulation and theoretical counterpart, suggesting correct functioning of our image processor.

The simulation results above demonstrate that the modified back-projection algorithm can be well performed in SS-BSAR with GLONASS and stationary receiver on theoretical level, even in the presence of unpredicted receiver noise and atmosphere artefacts. Based on this, the next step is to conduct proper experiments and apply the algorithm in practice.

4.5 Conclusion

Due to complex image nature inherent in stationary receiver bistatic SAR system, the modified back-projection algorithm has been selected for imaging formation. The chapter presents the system geometry and mathematical derivation of such an algorithm. Theoretically speaking, though there may be some phase errors caused by receiver artefacts, it could be almost removed after range compression. Two simulation experiments were studied to verify the modified BP algorithm. One is called quasi-monostatic case, where the transmitter is flying along a straight line. In the other one, we use real satellite and receiver positions to imitate general geometry. To evaluate our simulation tool, comparison has been made between one target point

from simulated image and theoretical PSF of corresponding location. The high accordance suggests correct functioning of our bistatic BP simulator.

CHAPTER 5

EXPERIMENTAL IMAGERY AND ANALYSIS

5.1 Introduction

This chapter presents the results obtained with regard to our imaging experiments, as well as the analysis of the findings. A number of experiments were conducted during my PhD periods, aimed at from system prototype verification to further applications such as change detections, etc. This chapter only selects the most representative four experiments, through which the capability of imaging using our system can be demonstrated. The summary of selected experiments discussed in this chapter is listed in Table 5.1.

Experiment	Date	Satellite
Prototype experiment	19th December 2010	GLONASS COSMOS 732
Feasibility experiment	18th March 2011	GLONASS COSMOS 737
Vale village site experiment	29th February 2012	GLONASS COSMOS 744
Metchley park site experiment	24th July 2012	GLONASS COSMOS 736

Table 5.1: Summary of imaging experiments presented in this thesis

The first experiment is called prototype experiment, aimed at verifying our system functionality. During the dwelling time, two identical antennas were 50 m apart and receiving signal directly from one single satellite. The antenna at far end imitated a single transponder and connected to our receiver with a cable. In this way, the system is exempt from clutter and random scattering from environment. Obtained signal target PSF demonstrated system functionality. Such a prototype has also been used as a test-bed for CCD, which will be discussed in next chapter. Following up the prototype experiment, the image feasibility experiment was carried up. This time, a real experimental platform has been setup, i.e. one antenna was pointing directly to the satellite, while the other one was pointing to the target area. A big building closer to receiver can be served as a reference target. This obtained experimental image proved the imaging capability of our system in real scenario. The Vale village site experiment and Metchley park site experiment were implemented towards different target area, which are quite different in terms of ground features. The vale village site, features with small buildings, trees and grasslands. A high building in the center of image scene can be served as a isolated reference point for system calibration. On Metchley park site, there are four high buildings at far distance (around 1250m), Visibility of such buildings can be used for power budget analysis. Apart from single acquisition of four scenarios mentioned above, a number of images of different satellites and different geometries at Metchley park were acquired. The applications such as change detection and ground feature extraction could be a possible after investigating these images in different aspects. This chapter only deals with experiments and imaging analysis, while future work of last chapter will discuss some mentioned applications.

This chapter presents the four obtained images and associated signal processing results at every stage leading to obtained images during my PhD. Section 6.2 to Section 6.5 present prototype experiment, feasibility experiment, Vale village site experiment and Metchley park site experiment in sequence. Section 6.6 finalizes all the work in this chapter.

5.2 Prototype functionality experiment

Experimental overview

The prototype functionality experiment was performed on December 20th 2010 near the School of Electrical Electronic and Computer Engineering in UOB. The trial site is on a piece of large empty lawn (Fig. 5.1). Both the HC and RC antennas were pointing towards the satellite, while the RC antenna was connected to the receiver via a 50m long cable. In this way, this configuration enabled the RC antenna to imitate an ideal point target, located 50m away from the receiver. The experiment is well ideal for system calibration. The reasons are multiple. The interference from clutters and unpredictable environments will be negligible. Moreover, random target scattering in conventional radar can be prevented in case of direct signal absorption, resulting in a higher image SNR.

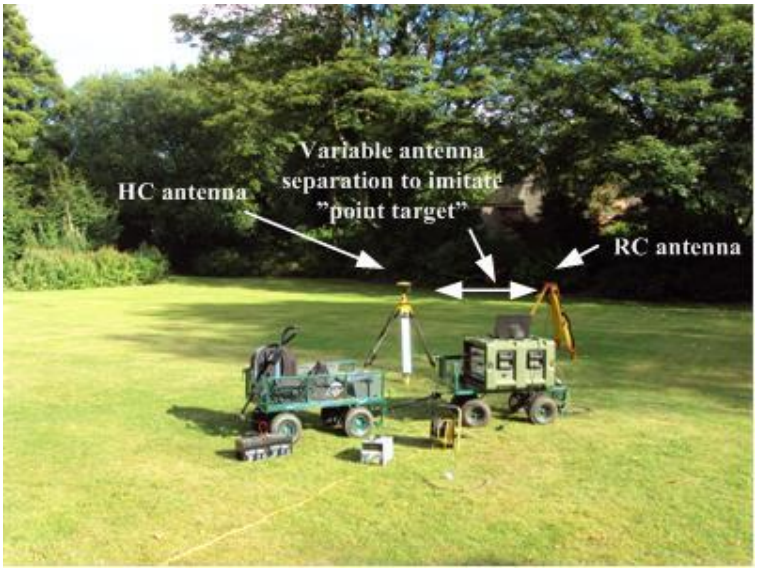

Figure 5.1: Experimental equipments used in the prototype trial

GLONASS COSMOS 732 was employed as the transmitter of opportunity. The ranging signal P-code was used for image formation. During the experiment, the satellite moves at the periods of 300s, resulting in the variation of its positions in each epoch. The experiment acquisition parameters are listed in Table 5.2.

Parameter	Value
Transmitting satellite	GLONASS COSMOS 732
Carrier frequency	1603.6875MHz (L1)
Satellite signal used	P-code
Signal bandwidth	5.11MHz
Satellite elevation angle	$48^o - 52^o$
Satellite azimuth angle	$298^o - 301^o$
Integration time	300s
Bistatic angle	162^o
PRF used for signal processing	1KHz

Table 5.2: Experimental parameters

It is noteworthy that satellite elevation angle is measured relative to horizon of observation location, and azimuth angle is measured relative to the North direction.

Both parameters vary during long integration time. The definition will apply through this thesis, without particularly notifying.

The satellite and receiver ECEF coordinates during experiments were obtained on IGS webpage accordingly. The local coordinate frame defines that HC antenna is located at origin (i.e. point(0,0)). Two axes are pointing to North direction and West direction respectively. By using Helmert algorithm, the global satellite and receiver positions were transformed to the local counterparts, which were measured with regard to location of observation. Fig. 5.2 presents the satellite photograph of the experiment scene (HC antenna location, RC antenna location and environment) overlaid with local grid coordinate (Northings, Westings) and satellite positions, i.e. azimuth (φ), elevation (γ) relative to the HC location.

Figure 5.2: Imaging scene superimposed on local coordinate frame

As you can see from Fig. 5.2 that the RC antenna is placed on the first quadrant, while the project of satellite trajectory falls on the second quadrant.

From the Eq. (2.20), the image SNR is approximately,

$$SNR_{img} = 26 + 10 \times log10(5.11 \times 300) = 57.85dB \quad (5.1)$$

The value here shows the noise floor is at level of -57.85 dB relative to RC PSF peak value.

To examine the range and Doppler variation, calculation by using local satellite and HC antenna positions was performed to estimate the range history and Doppler history during experiment time (Fig. 5.3).

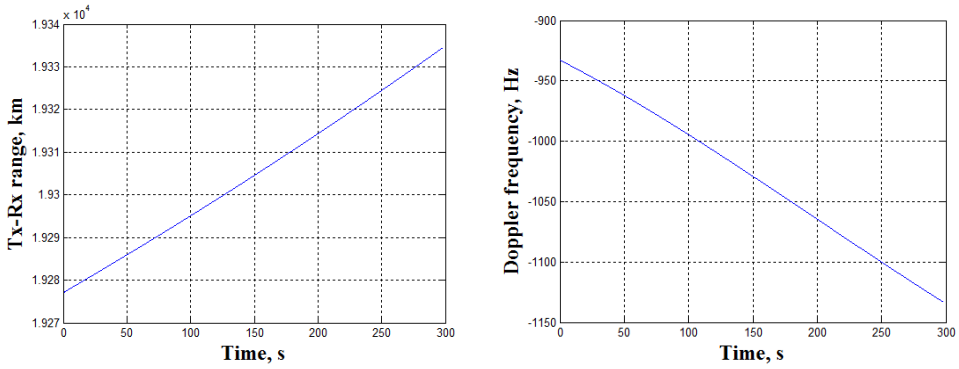

(a) (b)

Figure 5.3: (a) Estimated range history, (b) Estimated Doppler history

It can be seen that the satellite to receiver range history is between 19270km to 19340km during dwelling time, which has a high level match with nominal satellite elevation specified in [71]. The Doppler varies between around -930Hz to 1130Hz, resulting in a bandwidth of 200Hz in azimuth direction.

Signal synchronization

Following experiment, the collected data would be synchronized to get delay, Doppler and phase information. The proposed synchronization algorithm described in chapter 3 was applied, giving the tracking results shown in Fig. 5.4.

The synchronization results shown in Fig. 5.4 demonstrate the same contents with those in chapter 3. It could be seen that the delay and Doppler curve are both straight line. Slow-time signal becomes periodic and its spectrum becomes flat top rectangular shape after removing navigation message, which indicates chirp like signal in its time domain.

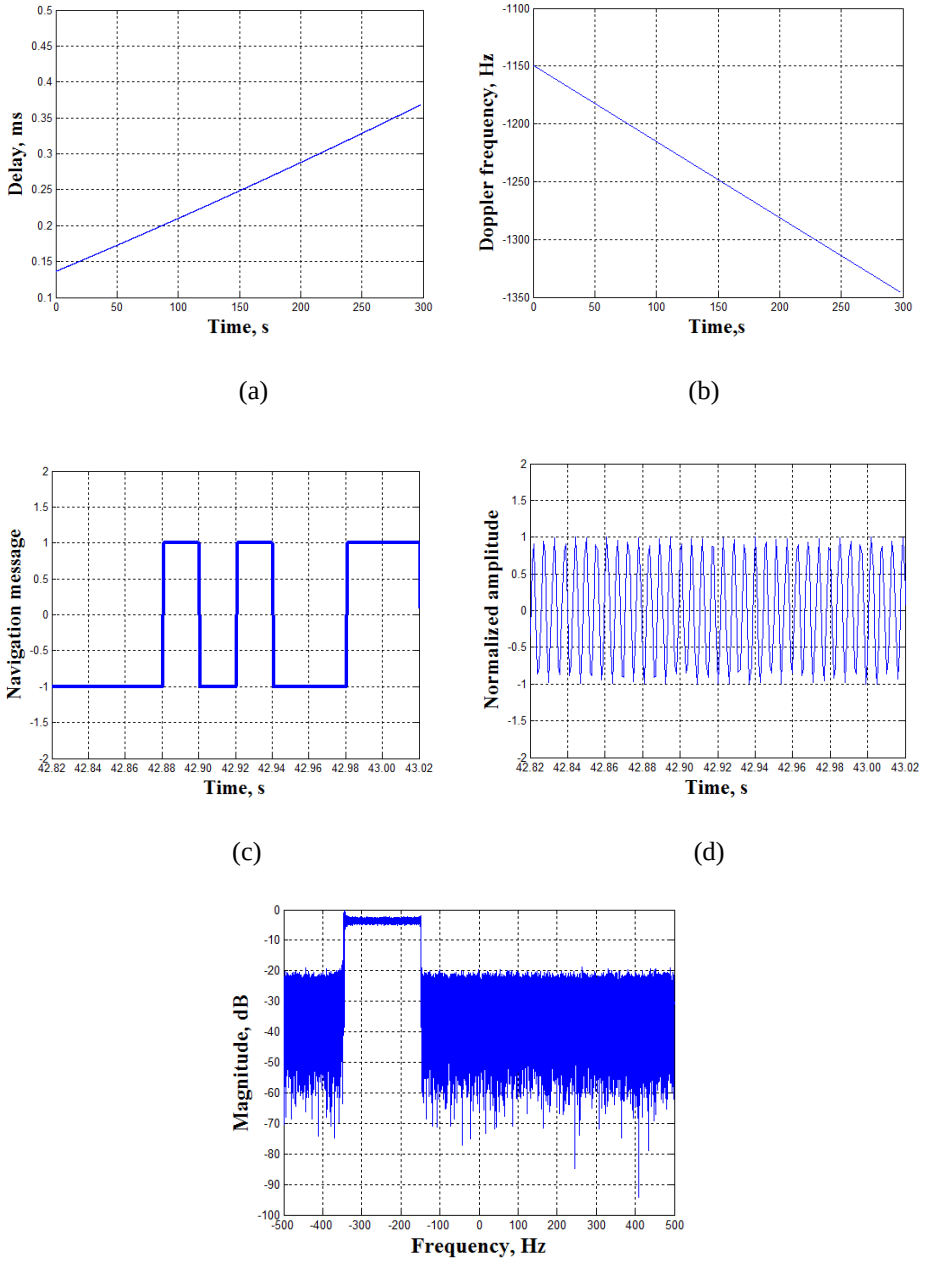

Figure 5.4: (a) P-code Delay, (b) P-code Doppler, (c) P-code decoded navigation message, (d) P-code slow-time signal (without navigation message), (e) P-code slow-time signal spectrum (without navigation message),

Using the synchronized parameters (delay, Doppler, phase), the range reference signal is generated for every azimuth point by Eq. (4.9).

The accuracy of synchronized outputs are examined by checking range compressed signal between raw HC data and locally generated signal. Fig. 5.5 provides the results.

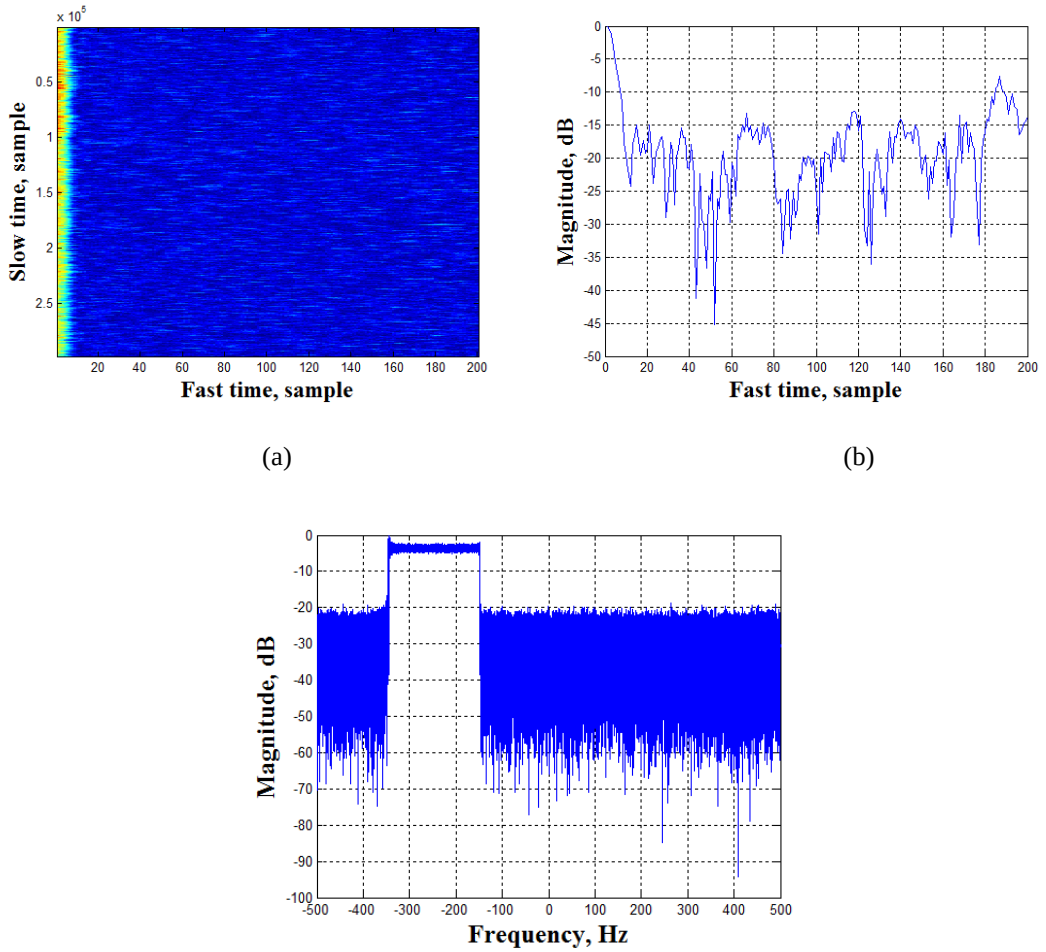

Figure 5.5: (a) Range compressed signal, (b) Cross section along fast time, (c) Signal spectrum along slow-time after navigation message removal

Fig. 5.5(a) shows the HC range compressed signal in fast time slow time domain. Fig. 5.5(b) is the cross-Section along fast time. Observation of this plot indicates that the peak is located at the first range, corresponding to our expectation. Fig. 5.5(c) is the

signal spectrum along slow-time. From Fig. 5.5(c), it could be seen that the phase term has been preserved after navigation bits decoding. To sum up, the synchronization on HC signal is well performed.

Experimental image and analysis

The experimental SS-BSAR image is formed by modified BPA on RC signal. The resulted image is shown in Fig. 5.6(a). The image is plotted in dB scale, where 0 dB corresponds to the highest signal intensity. The dynamic range has been clipped to 35 dB. The location of the HC antenna marks the origin of the local coordinate system [i.e., the point (0,0)]. It could be seen that the center of target response is located at (44, -20, 0), which is where the RC antenna located. Also, both sidelobes in two wings are symmetric, indicating that energy has been evenly distributed. The theoretical simulated PSF using Eq. (2.27) is presented in Fig. 5.6(b). Comparing these two images, it shows that they are in good accordance, where they share the same orientation and same size in all area. The resolution in range and azimuth is not orthogonal, as expected due to bistatic acquisition parameters. The cross-sections at both North direction and West direction are shown in Fig. 5.6(c) and Fig. 5.6(d). The theoretically calculated counterparts are superimposed on them.

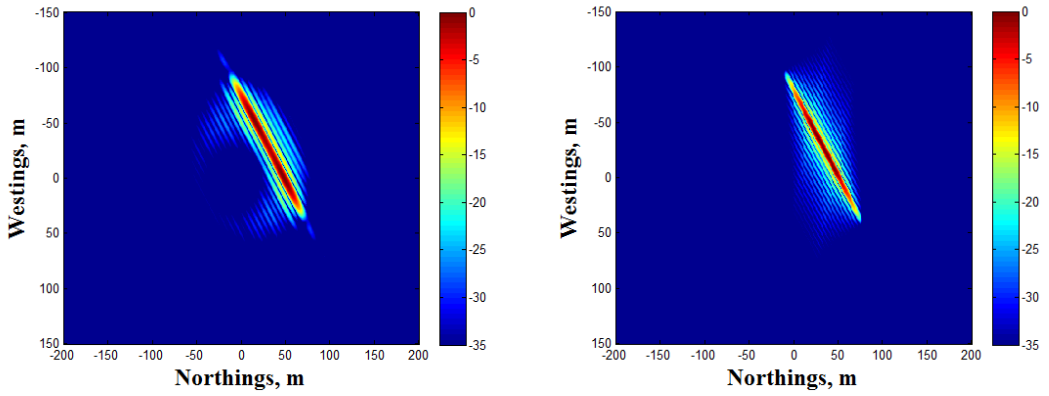

(a) (b)

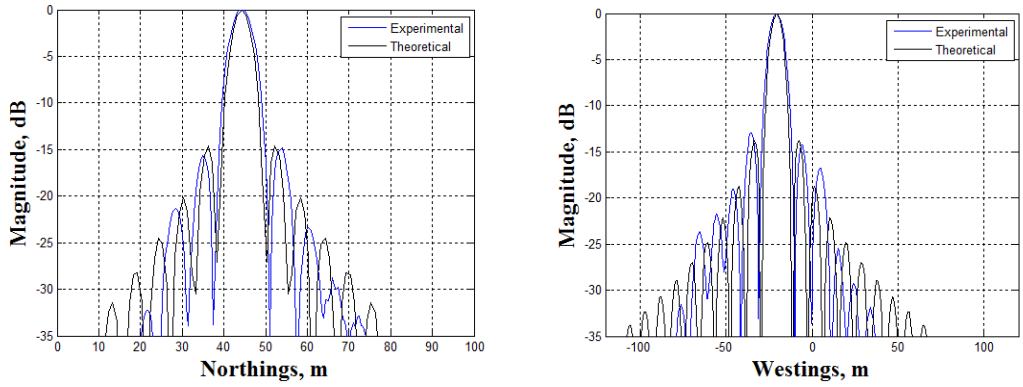

(c) (d)

Figure 5.6: (a) Experimental RC image, (b) Theoretical calculated PSF, (c) Cross-section in North direction, (d) Cross-section in West direction

Inspection of the cross-sections shows that the main-lobes along both North and West directions have high level of similarity, though there are some differences between theoretical and experimental side-lobes. It may be explained by oscillator instability.

The resolutions along North and West directions are found by measuring -3dB widths in Fig. 5.6(c) and (d). Table 5.3 lists the experimental and theoretical results.

	Resolution at South direction (m)	Resolution at East direction (m)
Theoretical result	4.7	7.7
Experimental result	4.8	7.9

Table 5.3: Theoretical and experimental resolutions at South and East directions

It could be observed that the experimental resolutions are only 0.1m and 0.2m more than theoretical one at South direction and East direction respectively, which is trivial compared to gross value. It is apparent from this measurement and the overall shape of the response that the image is fairly well focused at this point.

5.3 System feasibility experiments

Experiment overview

The system feasibility experiment was performed in March 23rd 2011 in the campus of UOB. The aim is to prove the imaging feasibility of SS-BSAR with GLONASS and stationary receiver. The receiver is placed on the roof of School of Electronic, Electrical and Computer Engineering. Fig. 5.7 shows the equipments used for the experiments. Two antennas i.e. RC antenna and HC antenna are used to receiving signals from target area and satellite respectively. The signals received from two antennas are passed through to the receiver box (Fig. 2.6) for processing. The transmitter is GLONASS 732.

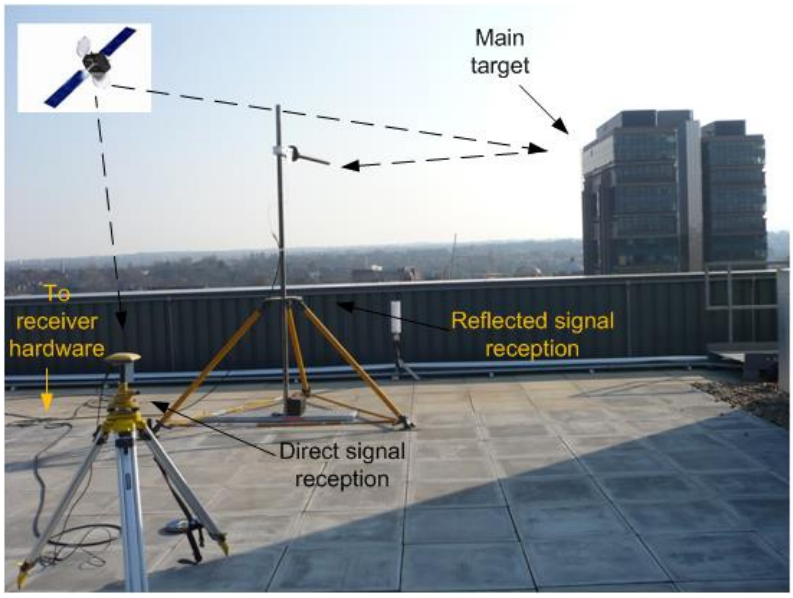

Figure 5.7: Equipments used for experiment

The imaging target area is South to the receiver, as shown in Fig. 5.8. The receiver pointed to the South direction, where the RC antenna main-lobe bisector is marked with white solid lines. Generally speaking the target area is full of scattered objects such as buildings, trees, grass, etc, which is not preferable for image purpose. However, it could be used for system feasibility study due to there are several high

buildings that could be served as prominent reference points, e.g. Muirehead tower. The local grid coordinate follows Southings and Eastings. The satellite flying positions are remarked and projection on the ground is marked with yellow dashed line at left bottom (Fig. 5.8). It can be seen that the image target area is in the first and second quadrant of the coordinate, while the satellite flies in the third quadrant. Such a bistatic geometry results in desirable bistatic angle leading to preferable range resolution.

Figure 5.8: Imaging scene superimposed on local coordinate frame

Figure 5.9 presents the main targeting buildings in the target scene, photograph taken from location of observation. There are five distinguishable buildings marked, i.e. Muirhead tower, Library, Arts buildings, Birmingham business school, and Barber institute of fine art. The location and height of each feature is listed in Table 5.4

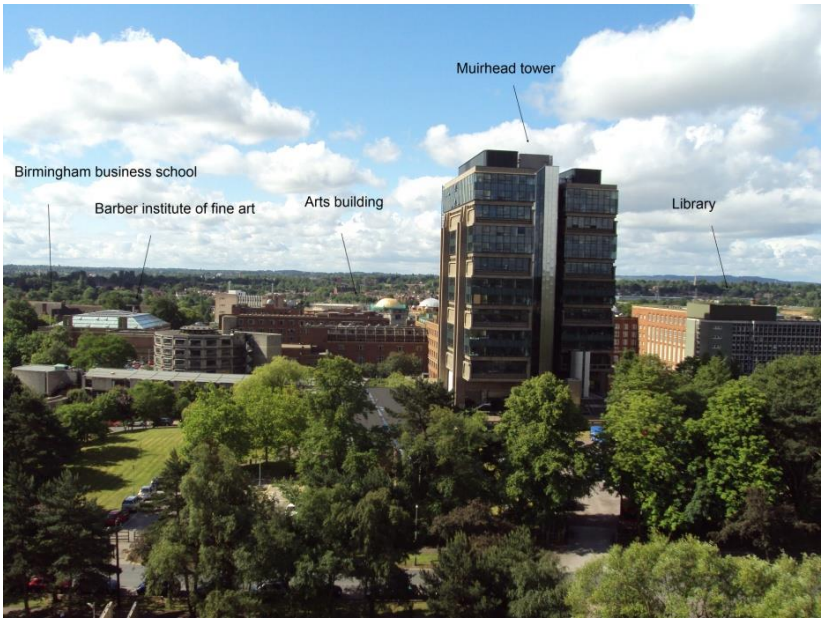

Figure 5.9: Optical photograph of target area taken from location of observation

Building name	Geographic location (m)		
	Range	Cross-range	Height
Muirhead Tower	110	80	60
Library	130	120	20
Birmingham business school	400	-300	10
Barber institute of fine art	330	-60	10
Arts building	230	70	15

Table 5.4: Positions and heights of main target buildings

The dwell time applied is 5 minutes, and the experimental parameters are listed in Table 5.5.

Parameter	Value
Transmitting satellite	GLONASS COSMOS 737
Carrier frequency	1601.4375MHz (L1)
Satellite signal used	P-code
Signal bandwidth	5.11MHz
Satellite elevation angle	$71^o - 68^o$
Satellite azimuth angle	$73^o - 60^o$
Integration time	300s
Bistatic angle	72.8^0
PRF used for signal processing	1KHz

Table 5.5: Experimental parameters

From Eq. (2.21) and (2.22), the SNR at receiver location in RC image and power budget for targets at varying ranges are shown in Fig. 5.10.

$$SNR_{img} = 26 + 10 \times log10(5.11 \times 300) = 57.85dB \tag{5.2}$$

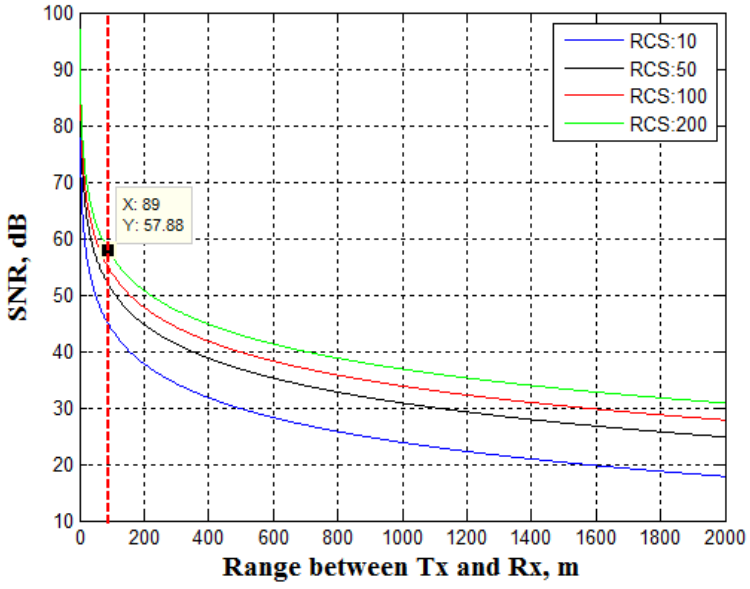

Figure 5.10: RC image target SNR vs. target to receiver range

It can be seen from Fig. 5.10 that the target with RCS of $50m^2$ can be detected at range of 1000m (i.e. target SNR at 1000m is 33dB). Moreover, the response at

receiver is likely to obscure the other targets (in order to get high signal intensity than receiver response, even a target with RCS of $200m^2$ is needed to be located less than 89m from receiver).

Signal synchronization

Once again, after data collection, signal synchronization will be done on the raw HC data. Same contents with Figure 5.4, Fig. 5.11 (a-e) presents tracked P-code delay, P-code Doppler, decoded P-code navigation message, P-code phase and slow-time signal spectrum. Inspection of these plots shows that the delay, Doppler and phase were well tracked. Moreover, after navigation message removal, the slow-time signal spectrum becomes ideal for azimuth compression.

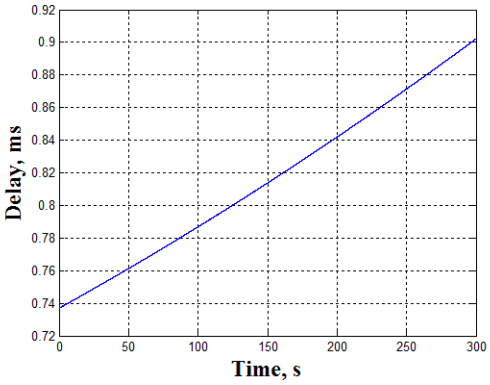

(a)

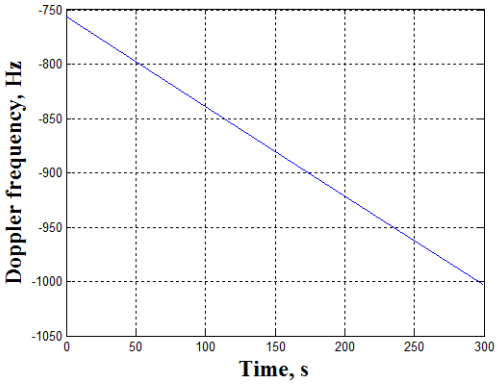

(b)

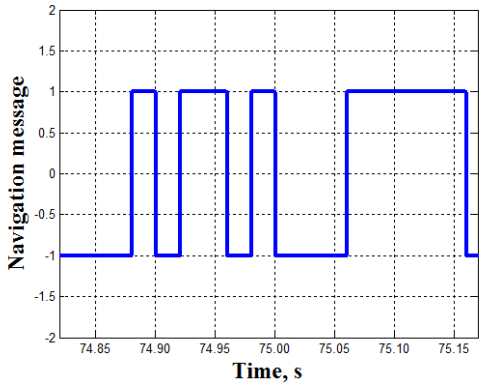

(c)

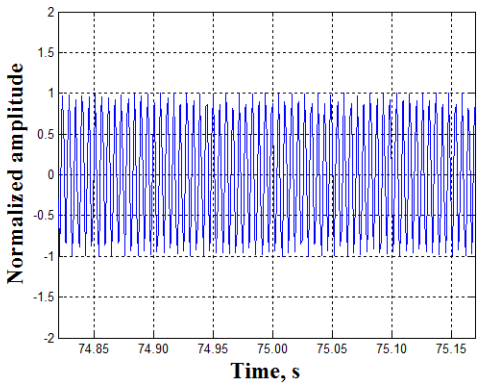

(d)

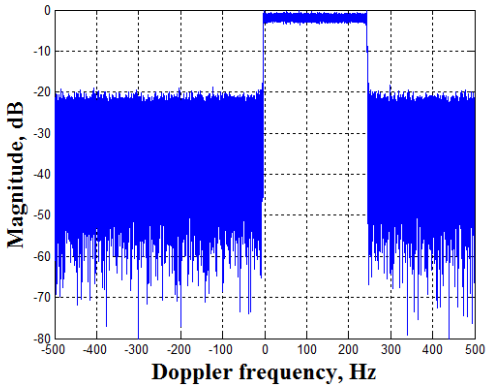

(e)

Figure 5.11: (a) P-code Delay, (b) P-code Doppler, (c) P-code decoded navigation message, (d) P-code slow-time signal (without navigation message), (e) P-code slow-time signal spectrum (without navigation message)

The range compressed image of HC signal followed by cross-sections along two dimensions is shown in Fig. 5.12. It can be found from Fig. 5.12(b) and (c) that SNR at fast time dimension is up to 17dB. The coincidence between Fig. 5.12(c) and Fig. 5.11(h) verifies that navigation and phase noise has been fully removed from HC signal, only remaining propagation induced phase.

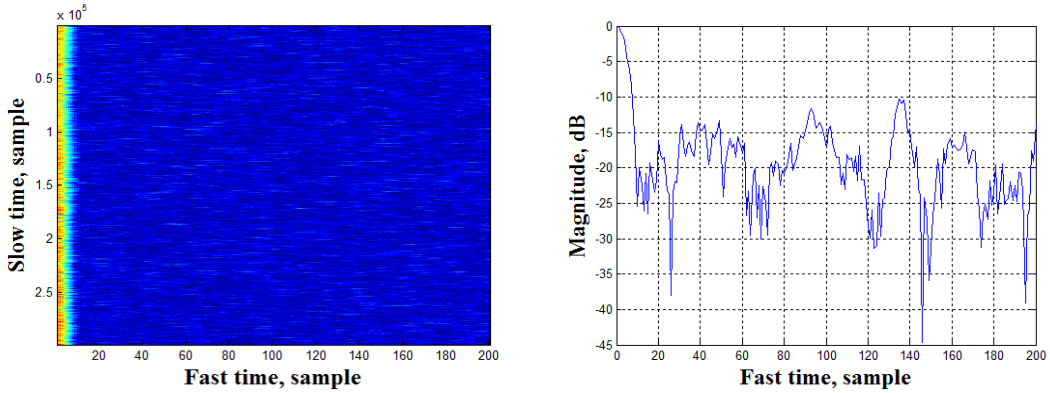

(a) (b)

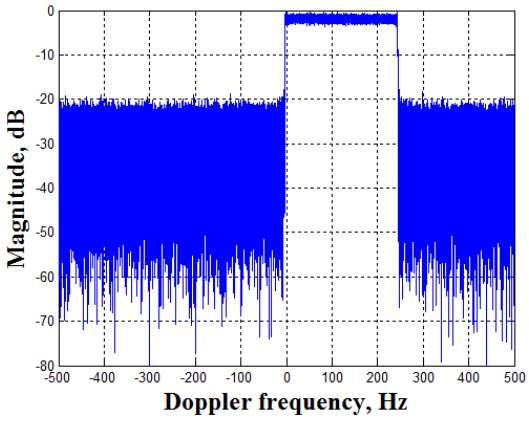

(c)

Figure 5.12: (a) HC range compressed signal, (b) Fast-time direction cross-section, (c) First range bin signal spectrum after navigation message removal

Experimental imagery and analysis

Image formation for HC signal is performed at first place to verify system functionality. The obtained HC image is shown in Fig. 5.13(a). The image is plotted in dB scale, where 0dB represents the highest magnitude. The center of target response is the origin of local coordinate [i.e. at point (0,0)], where the HC receiver is located at. The theoretical PSF generated from the same parameters is shown in Fig. 5.13(b). The cross-sections along South and East directions are shown in Fig. 5.13(c) and (d). Few notes can be drawn after inspection of four images. The flashes of experimental and theoretical results have the same main-lobes and orientations in grid coordinate. Though side-lobes are a little different at left wing between experimental result and theoretical result, which may be caused by I Q imbalance after quadrature demodulation, they are much the same at the other wing. In addition, the cross-sections between the two have high similarity, suggesting good focus achieved in HC signal.

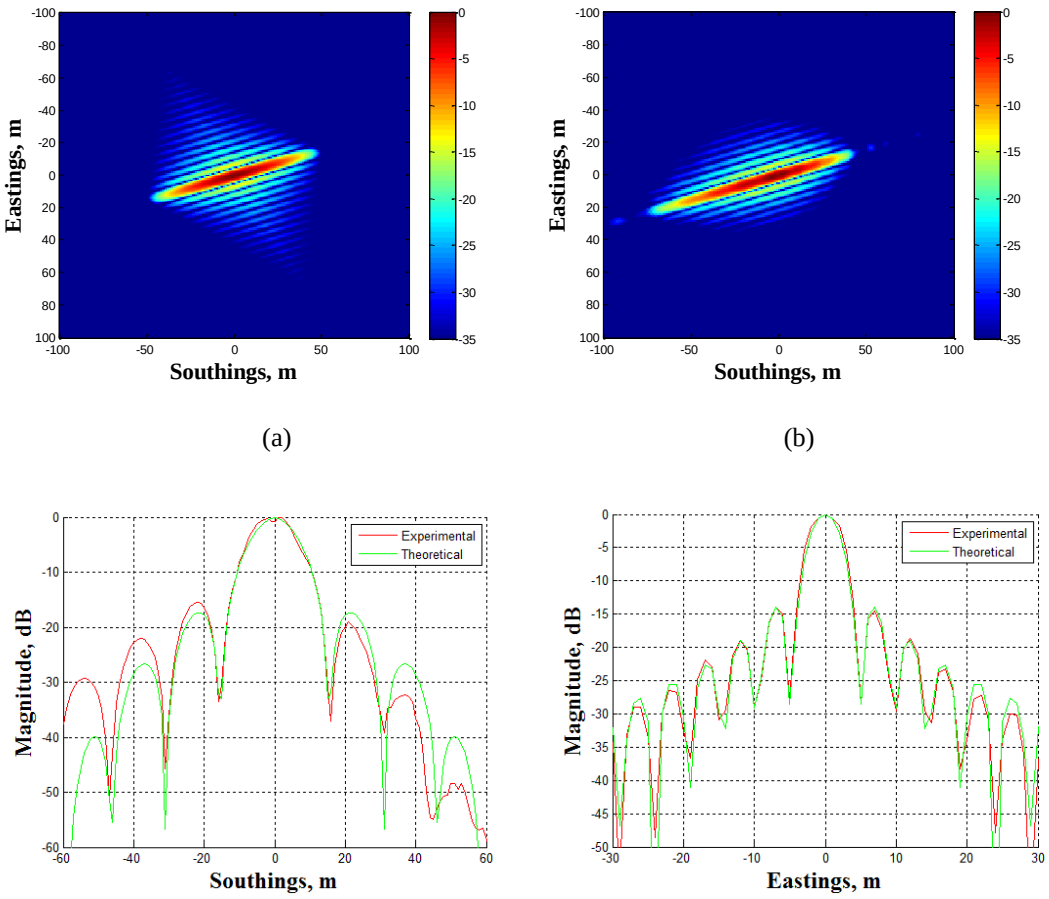

Figure 5.13: (a) Experimental image from HC, (b) Theoretical image, (c) Cross-sections comparison along South direction, (d) Cross-sections comparison along East direction

Following up, the modified BP algorithm was applied to RC signal. The experimental SS-BSAR image is shown in Fig. 5.14(a). The image is a demonstrated in magnitude, measured relative to the response at the receiver, who has the highest signal intensity. The colour scale is dB, where 0 presents the strongest signal. The dynamic range of this image is cut to -35dB. It is noteworthy that the noise floor is calculated as -57.85dB from theoretical point of view. If we apply the dynamic range as such a value in our image, however, prominent targets will not be clearly presented, since large-sized response flashes from weaker targets will blur those from targets of interests. Therefore, we adjust the dynamic range manually to give the best image

presentation. This operation will be applied to other images in later texts. The targeting size is from 0 to 500m along South direction and -340m to 340m along East direction.

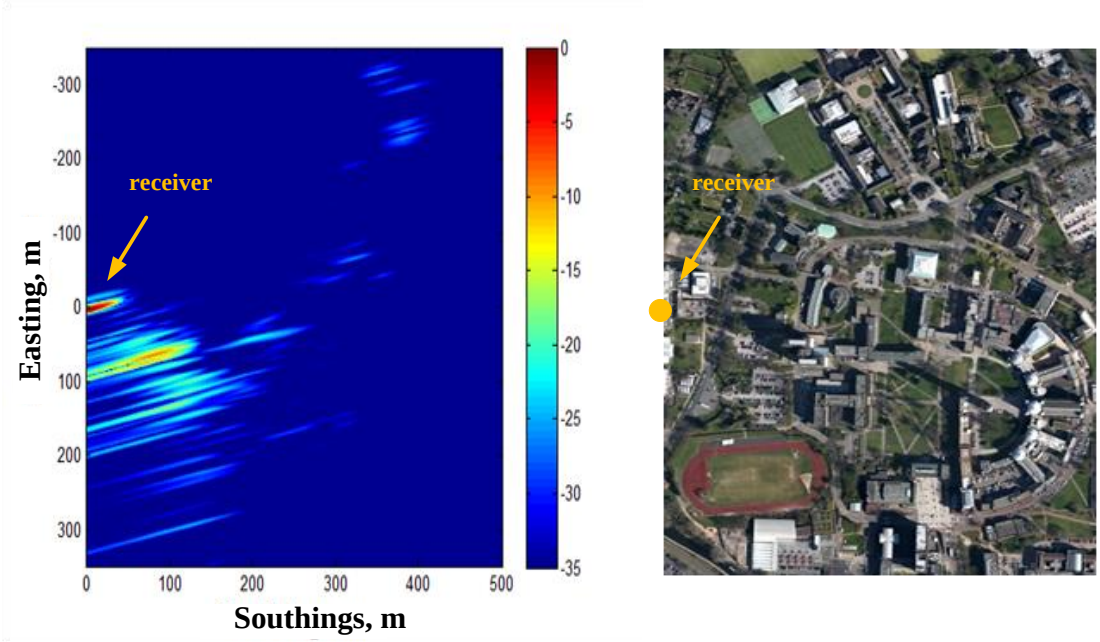

(a) (b)

Figure 5.14: (a) Obtained experimental image from RC signal, (b) Optical photograph of the same area

The cross-sections of signal responses at receiver locations along South and East directions are shown in Fig. 5.15, with theoretical results being superimposed on.

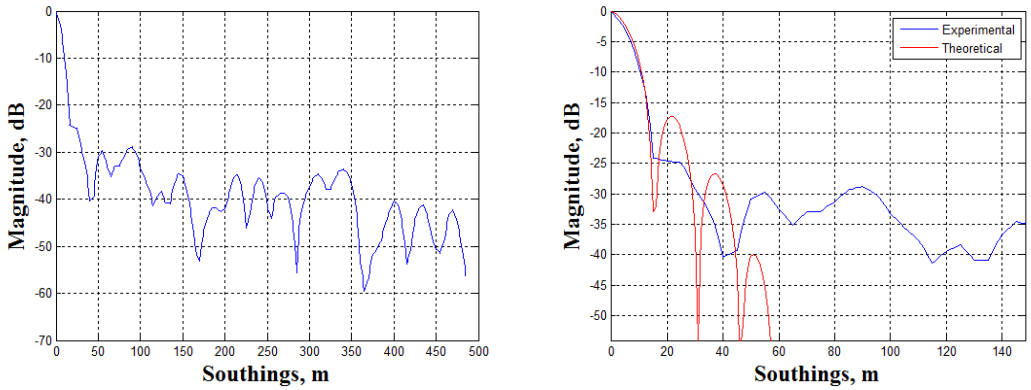

(a) (b)

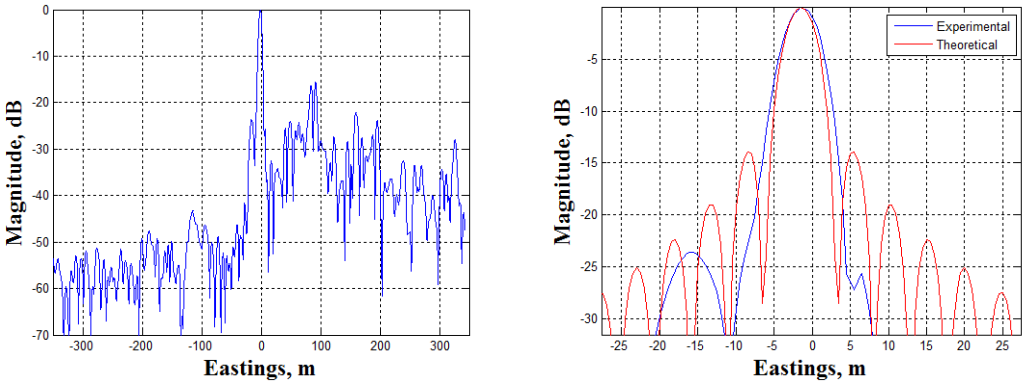

(c) (d)

Figure 5.15: (a) Cross-section along South direction, (b) Zoomed plot of (a) overlaid with theoretical result, (c) Cross-section along East direction, (c) Zoomed plot of (c) overlaid with theoretical result

Beginning with cross-section along South direction, several point targets may be found at this direction. All of which are at least -45 dB below the receiver response, but above the noise floor of -57.85 dB. The shape of the responses is not as well defined as that at receiver. This may be explained by multiple scatters enclosed in coarse resolution cells. With regard to cross-section along East direction, multiple targets were found at the right side of main-lobe, all of which are more than -40 dB relative to that at receiver. These can be explained by side-lobes from other targets closer to receiver. At left side, however, the responses of targets are weak and the noise floor may have been observed (i.e. -57.85 dB relative to receiver response). It is expected, as can be seen from real scene (Fig. 5.8) that this area has been shadowed.

The resolutions along South direction and East direction are also found by measuring half power widths in Fig. 5.15(b) and (d). Table 5.6 gives the experimental and theoretical results.

	Resolution at South direction (m)	Resolution at East direction (m)
Theoretical result	11.6	4.3
Experimental result	11.5	4.5

Table 5.6: Theoretical and experimental resolutions at South and East directions

It is observed from Table 5.6 that the experimental resolutions measured along South direction and East directions are 11.5m and 4.0m respectively. Furthermore, inspection of Fig. 5.16 and Table 5.6 demonstrates a high similarity between experimentally measured resolutions and theoretical counterparts along both directions. It is apparently at this point at RC signal is fully focused in all area at receiver location.

A Kaiser window (Fig. 5.16(a)) was performed in frequency domain to image (Fig. 5.14(b)) along East direction to reduce the side-lobe. After converting to time domain, it could be found that the side-lobe has been reduced in large extent (Fig. 5.16(b, c)). The drawback is the broadening of the main-lobe, resulting in a poorer resolution. To make a balance between side-lobe reduction and resolution deterioration, proper input parameter of Kaiser window should be found. In this data, $\beta = 70$ is selected for the input of Kaiser window. The image after windowing at East direction is shown in Fig. 5.16(d).

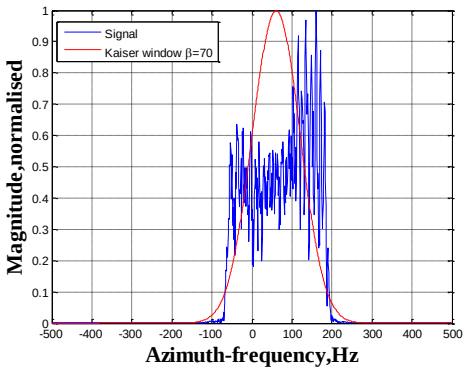

(a)

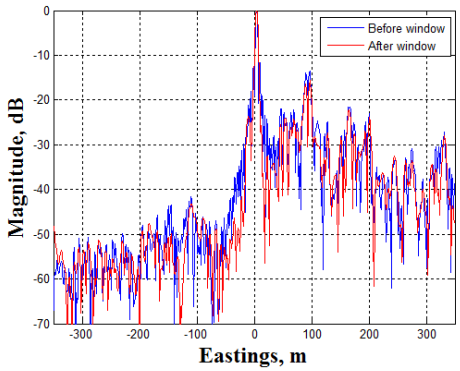

(b)

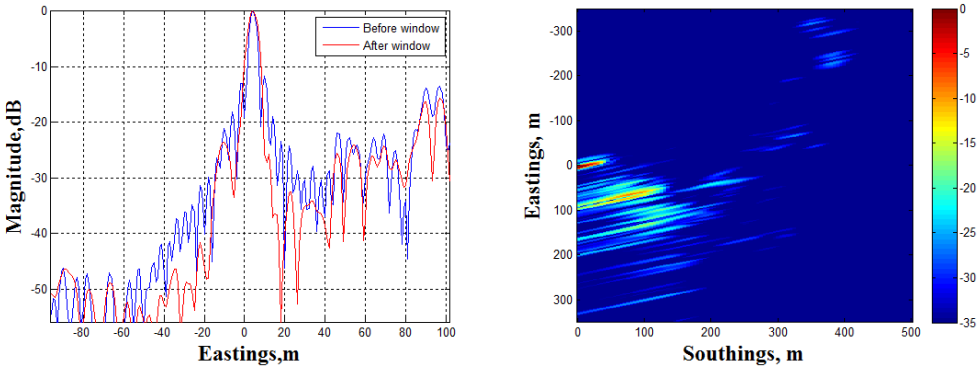

(c) (d)

Figure 5.16: (a) Signal spectrum in Y direction overlapped with Kaiser window, (b) Point impulse response between and after windowing, (c) Zoomed plot of (b), (d) Image after windowing at East direction

It could be found that, the signal at receiver has the highest intensity, as expected due to direct signal absorbed at RC antenna through back-lobe. Moreover, there are number of other signals in the image area whose signal intensity varies with the distance between receiver and targets, as expected according radar equation. Due to that high signal intensity at receiver location largely obscures other target returns, especially those far away (e.g. 400m at South direction), the first 80m of image in Fig. 5.16(d) has been discarded and showed in Fig. 5.17.

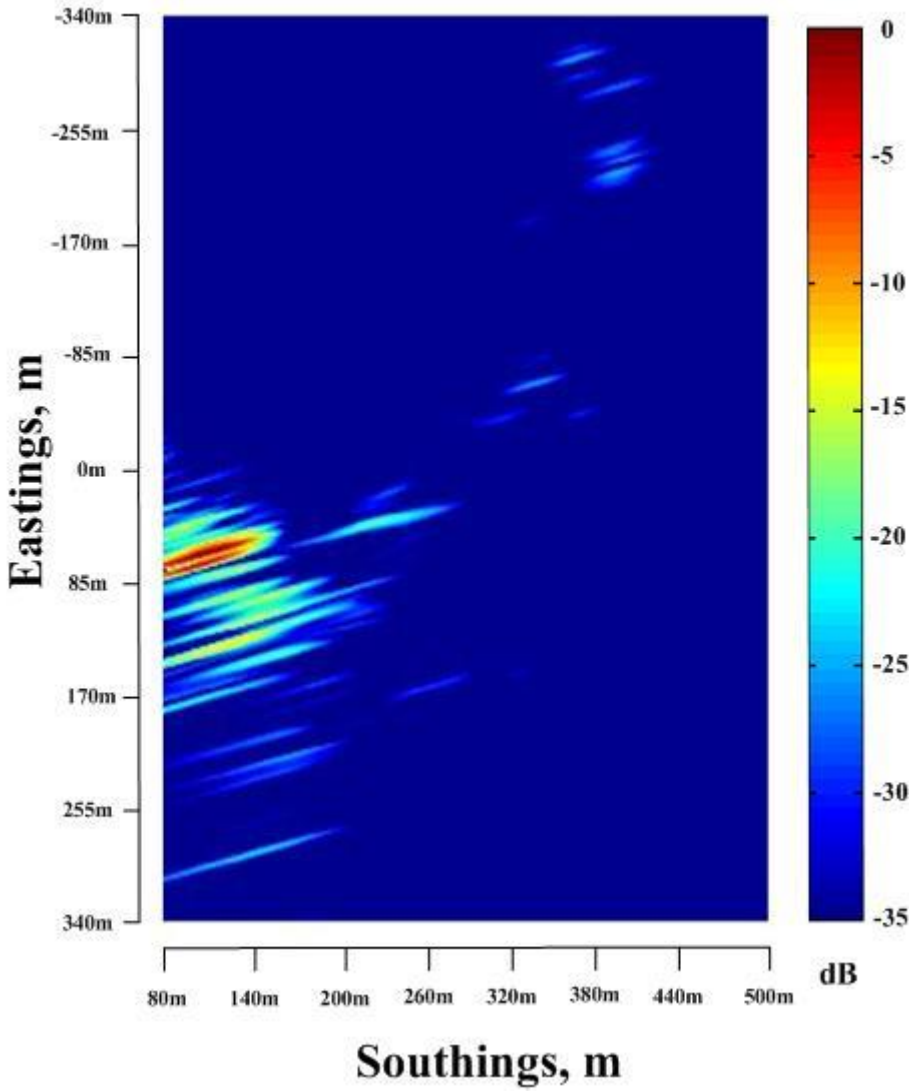

Figure 5.17: SS-BSAR image (after discarding image of receiver)

It could be seen that without receiver, under colour dynamic range of 35 dB, the Muirehead tower and other buildings are more visible and contrast with background. Due to low resolution characteristic of our SAR system, the target response is a long ellipsoid shape flash extended up to 80m in South direction, which may include a number of ground features. An individual object will not be distinguishable by image inspection alone. As such, it is more constructive to examine the image by superimposing it with optical photograph of the same area.

Fig. 5.18 shows the overlapped plot of obtained SAR image and satellite photograph from Google Earth. Inspection of this image demonstrates that the main target buildings (i.e. Muirehead tower, Library, Arts building, Barber institute of fine art, Birmingham business school) can be clearly seen in SAR image and are located at the same positions as on the optical photograph. Moreover, the areas that do not have signal return is shadow area (marked with rectangular), which are either grassy lands or impeded by high buildings. It is apparently that this image is well focused.

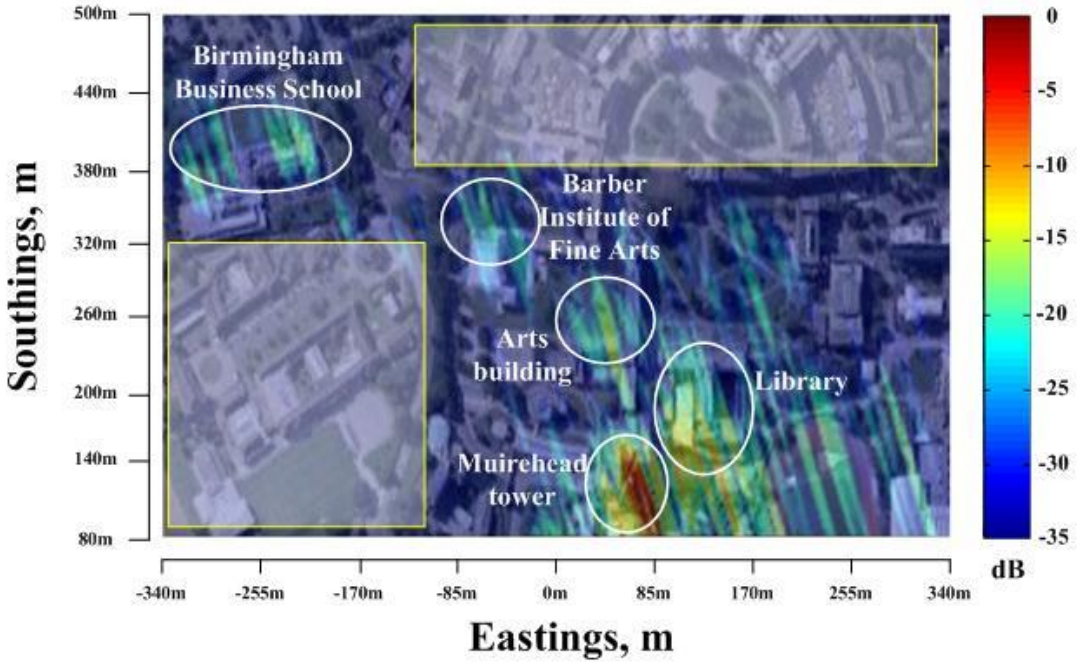

Figure 5.18: Obtained SS-BSAR image superimposed on optical photograph from satellite

The reflectivities of predominant targets relative to magnitude measured at receiver are listed in Table 5.7.

Feature	Max magnitude relative to receiver response (dB)	Max magnitude relative to noise floor (dB)
Muirehead Tower	-8.02	49.83
Library	-16.76	41.09
Arts Building	-21.87	35.98
Barber Institute of Fine Arts	-26.17	31.68
Birmingham Business School	-26.29	31.56

Table 5.7: Reflectivity of prominent targets

It can be observed from Table 5.7 above that the buildings at nearer end gives the higher signal intensity, as expected, given they responds to the smaller range to the receiver.

5.4 Vale village site

Experiment overview

This experiment was conducted in Feb. 29th 2012 in the campus of UOB. The same receiver used for previous experiments was placed on the roof of School of Electronic, Electrical and Computer Engneering pointed to the targeting area in North direction (Fig. 5.19(a)). The satellite was GLONASS COSMOS 744, moving at elevation angle round 66^{o} relative to location of receiver and azimuth angle around 179^{o} with regard to North direction. The satellite path projection on the local ground is marked with yellow dash line in Fig. 5.19(a). It can be observed that such geometry is almost quasi-monostatic (Definition seen in Chapter 2). Another photograph of this area taken from location of observation is shown in Fig. 5.19(b).

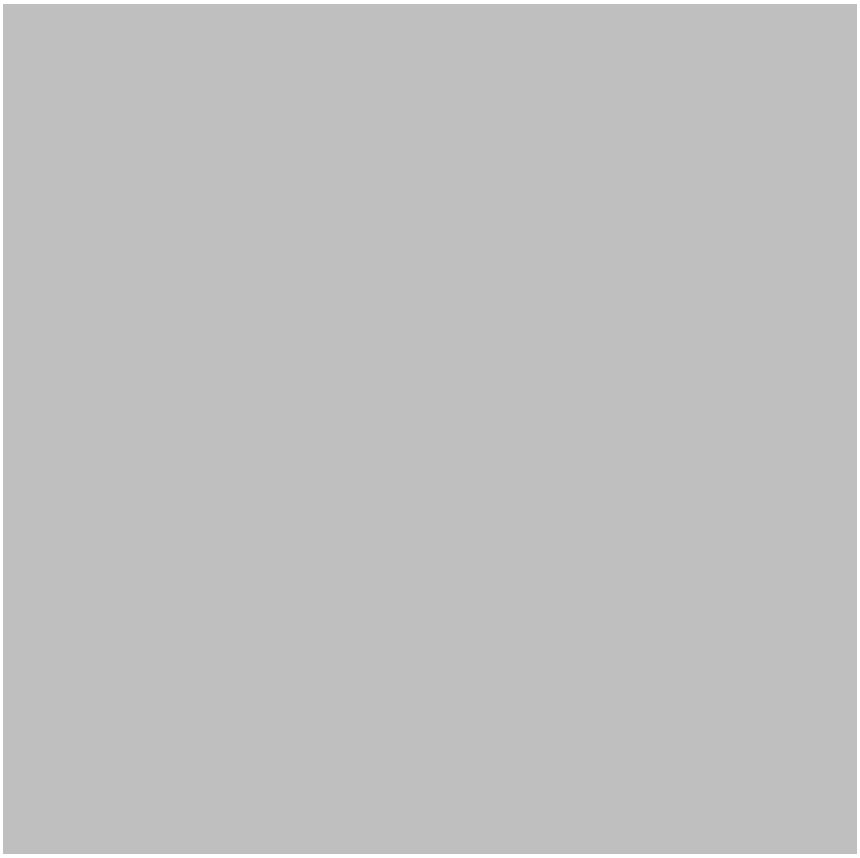

(a)

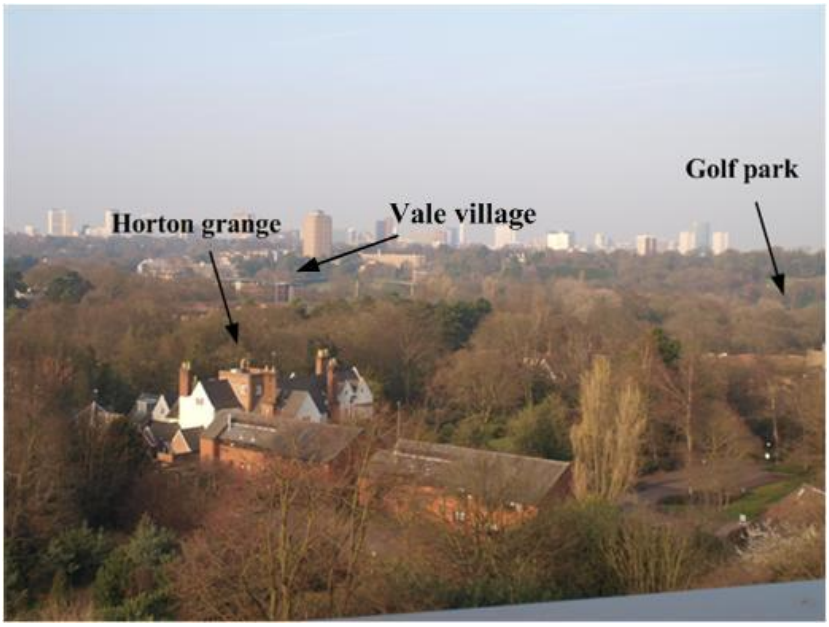

(b)

Figure 5.19: (a) Imaging scene superimposed on local coordinate frame, (b) Photograph taken from the location of observation

There are a number of features that have been found as the targets for imaging. In the sequence of ascending range to receiver, they are Horton grange, Green house, Tennis close, Vale village and Golf park terrain. The positions and height of them are listed in Table 5.8.

Feature name	Geographic location (m)		
	Range	Cross-range	Height
Horton grange	160	80	60
Green house	200	120	20
Tennis close	400	-300	10
Vale village	310	-60	10
Golf park terrain	250	70	15

Table 5.8: Positions and heights of main features in the imaging scene

Apart from those features above, it can be observed that the experimental site is occupied by trees, grasses and waters, from where low signal reflectivity is expected.

The experimental parameters are given in Table 5.9.

Parameter	Value
Transmitting satellite	GLONASS COSMOS 744
Carrier frequency	1604.8125MHz
Satellite signal used	P-code (L1)
Signal bandwidth	5.11MHz
Satellite elevation	$68^o - 65^o$
Satellite azimuth	$180^o - 178^o$
Integration time	250s
Bistatic angle	171^o
PRF used for signal processing	1000Hz

Table 5.9: Experimental parameters

From Eq. (2.21) and (2.22), the SNR at receiver location in RC image and power budget for targets at varying ranges are shown in Fig. 5.20.

$$SNR_{img} = 26 + 10 \times log10(5.11 \times 250) = 57.06dB \tag{5.3}$$

It indicates that the noise floor is 57.06 dB lower than that measured at receiver.

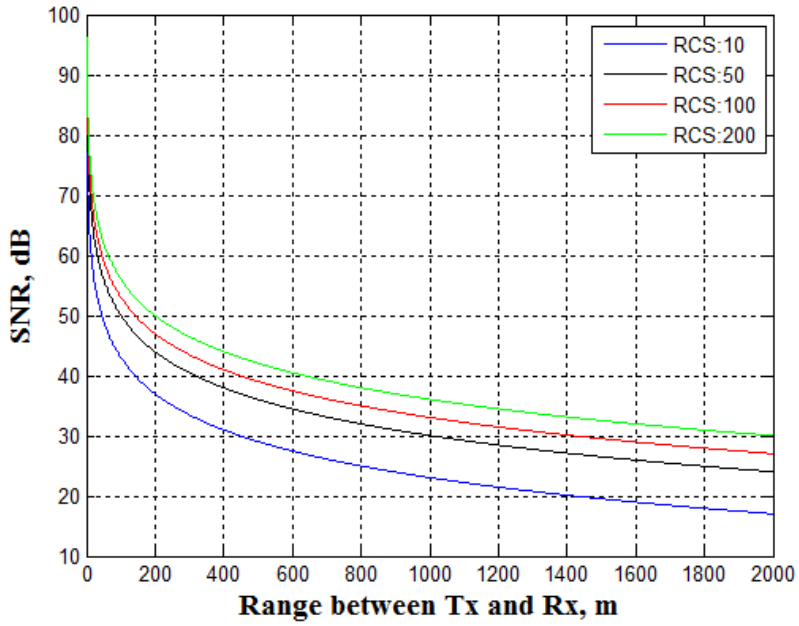

Figure 5.20: RC image target SNR vs. target to receiver range

It could be observed that the magnitude dynamic range of this experiment is smaller than the previous one, due to less integration time perfomed. In addition, same as before, the receiver may obscure most targets.

Signal synchronization

Fig. 5.21 shows the signal synchronization outputs of acquired HC data. They are with the same content as before. The slow-time signal becomes periodic and its spectrum becomes flat after removing navigation message, and image can be obtained after azimuth compression in this dimension.

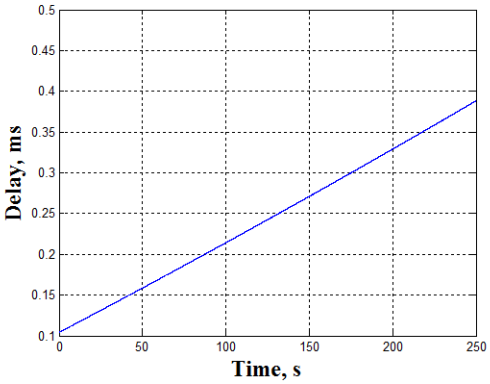

(a)

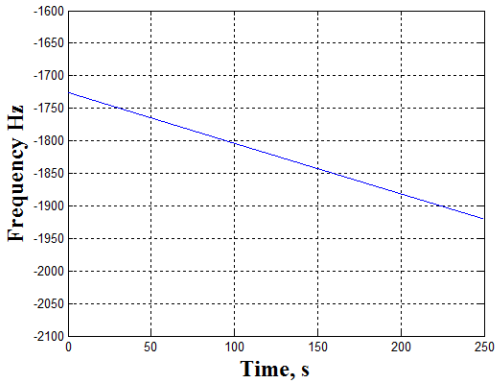

(b)

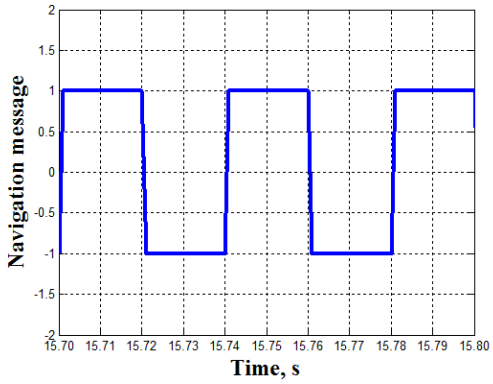

(c)

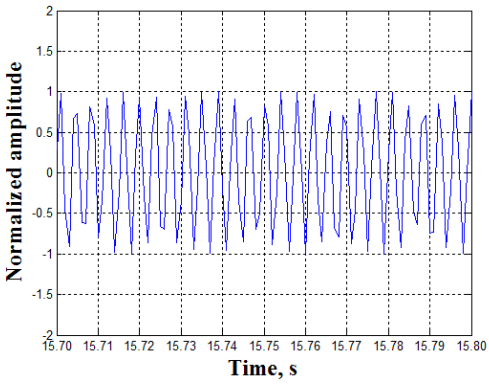

(d)

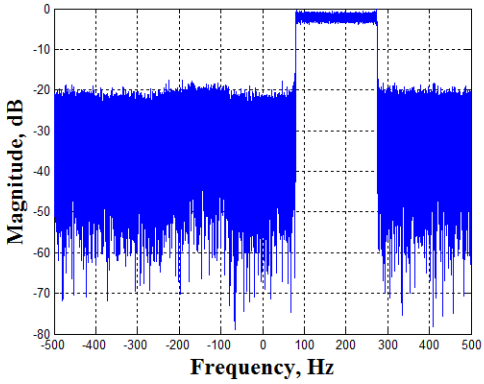

(e)

Figure 5.21: (a) P-code delay, (b) P-code Doppler, (d) P-code slow-time signal spectrum (with navigation message), (e) P-code decoded navigation message, (f) P-code slow-time signal (without navigation message), (g) P-code slow-time signal spectrum (without navigation message)

The HC range compressed signal and cross-sections in both fast time and slow time dimensions are presented in Fig. 5.22. Again, it could be found that the delay, Doppler, phase terms and navigation messages are all well tracked in HC signal.

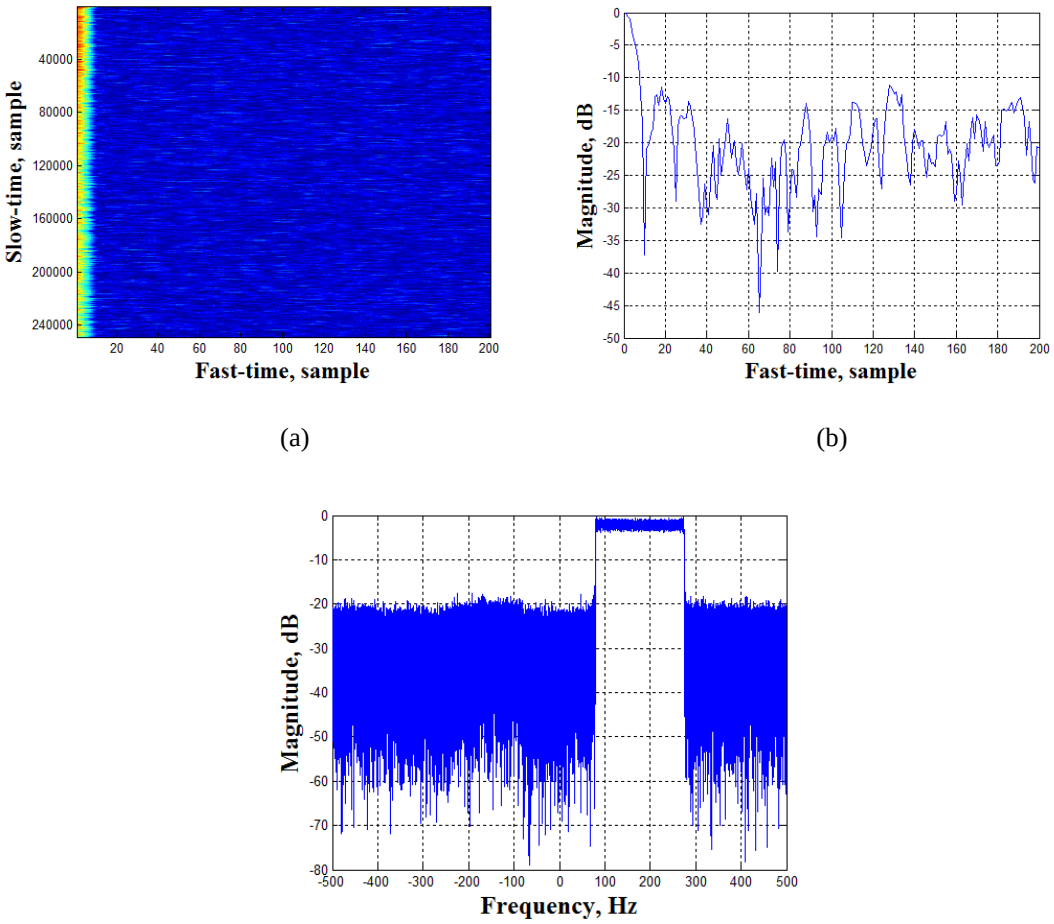

Figure 5.22: (a) HC range compressed signal, (b) Cross-section along fast time, (c) Slow-time signal spectrum (after navigation message decoding)

Experimental imagery and analysis

The obtained experimental image from RC is given in Fig. 5.23. Same as previous experiment, the colour scale applied is in dB and dynamic range is cut to -35dB. The image size is from -1000m to 200m along West direction and from 0m to 1000m along North direction. Coordinate (0,0) is where the receiver is located.

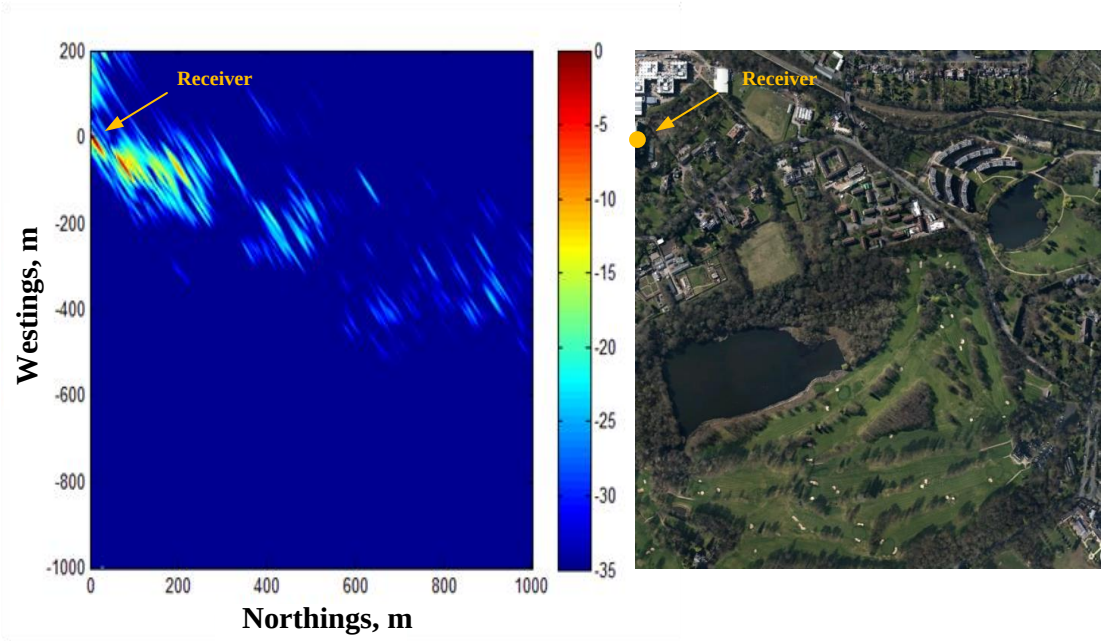

(a) (b)

Figure 5.23: (a) Obtained experimental image from RC, (b) Optical photograph of the same area

The cross-sections of response at receiver in North and West directions are shown in Fig. 5.24(a) to (d), in which Fig. 5.24(b) and (d) are the enlargement of Fig. 5.24(a) and (c) respectively and superimposed by their theoretical counterparts.

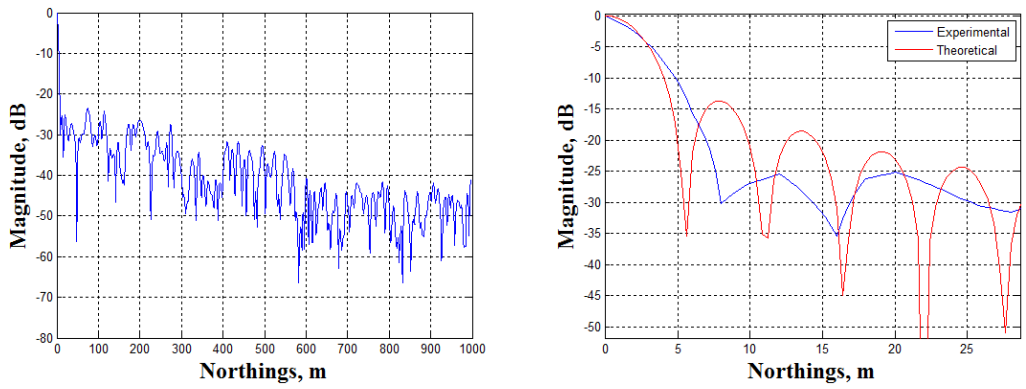

(c) (d)

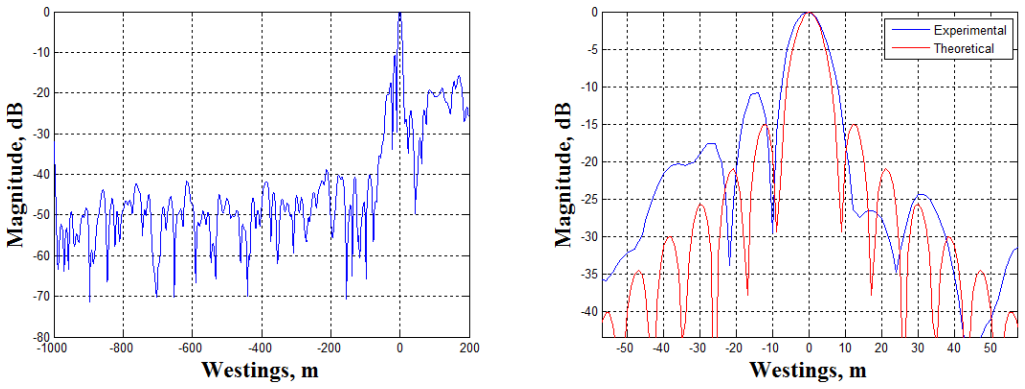

(e) (f)

Figure 5.24: (a) Cross-section at receiver along North direction, (b) Close-in plot of (a) superimposed on theoretical result, (c) Cross-section at receiver along West direction, (d) Close-in plot of (c) superimposed on theoretical result

Inspection of Fig. 5.24 (a) and (c) shows that, with regard to target responses along North direction, multiple responses may be observed within range of 600 m. This can be explained by reponses of features as well as reflections from terrain within this area. Result outside 600m shows the noise floor (i.e. -57.06dB) mixed with weak return, as expected due to this area is mainly consisted of grassy lands. Along West direction, there are strong signal responses up to -20 dB relative to receiver response at right side of mainlobe, this may be explained by scattering from neighbouring objects. At right side of receiver, however, the signal magnitudes are much lower. The magnitude varying zone between -60 dB to 50 dB contains noise floor, indicating that the signal in such area is consisted of noise and reflections of grassy terrain as expected.

The resolution of receiver responses along two directions experimentally measured at -3 dB width of the mainlobe gives 4.0 m and 7.4 m along North and West direction, which are 0.1 m less and 0.5 m more than theoretical results respectively.

After applying Kaiser window to data along West direction and discarding the first 100m along North direction, the same processing as before, the experimental RC image is shown in Fig. 5.25. The image is plotted using dB colour-scale, and the dynamic range is cut to -30dB. The imaging size is from 100m to 1000m along North direction and from -1000m to 200m along West direction. The orientations of all the target responses are the same, pointing to Northeast direction. The signal intensities become weaker at far distance, as expected due to larger path loss.

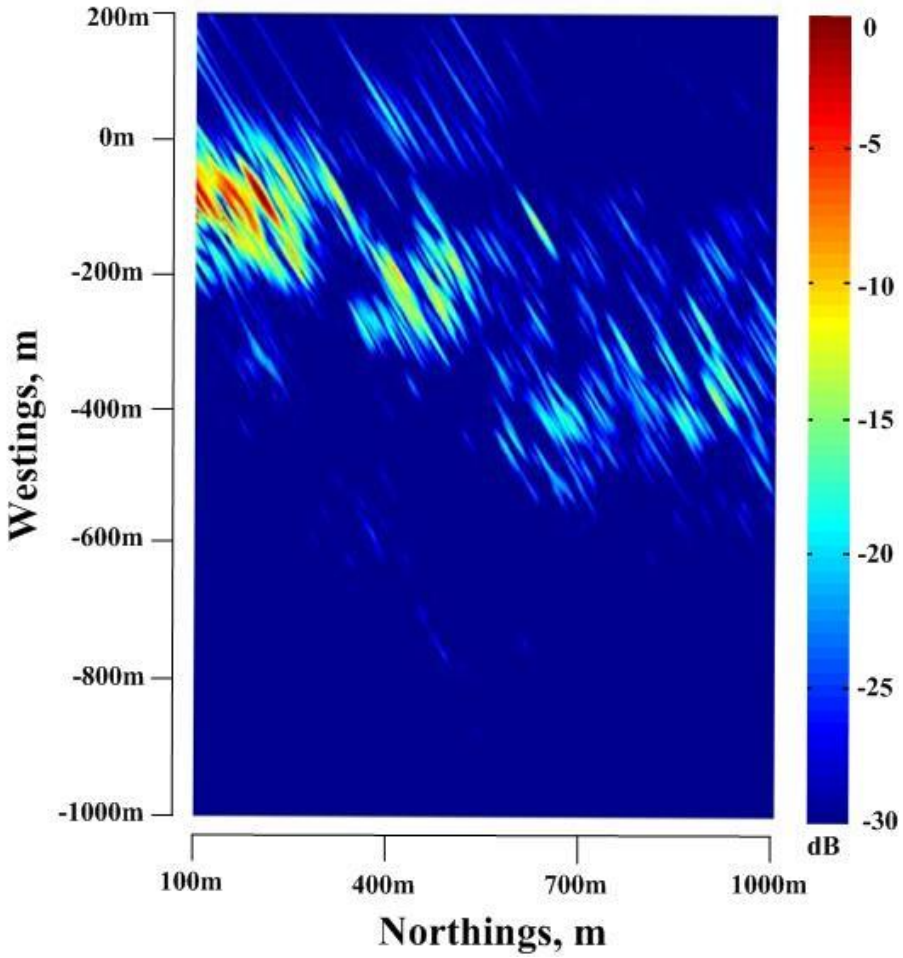

Figure 5.25: SS-BSAR image (after discarding image of receiver)

The bistatic image overlaid with satellite photograph of the same area is provided in Fig. 5.26. The prominent features (1: Horton grange, 2: Green house, 3: Tennis close, 4: Vale village and 5: golf park terrain) are marked with ellipsoids and grassy lands

are marked with shadowed rectangles. Inspection of Fig. 5.26 indicates that the SAR image is well corresponding to optical photograph in terms of signal intensity.

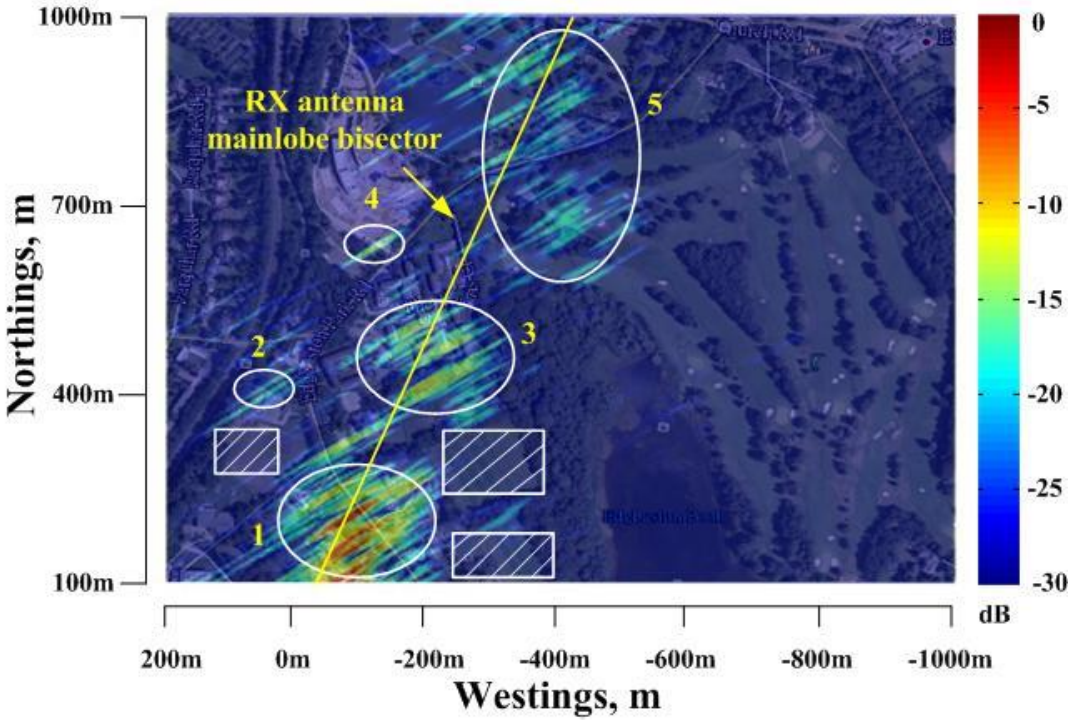

Figure 5.26: SS-BSAR image superimposed on satellite photograph of the same area

The reflectivity of the five features relative to measured at receiver is listed in Table 5.10.

Features	Max magnitude measured relative to receiver (dB)	Max magnitude measured relative to noise floor (dB)
Horton grange (1)	-4.91	52.51
Green house (2)	-24.82	32.24
Tennis close (3)	-21.21	35.85
Vale village (4)	-17.98	39.08
Golf park terrain (5)	-23.07	33.99

Table 5.10: Target reflectivity parameters

It is observed that Horton grange provides the highest signal return, as expected due to smallest range. Green house has the second smallest range, however, due to smaller

size (RCS may be less) and plastic materials (but steel frame), small signal return is expected. Vale village is far from receiver, however, its shape is fairly like a mirror, and therefore strong reflection is also expected. All the features will be analyzed in details in following texts.

The image of Horton grange area is shown in Fig. 5.27. Fig. 5.27(a) is the satellite photograph of this area and Fig. 5.27(b) is the corresponding experimental SS-BSAR image superimposed on the satellite photograph. From Fig. 5.27(b), it has been seen that a series of multiple targets makes it difficult to achieve one-to-one coincidence between optical image and SAR image. This is likely to be resulted from that the roofs of Horton grange (marked with yellow circle in Fig. 5.27(a)) is made up of numbers of trihedral and dihedral reflectors. However, a coarse correspondence could still be achieved, i.e., the four yellow circles in Fig. 5.27(a) Coincide four black squares in Fig.5.27(b).

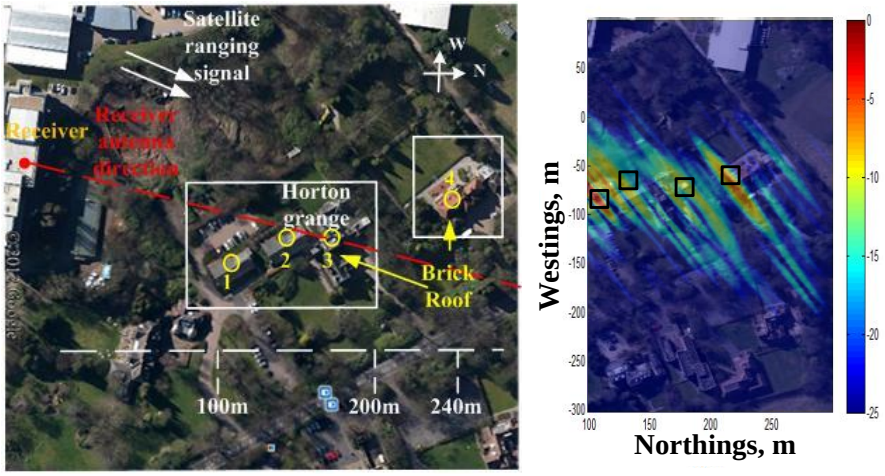

(a) (b)

Figure 5.27: Close-in image of Horton grange area (a) Satellite optical photograph, (b) SS-BSAR image superimposed on optical counterpart

The cross-sections of highest signal response are shown in Fig. 5.28. The theoretical results are superimposed on experimental one. The back circles in Fig. 5.28(a) presents four back square in Fig. 5.28(b). It can be seen from Fig. 5.28(a) that the two middle circles consist of two peaks, probably due to irregular shape of those buildings. The experimental and theoretical half power width of highest intensity target along North and West directions are listed in Table 5.10. The inspection Fig. 5.28 and Table 5.11 shows that there is a high level of similarity between theoretical and experimental results for this particular target.

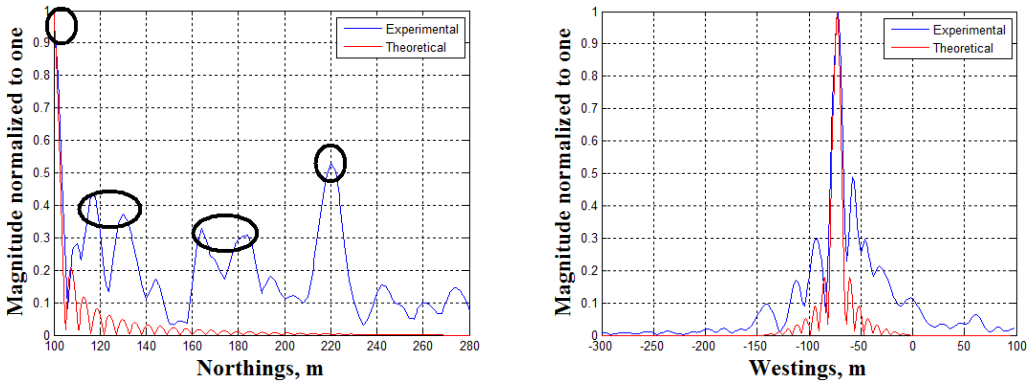

(a) (b)

Figure 5.28: Comparison between experimental cross-sections and theoretical counterparts: (a) at North direction, (b) at West direction

	-3dB width at North direction (m)	-3dB width at West direction (m)
Theoretical width	3.9	6.9
Experimental width	4.2	7.2

Table 5.11: Half power width of experimental and theoretical results

Image of Vale village building were examined at next stage. Fig. 5.29(a), (b) and (c) show optical photograph taken in front of the building, the obtained SS-BSAR image and the corresponding theoretical PSF. It can be found that such a building has a flat face, which may results in specular reflection. Same orientation and flash shape have

been observed between Fig. 5.29(b) and (c), indicating well image focus. Nevertheless, the experimental one is a bit fatter than theoretical counterpart, this may be due to that little residual phase is not fully removal in image formation stage

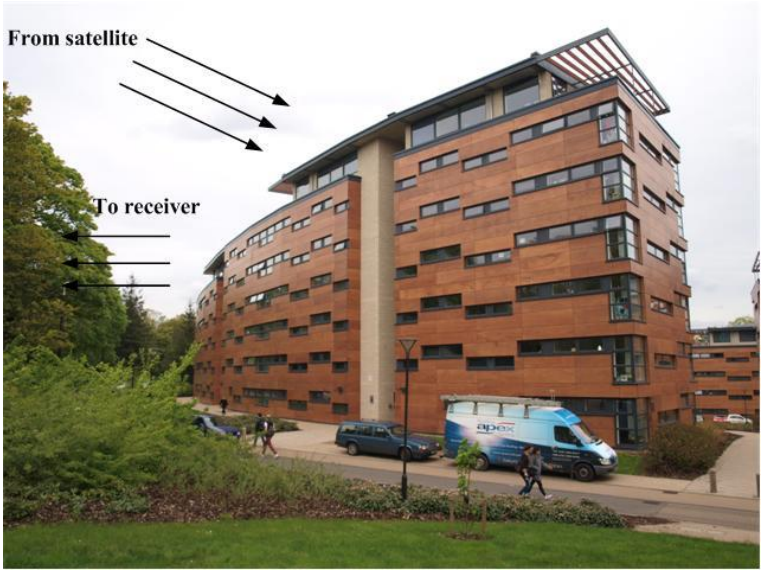

(a)

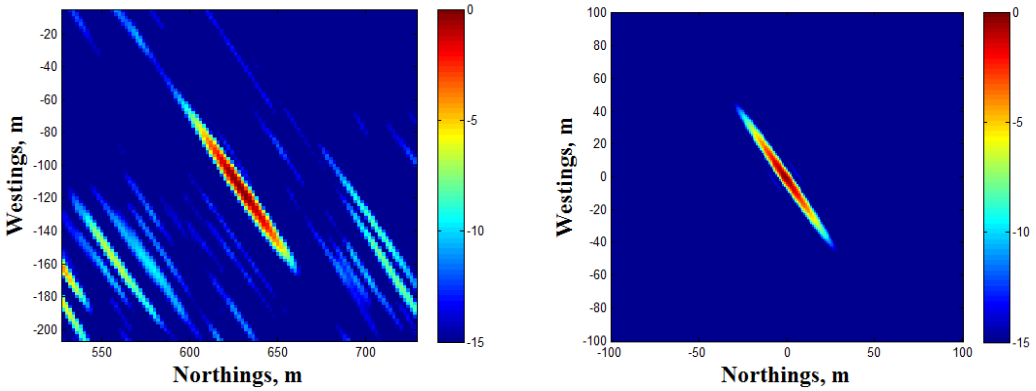

(b) (c)

Figure 5.29: Image of Vale village: (a) Optical photograph, (b) Experimental image, (c) Theoretical image

With regard to -3dB widths along North and West direction, the measured values are 4.2m and 7.2m respectively, which are parallel with the theoretical values of 3.9m and 6.9m. In addition, as mentioned below, such a isolated building can be well served as a reference target for resolution analysis.

Now let's go to examine green house image, Fig. 5.30(a) shows the satellite image of this area, and Fig. 5.30(b) is the SS-BSAR image of this area superimposed on optical counter part. Fig 5.31(a) and (b) present the cross-sections along North and West directions. Examination of Fig. 5.30(a) finds that the green house site is consisted of one main big house and a couple of small houses. The dimensions of overall targets along two directions are 60m and 60m respectively. The main object green house is covered with plastic-like materials, and the frame is made of steel. The roof is made up of multiple dihedral and trihedral reflectors. As such, it is difficult to make a prediction of how much returns will arrive at receiver and what are their intensities. From Fig. 5.31 and Fig. 32, it can be observed that coarse correspondence between the experimental response and real dimension can be made. Nevertheless, careful investigation of responses in this area is needed.

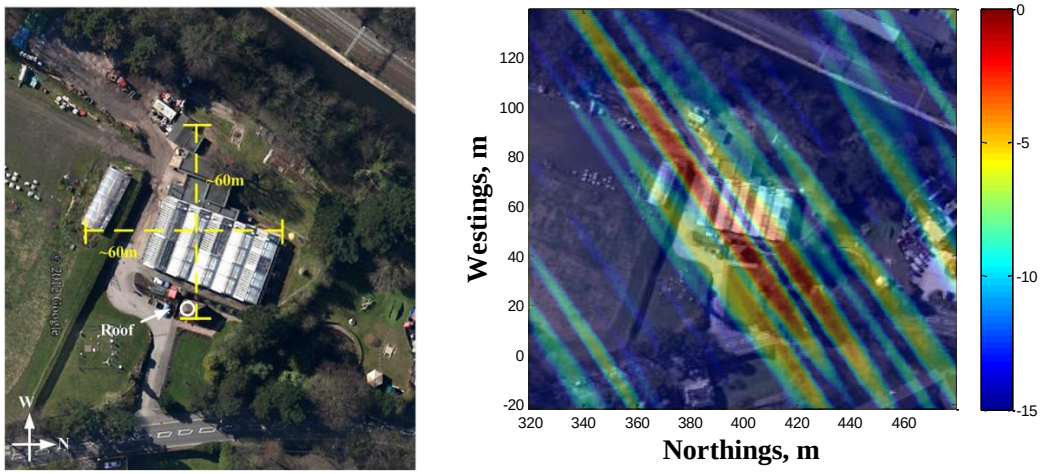

(a) (b)

Figure 5.30: Image of green house (a) Satellite photograph (b) SAR image superimposed on satellite photograph

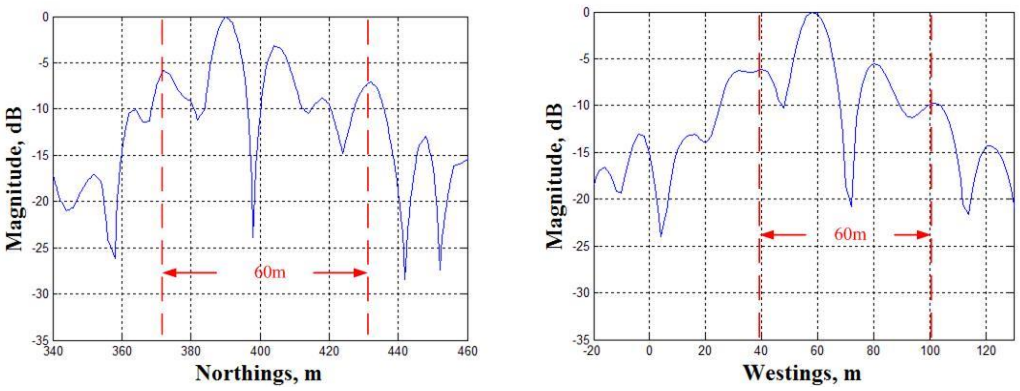

(a) (b)

Figure 5.31: (a) Cross-section along North direction, (d) Cross-section along West direction

It is well worth noticing the returns from golf park (marked with circle 5 in Fig. 5.26). This area is a grassy land with scattering trees and waters, and there are no prominent buildings nearby. However, certain amount of signal return is expected. The elevation profile along the RC antenna illumination angle obtained from Google Earth is shown in Fig. 5.32. It could be observed that the terrain increase after 700m makes it like a mirror. When the satellite signal comes across it, a fraction of echoes would be reflected back to the receiver.

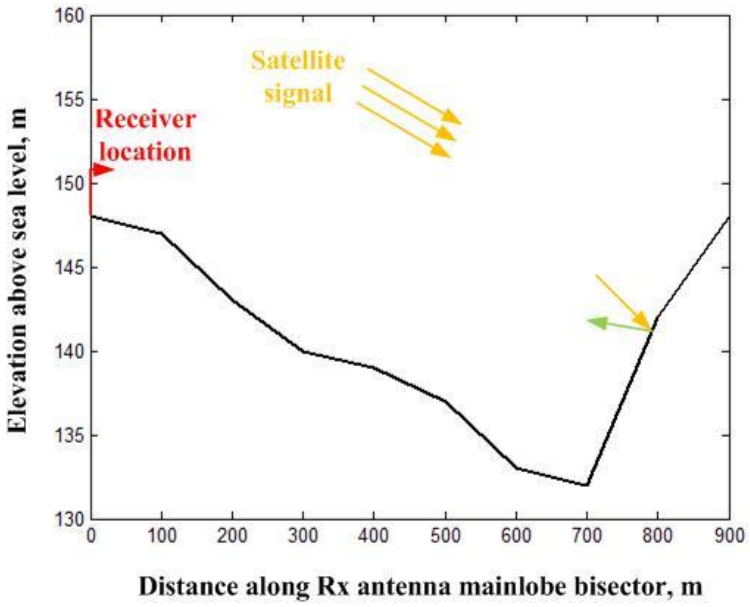

Figure 5.32: Elevation profile of Vale village site along RC antenna illumination angle

5.5 Metchly park site

Experimental overview

This experiment was conducted in July 24th 2012. Receiver is again located on the roof of School building of Electronic, Electrical and Computer Engineering in UOB. The target area is at the West direction of receiver (Fig. 5.33(a)). This area features with large area of empty grassy land named Metchley park (marked with white rectangular), surrounded by a number of buildings (marked with yellow ellipsoid). The RC antenna illumination direction is indicated on Fig. 5.33(a) using white solid line. Inspection of Fig. 5.33(a) indicates that at closer range, there is a large area of lower buildings, which is the Material school in UOB, and at farer range (around 1200m), there are four high buildings separated apart along South direction (Fig. 5.33(b)). Moreover, between the two grassy lands, there are two lines of trees. Our aim is to get image of this area. We were expecting that the signal responses gathered near the receiver, and there are four distinguish flashes at the positions of four buildings, while there are less signal returns in between expect from the trees.

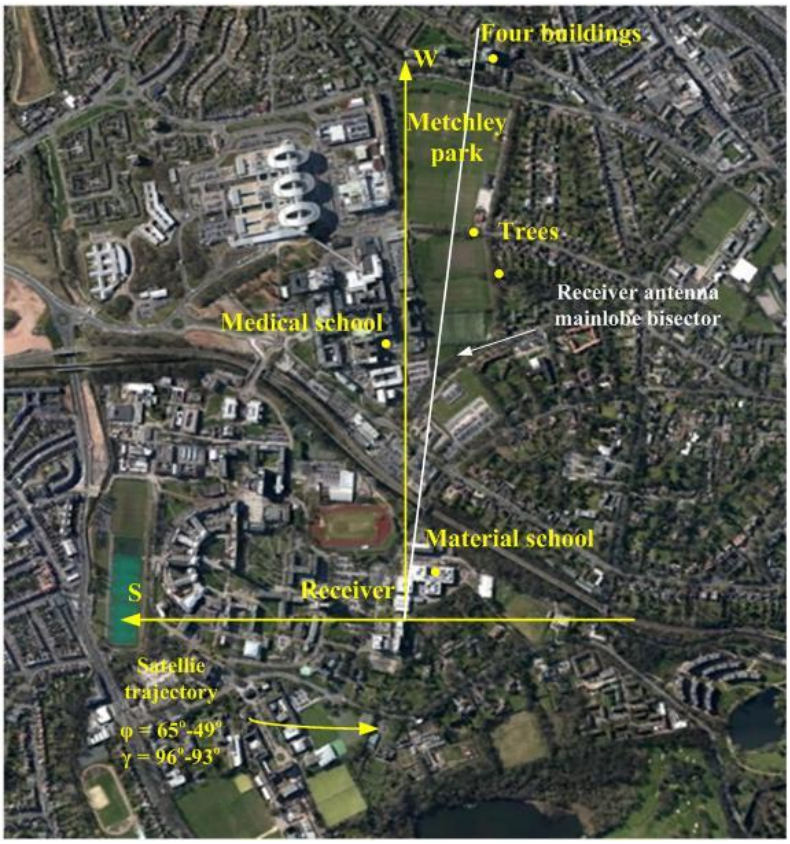

(a)

(b)

Figure 5.33: (a) Satellite photograph of full target area superimposed on local coordinate frame, (b) Four buildings photograph at far end of imaging scene

The transmitter is GLONASS COSMOS 736 and data acquisition took 200 seconds. The experimental parameters are listed in Table 5.12

Parameter	Value
Transmitting satellite	GLONASS COSMOS 736
Carrier frequency	1600.3125MHz
Satellite signal used	P-code (L1)
Signal bandwidth	5.11MHz
Satellite elevation angle	$65^o - 49^o$
Satellite azimuth angle	$96^o - 93^0$
Integration time	200s
Bistatic angle	63.6^o
PRF used for signal processing	1000Hz

Table 5.12: Experimental acquisiton parameters

From Eq. (2.21) and (2.22), the SNR at receiver location in RC image and power budget for targets at varying ranges are shown in Fig. 5.34.

$$SNR_{img} = 26 + 10 \times log10(5.11 \times 200) = 56.09dB \tag{5.4}$$

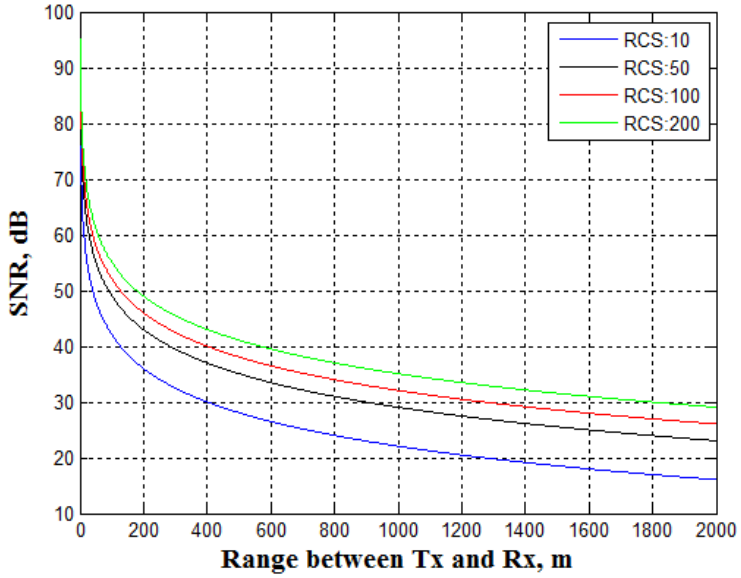

Figure 5.34: RC image target SNR vs. target to receiver range

Again, the target with RCS of $50m^2$ can still be detected at distance of 1000m if dwell time 200s is applied. Also, signal magnitude at receiver may be the highest in the obtained image.

Signal synchronization

The HC signal synchronization is performed by using the same methods as before, the results given by Fig. 5.35. Same as before, examination of all the plots indicates that the delay, Doppler, phase and navigation has been tracked correctly.

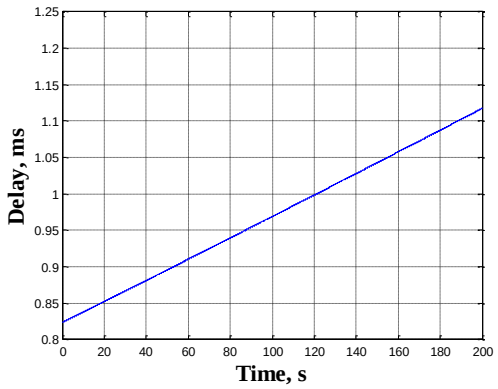

(a)

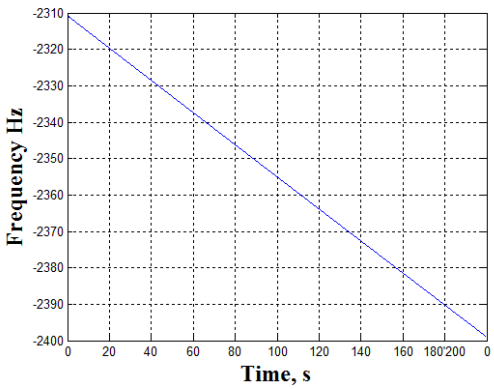

(b)

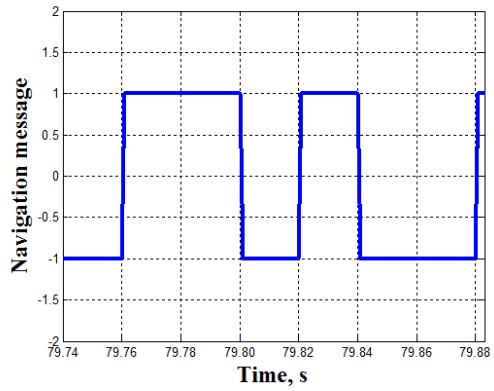

(c)

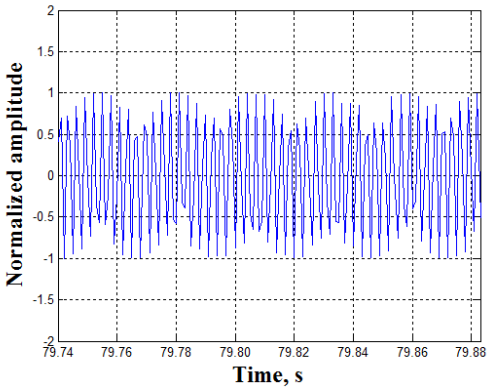

(d)

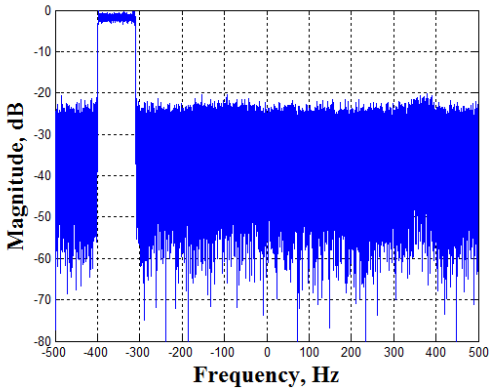

(e)

Figure 5.35: (a) P-code delay, (b) P-code Doppler, (c) P-code decoded navigation message, (d) P-code slow-time signal (without navigation message), (e) P-code slow-time signal spectrum (without navigation message)

The HC signal range compression is implemented to evaluate synchronization performance. Fig. 5.36(a) to (c) show the range compressed signal and cross-sections along two dimensions individually. It is well demonstrated that, once again, the delay, Doppler, phase and navigation message are well tracked in HC signal.

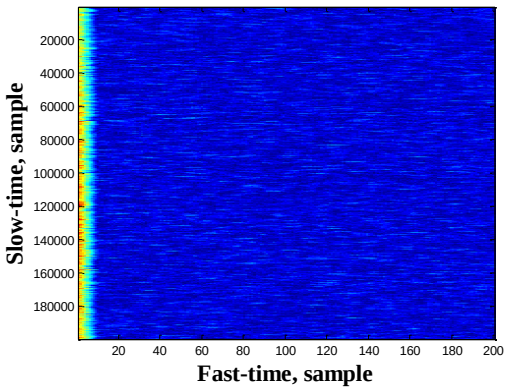

(a)

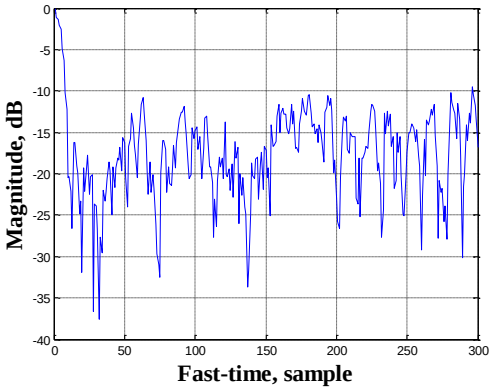

(b)

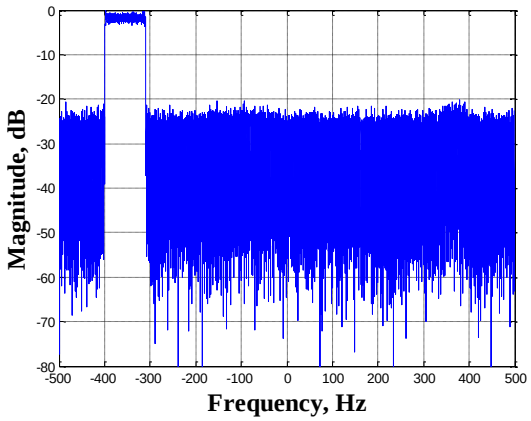

(c)

Figure 5.36: (a) HC range compressed signal, (b) Fast-time direction cross Section, (c) Slow-time signal spectrum (after navigation message decoding)

Experimental imagery and analysis

The experimental SS-BSAR image obtained from RC is given in Fig. 5.37. In Fig. 5.37(a), same as previous images, the colour scale is in dB and dynamic range has been clipped to -45dB. It is noteworthy that in Vale village image, -35dB was set as the dynamic range. However, to make targets at 1250m visible, -45dB is manually set for this image.

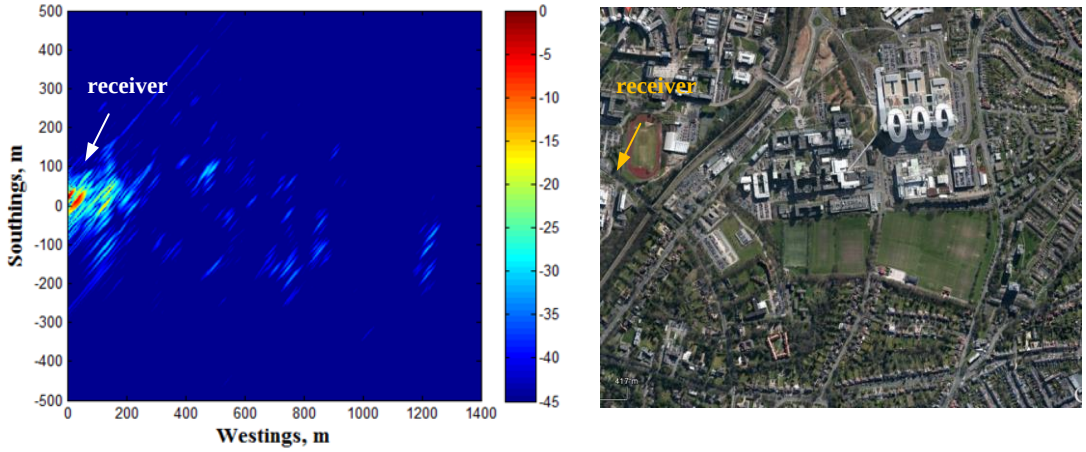

(a) (b)

Figure 5.37: (a) Obtained experimental image from RC, (b) Optical photograph of the same area

Fig. 5.38(a) to (d) show the cross-Sections along two dimensions at receiver, in comparison with theoretical counterparts.

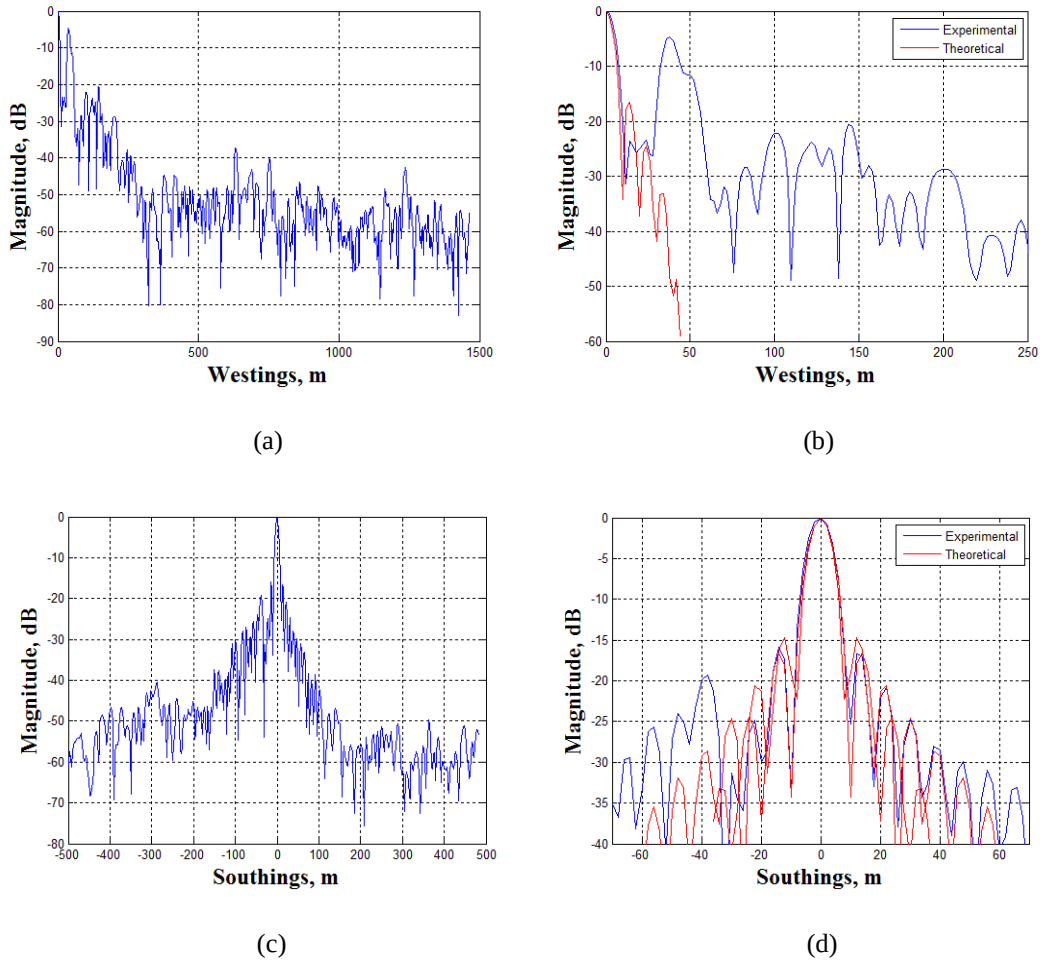

(a) (b)

(c) (d)

Figure 5.38: (a) Cross-Section at receiver along West direction, (b) Close-in plot of (a) superimposed on theoretical result, (c) Cross-Section at receiver along South direction (d) Close-in plot of (c) superimposed on theoretical result

From cross-section along West direction in Fig. 5.38(a), it can be observed that magnitudes of all target returns are higher than 40dB within first 200m, which are at least 16 dB above the noise floor. Moreover, the second peak along West direction is located at 40m away from receiver, and the magnitude is 5 dB less than that of receiver. This can be explained by signal reflected from an extended structured building, i.e. Material School close to receiver. The magnitudes of signals at ranges between 200m and 300m are varying from -55dB to -40 dB, it may due to side-lobe of

the responses of Material School. The signals at ranges exceeding 300m can be seen as noise, since whose magnitude accords with noise floor (i.e. -56.09 dB). The detailed signal reflection from Material School will be described later. The target responses along South direction are examined from Fig. 5.38(c). It can be found that only signals within 200m centered at receiver are targets reflections, while others are likely to be thermal noise. It is noteworthy in Fig. 5.38(d) and (f) that the signal at receiver is fully focused, as little differences of main-lobe can be seen between experimental result and theoretical counterpart, even the side-lobes at right side of receiver along South direction coincide with each other.

The -3dB widths of the main-lobe in Fig. 5.38(a) and (c) indicate the resolution along West and South direction respectively. Table 5.13 gives the experimental and theoretical values of -3 dB width of main-lobes measured at receiver locations.

	Resolution at West direction (m)	Resolution at South direction (m)
Theoretical result	8.6	7.8
Experimental result	8.7	8.9

Table 5.13: Theoretical and experimental resolutions at West and South directions

Inspection of Fig. 5.38 and Table 5.13 indicates high similarity of main-lobes between experimental and theoretical results are performed, and furthermore verifies that the image is fully focused at receiver.

Fig. 5.39 shows the image after windowing along South direction and first 100m being discarded along West direction. The colour dynamic range in this image is cut to -30dB. The response flash is directing to Southwest. Most strong signals gather closer to the receiver. Moreover, signal can be observed at a range of 1250m.

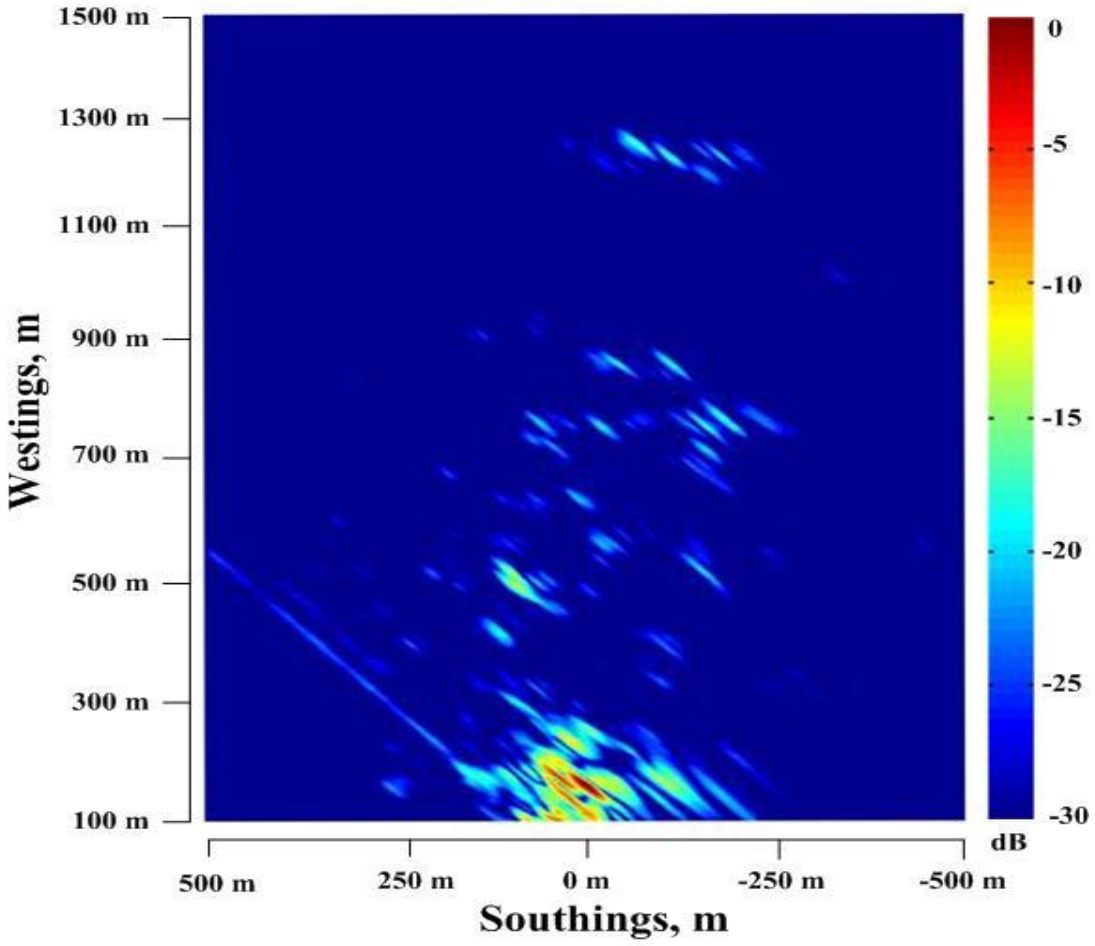

Figure 5.39: SS-BSAR image (after discarding image of receiver)

Fig. 5.40 presents the SS-BSAR image superimposed on a satellite optical photograph of the same area.

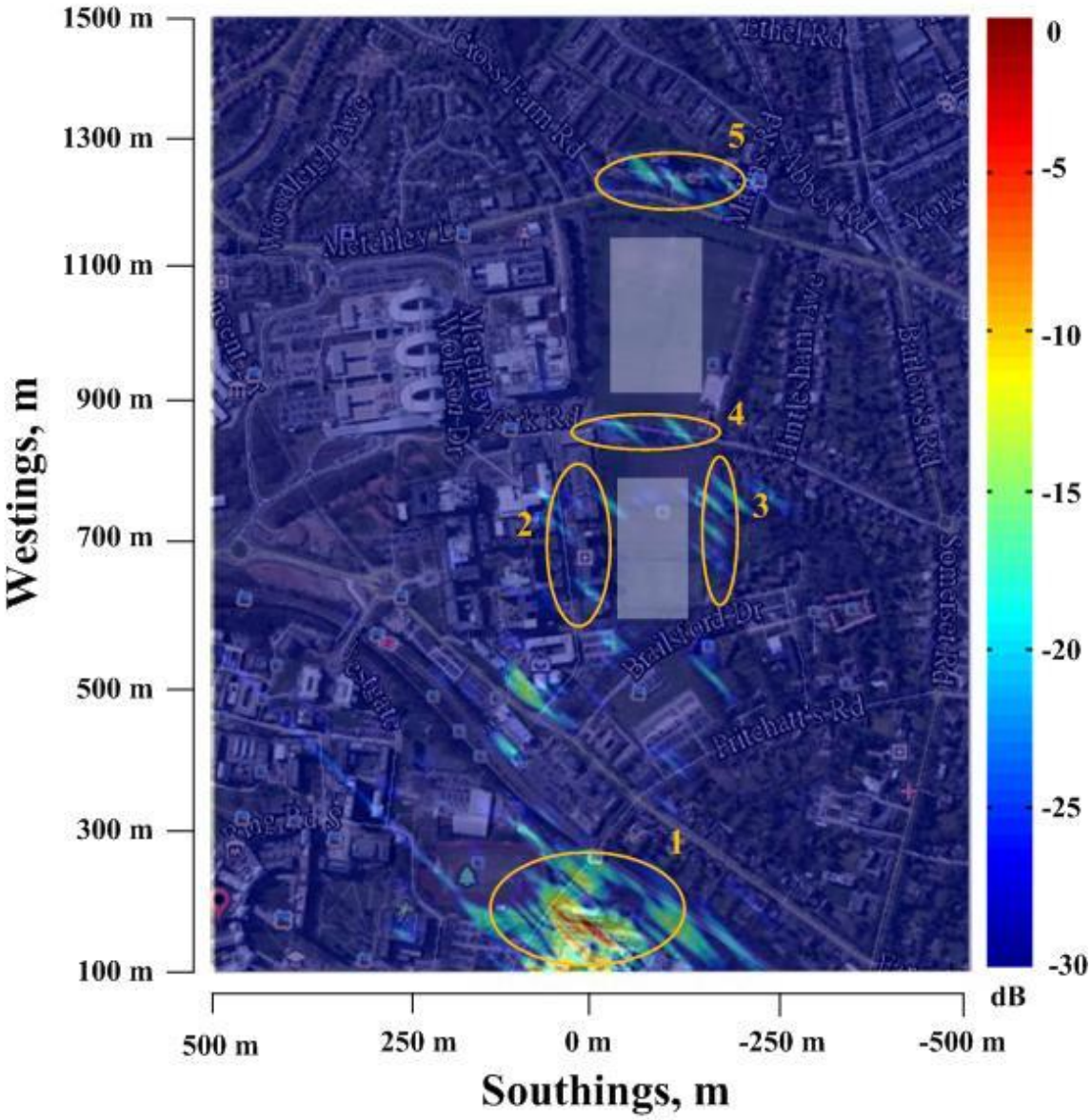

Figure 5.40: SS-BSAR image superimposed on satellite photograph of the same area

Inspection of this overlapped image arrives at some similar conclusions with Vale village site. For example, ground texture has successfully been classified, the Material school (marked with ellipsoid 1), Medical school (marked with ellipsoid 2), trees surrounding Metchley park (marked with ellipsoid 3 and 4) and four buildings (marked with ellipsoid 5) impose high reflectivity. while low signal intensity was observed in the grassy Metchley park (marked with shadowed rectangular). In

addition, the visibility of four buildings verified theoretical analysis (Fig. 5.33) and provides a promising future of such a configuration for ground-based large-size scene monitoring (up to 1250m far from receiver).

The reflectivity of the prominent features relative to measured at receiver and noise floor is listed in Table 5.14.

Features	Max magnitude measured relative to receiver (dB)	Max magnitude measured relative to noise floor (dB)
Material school (1)	-5.03	51.06
Medical school (2)	-29.62	26.47
Trees (3)	-32.81	23.28
Four buildings (4)	-31.73	24.36

Table 5.14: Target reflectivity parameters

Similar to analysis above, we come to look at image details. Fig. 5.41(a) shows the satellite optical photograph of Material school, and Fig. 5.41(b) is the once again optical photograph of the same area, but taken from location of receiver, Fig.5.41(c) shows the SAR image corresponding to the yellow dash rectangular area, superimposed on the satellite optical counterpart. Inspection of three images imposes multiple conclusions. Apart from coarse spatial resolution limited by the bandwidth of GLONASS ranging signal, the SAR image can be coarsely matched to the optical photograph in terms of signal intensity variation, i.e. all the signal intensity is enclosed in the middle part of Fig.5.41(c) (from -37m to 46m in South direction and from 70m to 200m in West direction). This is expected due to that, with regard to South direction, the area beyond +46m is almost occupied by roads, grass, etc., while that exceeding -37 are outside the beamwidth of receiver antenna. With regard to

West direction, all the objects are placed within 200m. Moreover, we found signal intensity of major parts on the roof area are weak, except two distinctive point-like image with high intensity, which are marked CR1 and CR2. It is not surprising that the satellite fires behind the receiver, after arriving at the flat roof area, most signals will reflect out. However, the white wall (CR2) and cabinet (CR2) shown in Fig. 5.41(b) can be served as corner reflectors. The signals from there are expected.

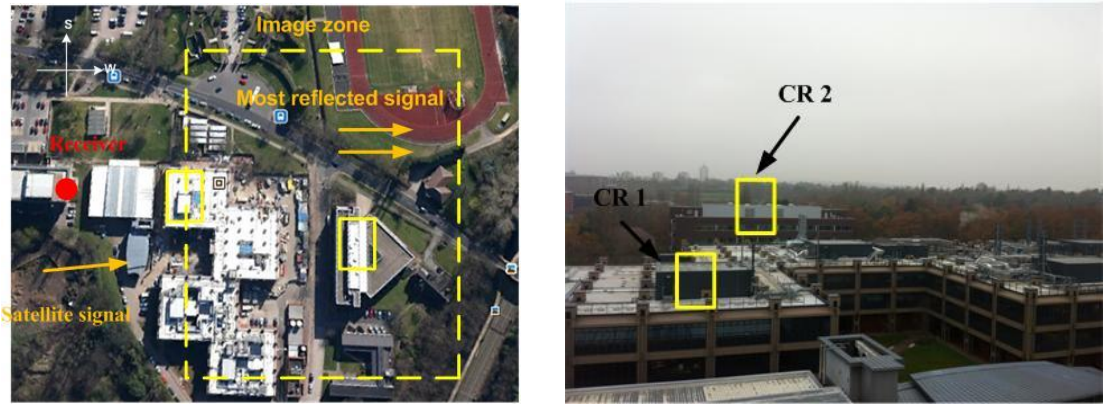

(a) (b)

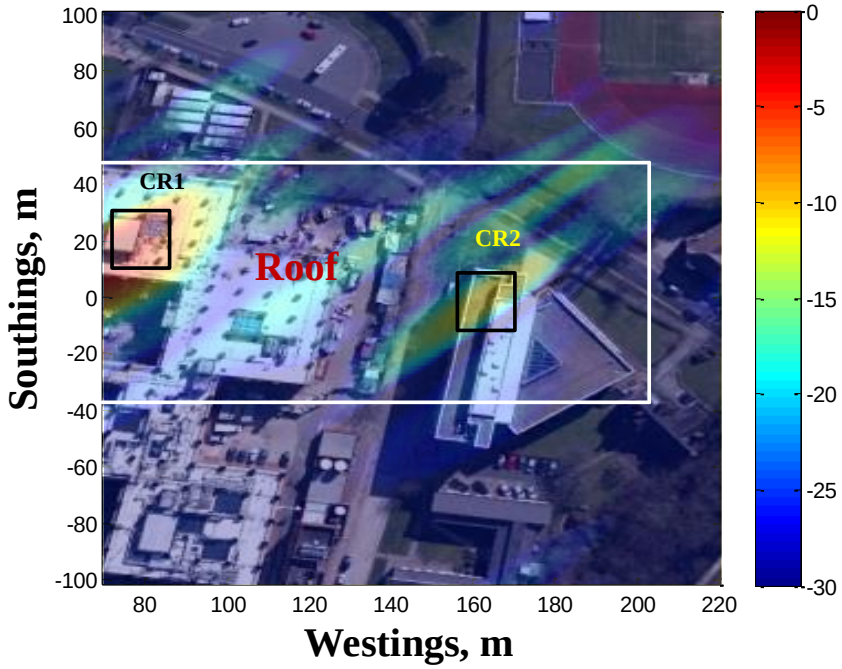

(c)

Figure 5.41: Image of Material school: (a) Optical satellite photograph, (b) Optical photograph taken from point of receiver, (c) SAR image superimposed on optical counterpart

Next we look into the zoomed image of four buildings at far end of target area (1250m) in Fig. 5.42. Fig. 5.42(a)) is a satellite photograph of this area from Google Earth software and Fig. 5.42(b) is the SAR image overlaid on the corresponding satellite photograph. The geometric distances between every neighbouring two buildings were measured (marked in Fig. 5.42(a)). It is clearly seen from Fig. 5.42(b) that the fours building are located at the correct positions. Though there are multiple responses corresponding to building 4, it may be due to multi-path effects and irregular shape of its roof.

(a) (b)

Figure 5.42: (a) Satellite photograph of four council buildings, (b) SAR image of council building superimposed on satellite photograph

Fig. 5.43(a) and (b) show the cross Sections of target 2 along West and South directions, and theoretical results are superimposed accordingly. Observation of Fig. 5.43 indicates that though experimental results are a little broadening than theoretical results (may caused by the building size), they may due to residual phase not fully compensated.

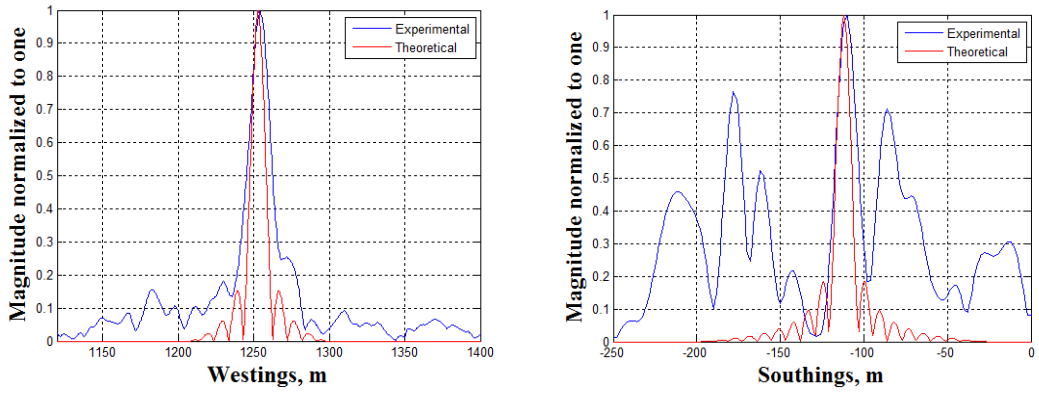

(a) (b)

Figure 5.43: Comparison between experimental and theoretical results, (a) Cross-Section along West direction, (b) Cross-Section along South direction

5.6 Conclusion

This paper presents our obtained experimental image results using SS-BSAR with GLONASS and a stationary receiver. Data collections were conducted in four different scenarios. In each program, experimental setup used for data acquisition was provided. The system performance such as power budget and potential resolution were given. HC signal synchronization outputs were provided. The obtained SS-BSAR images were analyzed to examine their correspondence of the real targeting area. Comparisons between experimental and theoretical cross sections of target responses along two dimensions were performed to verify expected theoretical resolution. Inspections of all the experimental results show that the obtained images are highly agreed with imaging scene and targets SNR align with theoretical expectations.

CHAPTER 6

CONCLUSIONS AND FUTURE WORK

6.1 Conclusions

In this thesis, a comprehensive research programme on GNSS based BSAR system with fixed receiver has been performed, including radar system performance, coordinate processing, signal synchronization between transmitter and receiver, image formation, experimentation, analysis of bistatic imagery and associated change detection applications.

The novelty of this work arises from such a particular bistatic configuration, where the passive mode, navigation satellite, navigation signal, asymmetric bistatic geometry are involved together. Moreover, the application by using such a passive mode is also noteworthy.

The major contribution of the research is the experimental demonstration of imagery capability of SS-BSAR with GNSS and stationary receiver, implying its feasibility of earth observation for its final use.

The GNSS transmitter and equipment used for data collection were introduced. It was justified that GLONASS is selected as optimal transmitter in terms of resolution and satellite number. The receiver architecture and two antennas were presented briefly. The experimental specifications such as resolution and power budget analysis have been given analytically and by simulation. It has been concluded theoretically that the bistatic resolution arrives at optimal if quasi-monostatic geometry is performed. In addition, the power budget of our system limited the maximum detected range, however, object at 1000m is still visible.

A new synchronization method between transmitter and receiver is derived and test to be applicable, aimed at dealing with computational complexity at long dwell time. It has been analytical and experimentally demonstrated that the new algorithm has parallel accuracy with those in literature, while took less time by 3 times. Even though the new algorithm was initially proposed for GLONASS signal tracking, it could be used for other GNSS type such as Galileo. The proposed algorithm may well be applicable when the Galileo is fully operational.

A modified BPA has been proposed to obtain the SS-BSAR image. The analytical expression of each step in the algorithm was derived. It has been demonstrated that the synchronization outputs were well integrated in the proposed algorithm from both simulation and experimental outcomes.

Experiments using GLONASS as transmitter and a ground-based receiver were conducted at four different scenarios. The topologies, synchronization were provided. The images were analyzed and compared with the corresponding optical photograph. It is found that our SS-BSAR images have one to one macthes with real scene in

terms of reflection. Moreover, the experimental resolutions have high accordance with theoretical expectations. This work suggested that SS-BSAR with GLONASS and a stationary receiver has the capability of small size imaging.

A feasibility research with regard to fixed receiver SS-BSAR as a change detector has been carried up. An experimental test bed was built to test system performance under controlled and ideal conditions, to evaluate the potential of such a technology. A signal processing chain consisting of signal synchronization, image formation and basic change detection algorithm was described. It can be found from experimental measurements that the phase stability and CCD accuracy are satisfactory enough to initiate the systematic study of the system on the feasibility level, which will be our future work.

6.2 Future work

A. Experimental image formation using frequency domain algorithm

Future work can involve an investigation of how to obtain the experimental image of SS-BSAR using frequency domain algorithm. To verify the imaging capability of such a system, the time domain algorithm, i.e. BPA was applied at first place. After obtaining image in this mode, it is suggested to develop frequency domain algorithm for SS-BSAR, aimed at improving processing efficiency. The difficulty embedded for such a task will be multiple. In the case of long dwell time, the transmitter moving path is no longer a straight line, therefore restraining the use of operation in frequency domain. Also, the spatial variation characteristics of our geometry make reference signal in two dimensions more complex.

B. Multi-perspective SS-BSAR with GNSS and stationary receiver

The imaging capability of SS-BSAR with GNSS and a stationary receiver has been experimentally proved in this thesis. The next task is to investigate the major advantage of the GNSS as the transmitters. The large number of satellites in a GNSS constellations offer a rather unique system diversity. The signal reflections from multiple satellites can be acquired by a single receiver, which can then generate multiple images of the same scene but from different viewpoints. These images can then be exploited and/or combined to increase information about a given scene, such as surface characterization, etc.

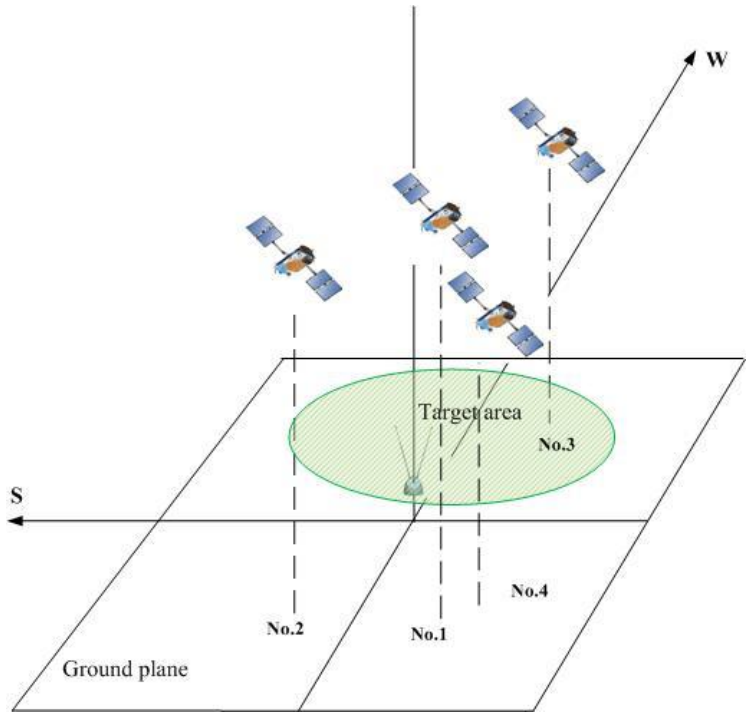

Figure 6.1: Satellite positions of experiments

A number of experiments were conducted at different satellite positions for the Metchley Park site (Fig. 5.37(a)). The aim is to enclose satellites positions at various azimuth angles and elevation angles, to analyze the corresponding response of different scene features. An illustration of an experimental program is shown in Fig. 6.1. The obtained corresponding SS-BSAR images are shown in Fig. 6.2.

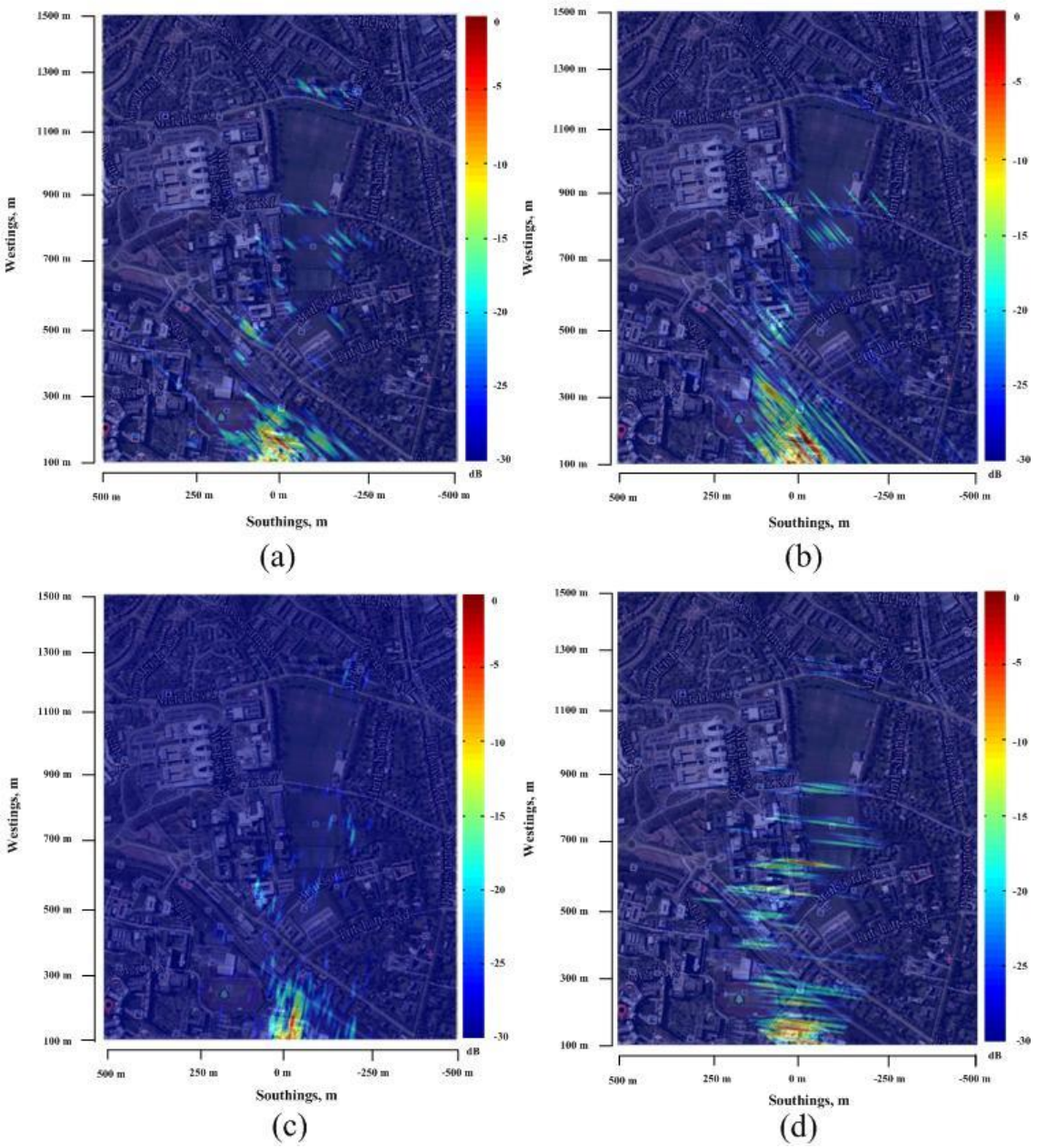

Figure 6.2: SS-BSAR image results of experiment (a) No.1, (b) No. 2, (c) No. 3, (d) No. 4

The future work lies in the investigation of the bistatic scattering properties of different objects within a scene, such as targets visibility of different features at different illumination angle and bistatic angle, bistatic scattering coefficient at different bistatic geometries, etc.

C. CCD feasibility study using SS-BSAR with GNSS and stationary receiver

The proof of concept of SS-BSAR with GNSS and stationary receiver has been verified experimentally [69]. The next step is its feasibility study, where the change detection of full-size targeting area will be involved.

The imaging scene will be Vale village site (Fig. 5.23(a)). The reason is that there is an isolated building, i.e. Vale village (Fig. 5.33(a)), making it as a reference point and easy to analyze. Three images acquired separating 3 seconds consecutively have been formed (Fig. 6.3). Observation of these images found no obvious difference, as expected due to trivial decorrelation.

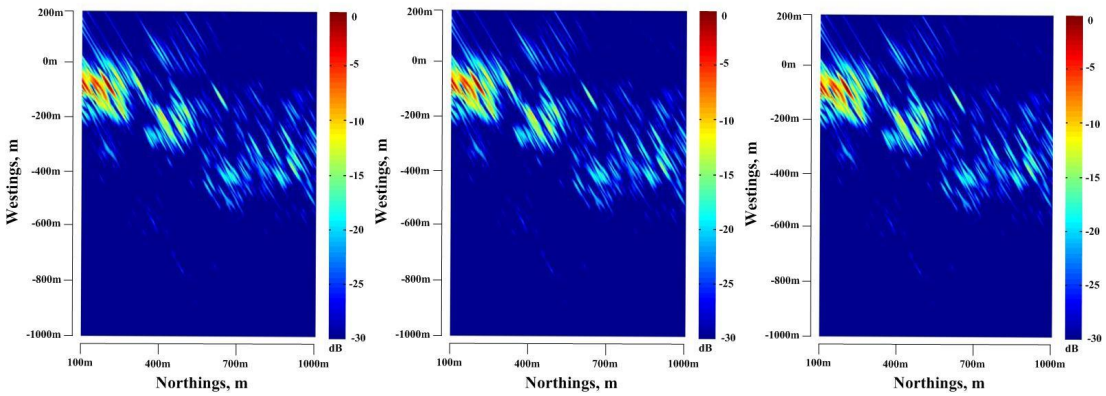

(a) (b) (c)

Figure 6.3: (a) SS-BSAR image 1, (b) SS-BSAR image 2, (c) SS-BSAR image 3

The coherence map of image 1 between image 2 and image 3 individually are shown in Fig. 6.4. In other words, Fig. 6.4(a) is the coherence map of two images separating 3 seconds and Fig. 6.4(b) 6 seconds.

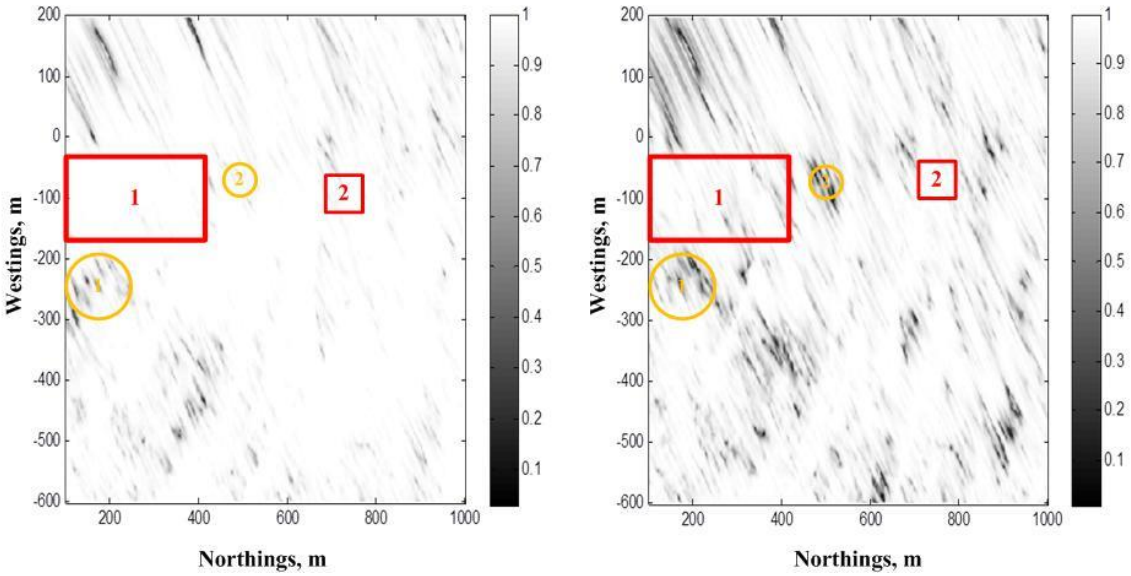

(a) (b)

***Figure 6.4**: Coherence map between (a) Image 1 and Image 2, (b) Image 1 and Image 3

** The coherence map was generated by Mr. Qilei Zhang, who was a visiting researcher from China*

Comparison of these two coherence maps apparently indicates that coherence deteriorate with acquisition interval, i.e. the larger the interval is, the worse the coherence will be. Moreover, the high intensity areas such as Horton grange (marked with red rectangular 1) and Vale village (marked with red rectangular 2) are highly correlated, while the low intensity grassy area (marked with yellow circle 1 and 2) is seriously coherent (correlation coefficient is down to 0.3 when 6 seconds acquisition interval is applied).

It is well understood that the generic de-correlation mainly consists of three components: temporal de-correlation, spatial de-correlation and thermal de-correlation [monostatic de-correlation paper]. In Fig. 6.4, it is quite difficult to measure or even qualify the de-correlation factors. We should only investigate one factor while keeping others fixed.

Therefore, the first stage for future work suggested here will be repeat-pass images obtained at multiple revisit cycle intervals. The minimum spatial de-correlation ensured by this way will make CCD more straightforward.

APPENDIX A

GLONASS L1 BAND FREQUENCY SCHEME

Satellite number	Code	RF Channel	Frequency (MHz)
1	730	1	1602.5625
2	728	-4	1599.75
3	727	5	1604.8125
6	733	6	1605.375
5	734	1	1602.5625
7	712	5	1604.8125
8	729	6	1605.375
14	722	-2	1600.875
10	717	-7	1598.0625
11	723	0	1602
13	721	-2	1600.875
14	715	-7	1598.0625
15	716	0	1602
17	718	4	1604.25
18	724	-3	1600.3125
19	720	3	1603.6875
20	719	2	1603.125
21	725	4	1604.25
22	731	-3	1600.3125
22	726		Maintenance

23	732	3	1603.6875
17	714		Spares
24	735	2	1603.125
12	737	-1	1601.4375
4	742	6	1605.375
2	743	-4	1599.75
3	744	5	1604.8125
7	745	5	1604.8125
17	746	4	1604.25
9	736	-2	1600.875

Table A.1: GLONASS frequency scheme

APPENDIX B

COORDINATE TRANSFORMATION

Let's define the position of object of interest in local coordinate frame (x, y, z), while in ECEF coordinate frame (x', y', z'). Helmert algorithm is applied to find the relationship between these two. It is also called 7-parameter algorithm due to 7 parameters are needed to perform the transformation [74]. The basic equation of Helmert algorithm is given by:

$$\begin{pmatrix} x \\ y \\ z \end{pmatrix}^r = \begin{pmatrix} \Delta x \\ \Delta y \\ \Delta z \end{pmatrix} + (1+s) \times Matrix_{rot} \times \begin{pmatrix} x' \\ y' \\ z' \end{pmatrix} \tag{B.1}$$

where $Matrix_{rot} =$

$$\begin{pmatrix} \cos(\alpha) & \sin(\alpha) & 0 \\ -\sin(\alpha) & \cos(\alpha) & 0 \\ 0 & 0 & 1 \end{pmatrix} \times \begin{pmatrix} 1 & 0 & 0 \\ 0) & \cos(\beta) & \sin(\beta) \\ 0 & -\sin(\beta) & \cos(\beta) \end{pmatrix} \times \begin{pmatrix} \cos(\gamma) & \sin(\gamma) & 0 \\ -\sin(\gamma) & \cos(\gamma) & 0 \\ 0 & 0 & 1 \end{pmatrix}$$

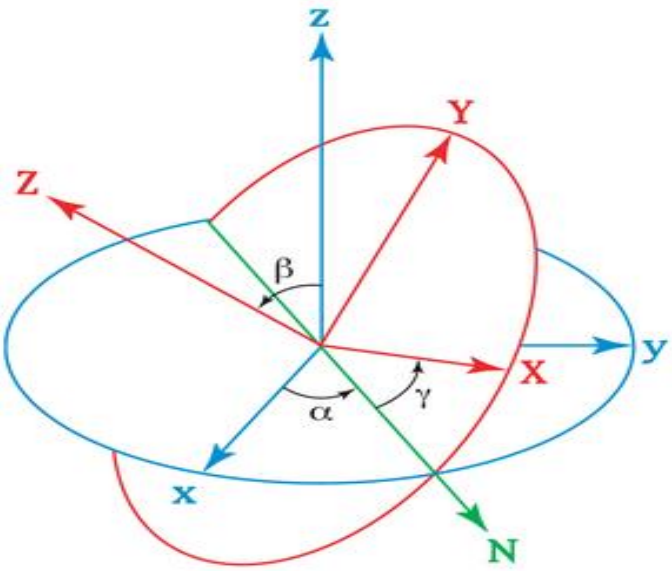

Figure B.1: Illustration of Helmert alogorithm [74]

The definitions of parameters could be better illustrated in Fig. B.1. Coordinate in blue colour and red colour represent old and new coordinate frames respectively. α is the angle between X axis of origin coordinate and line of North, β is the angle between Z axis of origin coordinate and that of new coordinate, γ is the angle of line of North and X axis of new coordinate. Δx, Δy and Δz are the distance between origin of new coordinate frame and old coordinate frame at x, y and z axis. s is scaling factor (1 is commonly used).

APPENDIX C

COORDINATE INTERPOLATION

C.1 Lagrange interpolation

Lagrange interpolation is a linear polynomial interpolation, given there is a Lagrange polynomial passing through *n+1* point sets

$$(x_0, y_0), (x_1, y_1), (x_2, y_2), \cdots, (x_n, y_n) \tag{C.1}$$

where $(x_i)_{0\leq i\leq n}$ is defined as points of interpolation and $(y_i)_{0\leq i\leq n}$is defined as values of interpolation. The Lagrange polynomial is given by:

$$\mathrm{y(x)} = \sum_{\mathrm{i=0}}^{\mathrm{n}} \mathrm{y_i} l_{\mathrm{i}} \tag{C.2}$$

where $l_i = \prod_{\substack{0\leq m\leq n \\ m\neq i}} \frac{x-x_m}{x_i-x_m} = \frac{(x-x_1)(x-x_2)\cdots\cdots(x-x_{i-1})(x-x_{i+1})\cdots\cdots(x-x_n)}{(x_i-x_1)(x_i-x_2)\cdots\cdots(x_i-x_{i-1})(x_i-x_{i+1})\cdots\cdots(x_i-x_n)}$

Hence, the polynomial evaluated at x_i could be obtained by following equation:

$$\begin{aligned}\mathrm{y_i} = {} & \frac{(x_i - x_2)(x_i - x_3)\cdot\cdots\cdot(x_i - x_n)}{(x_1 - x_2)(x_1 - x_3)\cdot\cdots\cdot(x_1 - x_n)} y_1 + \frac{(x_i - x_1)(x_i - x_3)\cdot\cdots\cdot(x_i - x_n)}{(x_2 - x_1)(x_2 - x_3)\cdot\cdots\cdot(x_2 - x_n)} y_2 \\ & + \cdots + \frac{(x_i - x_1)(x_i - x_2)\cdot\cdots\cdot(x_i - x_{n-2})(x_i - x_n)}{(x_{n-1} - x_1)(x_{n-1} - x_2)\cdot\cdots\cdot(x_{n-1} - x_{n-2})(x_{n-1} - x_n)} y_{n-1} \\ & + \frac{(x_i-x_1)(x_i-x_2)\cdots\cdots(x_i-x_{n-1})}{(x_n-x_1)(x_n-x_2)\cdots\cdots(x_n-x_{n-1})} y_n\end{aligned} \tag{C.3}$$

C.2 Power polynomial interpolation

Polynomial fitting is known as curve fitting. It is aimed at constructing a curve that has best fit to the know point data sets. Given a set of n+1 known different data points

$$(x_0, y_0), (x_1, y_1) \cdots, (x_n, y_n) \tag{C.4}$$

The value at x_i could be expressed as:

$$\mathrm{y_i} = \sum_{t=0}^{N} a_t {x_i}^t = a_0 + a_1 x_i + \cdots a_N {x_i}^{\mathrm{N}} \tag{C.5}$$

where N is the order of polynomial, when N equals to 1, the polynomial fitting following least mean square rule, which is the simplest form in this class. Using matrix form, Eq. could be written as

$$Y = XA \tag{C.6}$$

where

$$Y = \begin{bmatrix} y_0 \\ y_2 \\ \vdots \\ y_n \end{bmatrix}, \qquad X = \begin{bmatrix} 1 & x_0 & \ldots & {x_0}^N \\ 1 & x_1 & \ldots & {x_1}^N \\ \vdots & \vdots & & \vdots \\ 1 & x_n & \ldots & {x_n}^N \end{bmatrix}, \qquad A = \begin{bmatrix} a_0 \\ a_1 \\ \vdots \\ a_N \end{bmatrix}$$

Eq. (C.7) could be solved by applying least mean square rule, the solution is given by:

$$A = (X'X)^{-1}X'Y \tag{C.7}$$

Hence, Eq. (C.8) could be calculated by:

$$y_i = [1 \quad x_i \quad \cdots \quad {x_i}^N] \cdot A \tag{C.8}$$

APPENDIX D

GALILEO SIGNAL STRUCTURE

The Galileo satellite transmits signal at a number of frequency bands for different purpose (Fig. D.1).

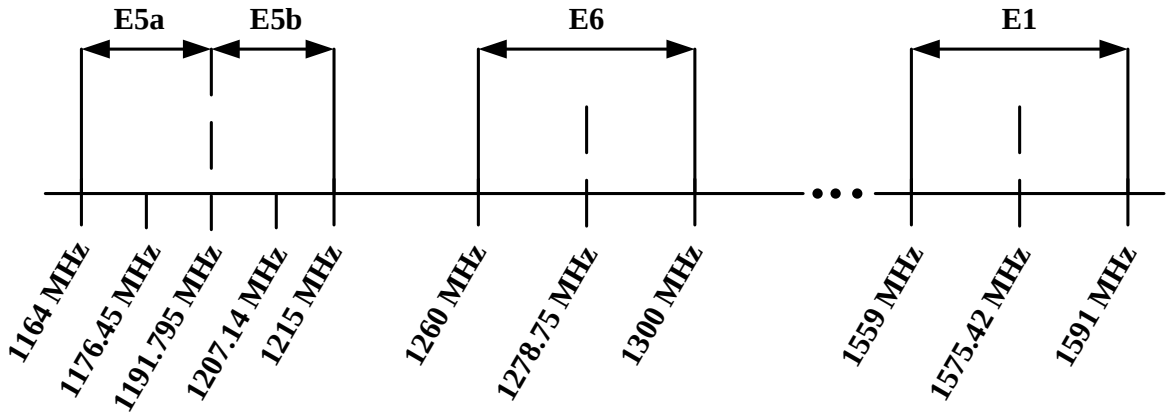

Figure D.1: Galileo signal frequency bands [74]

For radar imaging purposes, signals in the E5 band are preferable. That is because they are not encrypted, and have relatively wide bandwidths to provide a sufficient range resolution. The signal generation scheme for the E5 band is shown in Fig. D.2.

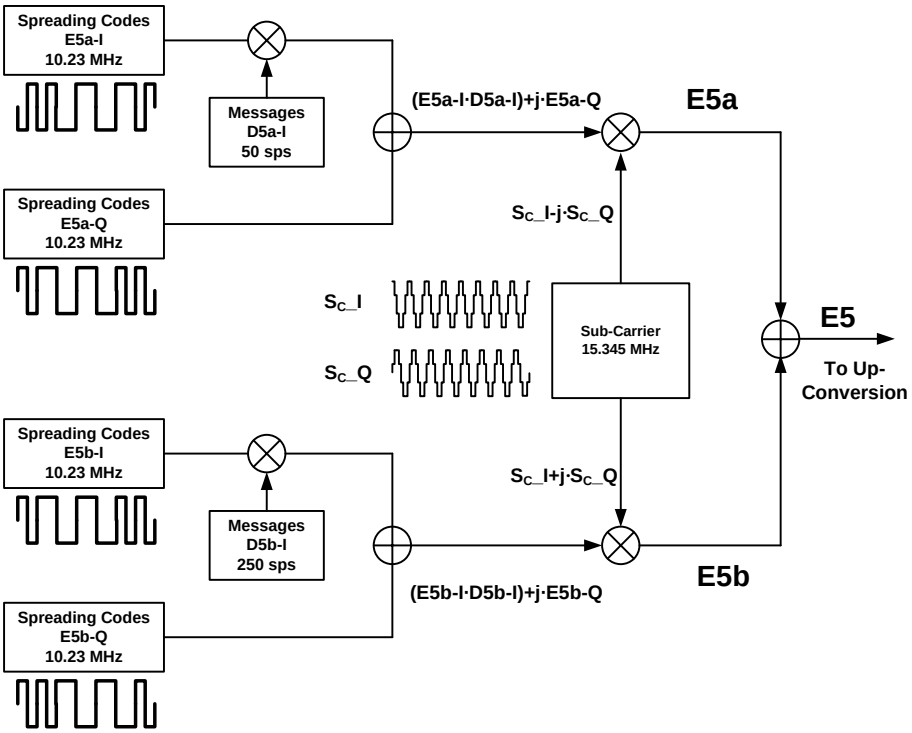

Figure D.2: Galileo E5 signal modulation scheme [74]

The composite E5 band contains two signals, E5a and E5b, centred at 1176.45 MHz and 1207.14 MHz, respectively. Both of these signals are generated using a dedicated modulation scheme called AltBOC, and have their own individual in-phase and quadrature components, $E5_{a-I/Q}$ and $E5_{b-I/Q}$, respectively. Each of these signals is composed of two spreading codes, called the primary and secondary codes. An XOR operation between these codes gives the corresponding quadrature signal. Both spreading codes are pseudo-random sequences, with chip durations of 100us (primary) and approximately 10ms (secondary). The bandwidth of the primary code is 10.23MHz. The I-components of both signals contain navigation data sampled at 50 ($E5_{a-I}$) and 250 ($E5_{b-I}$) symbols/s. The total E5 signal is the sum of the E5a and E5b signals. Prior to summation, the signals are modulated with a sub-carrier frequency. The mathematical expression for Galileo transmitted signal is given by [72].

$$s_{E5}(t) = \frac{1}{2\sqrt{2}}\left(s_{E5_{a-I}}(t) + js_{E5_{a-Q}}(t)\right)\left[sc_{E5-s} - jsc_{E5-s}\left(t - \frac{T_{s,E5}}{4}\right)\right]$$
$$+\frac{1}{2\sqrt{2}}\left(s_{E5_{b-I}}(t) + js_{E5_{b-Q}}(t)\right)\left[sc_{E5-s}(t) - jsc_{E5-s}\left(t - \frac{T_{s,E5}}{4}\right)\right]$$
$$+\frac{1}{2\sqrt{2}}\left(\bar{s}_{E5_{a-I}}(t) + j\bar{s}_{E5_{a-Q}}(t)\right)\left[sc_{E5-s}(t) - jsc_{E5-s}\left(t - \frac{T_{s,E5}}{4}\right)\right]$$
$$+\frac{1}{2\sqrt{2}}\left(\bar{s}_{E5_{a-I}}(t) + j\bar{s}_{E5_{a-Q}}(t)\right)\left[sc_{E5-s}(t) - jsc_{E5-s}\left(t - \frac{T_{s,E5}}{4}\right)\right] \quad \text{(D.1)}$$

where $s_{E5_{a-I}}$, $s_{E5_{a-Q}}$, $s_{E5_{b-I}}$ and $s_{E5_{b-Q}}$ are BPSK modulated ranging signal (including navigation message). $\bar{s}_{E5_{a-I}}$ $\bar{s}_{E5_{a-Q}}$, $\bar{s}_{E5_{b-I}}$ and $\bar{s}_{E5_{b-Q}}$ are the derivatives of$s_{E5_{a-I}}$, $s_{E5_{a-Q}}$, $s_{E5_{b-I}}$and $s_{E5_{b-Q}}$. sc_{E5-s} and sc_{E5-P} are subcarrier functions. $T_{s.E5}$ is the subcarrier sampling interval.

After I-Q demodulation (output from receiver), its baseband components can be written as

$$I(t_n, u) = s_{E5b-I}[t_n - \tau(u)] \cdot \cos(2\pi\Delta f_{E5b}[t_n - \tau(u)] + \theta_{E5b})$$
$$+s_{E5b-Q}[t_n - \tau(u)] \cdot \sin(2\pi\Delta f_{E5b}[t_n - \tau(u)] + \theta_{E5b}) \quad \text{(D.2)}$$

$$Q(t_n, u) = s_{E5b-I}[t_n - \tau(u)] \cdot \sin(2\pi\Delta f_{E5b}[t_n - \tau(u)] + \theta_{E5b})$$
$$-s_{E5b-Q}[t_n - \tau(u)] \cdot \cos(2\pi\Delta f_{E5b}[t_n - \tau(u)] + \theta_{E5b}) \quad \text{(D.3)}$$

Then the complex signal could be written as:

$$s(t_n, u) = I(t_n, u) + j \cdot Q(t_n, u)$$
$$= [s_{E5b-I}[t_n - \tau(u)] \cdot \cos(2\pi\Delta f_{E5b}[t_n - \tau(u)] + \theta_{E5b})$$
$$+s_{E5b-Q}[t_n - \tau(u)] \cdot \sin(2\pi\Delta f_{E5b}[t_n - \tau(u)] + \theta_{E5b})]$$
$$+j \cdot [s_{E5b-I}[t_n - \tau(u)] \cdot \sin(2\pi\Delta f_{E5b}[t_n - \tau(u)] + \theta_{E5b})$$
$$-s_{E5b-Q}[t_n - \tau(u)] \cdot \cos(2\pi\Delta f_{E5b}[t_n - \tau(u)] + \theta_{E5b})]$$

$$= [s_{E5b-I}[t_n - \tau(u)] \cdot \cos(2\pi\Delta f_{E5b}[t_n - \tau(u)] + \theta_{E5b}) + j \cdot s_{E5b-I}[t_n - \tau(u)]$$
$$\cdot \sin(2\pi\Delta f_{E5b}[t_n - \tau(u)] + \theta_{E5b})]$$
$$+[s_{E5b-Q}[t_n - \tau(u)] \cdot \sin(2\pi\Delta f_{E5b}[t_n - \tau(u)] + \theta_{E5b}) - j \cdot s_{E5b-Q}[t_n - \tau(u)]$$
$$\cdot \cos(2\pi\Delta f_{E5b}[t_n - \tau(u)] + \theta_{E5b})]$$
$$= s_{E5b-I}[t_n - \tau(u)] \cdot [\cos(2\pi\Delta f_{E5b}[t_n - \tau(u)] + \theta_{E5b}) + j$$
$$\cdot sin(2\pi\Delta f_{E5b}[t_n - \tau(u)] + \theta_{E5b})]$$
$$+s_{E5b-Q}[t_n - \tau(u)] \cdot [sin(2\pi\Delta f_{E5b}[t_n - \tau(u)] + \theta_{E5b}) - j$$
$$\cdot \cos(2\pi\Delta f_{E5b}[t_n - \tau(u)] + \theta_{E5b})]$$
$$= s_{E5b-I}[t_n - \tau(u)] \cdot [e^{(j(2\pi\Delta f_{E5b}[t_n - \tau(u)] + \theta_{E5b}))} - j \cdot s_{E5b-Q}[t_n - \tau(u)]$$
$$\cdot e^{(j(2\pi\Delta f_{E5b}[t_n - \tau(u)] + \theta_{E5b}))}] \quad \text{(D.4)}$$

Therefore, received signal in Q channels could be rewritten as:

$$Q(t_n, u) = -s_{E5b-Q}[t_n - \tau(u)] \cdot e^{(j(2\pi\Delta f_{E5b}[t_n - \tau(u)] + \theta_{E5b}))} \quad \text{(D.5)}$$

APPENDIX E

PUBLICATIONS LIST

1. Zeng Z., Antoniou M., Liu F., Cherniakov M., "First Space-Surface Bistatic Fixed Receiver SAR Images with A Navigation Satellite," *Presented on International Radar Symposium,* Germany, 2011

2. Zeng Z., Antoniou M., Zhang Q., Ma H., Cherniakov M., "Multi-Perspective GNSS Based BSAR: Preliminary Experimental Results," *International Radar Symposium, Germany,* 2013. (abstract accepted).

3. Zeng Z., "SS-BSAR with GNSS and A Stationary Receiver – Experimental Results," *Progress in Electromagnetic Research B,* vol. *48,* pp. *271-287*, 2013

4. Antoniou M., Zeng Z., Liu F., Cherniakov M., "Experimental Demonstration of Passive BSAR Imaging Using Navigation Satellites and A Fixed Receiver," *Geoscience and Remote Sensing Letters,* vol. *99,* pp. *1-5*, 2011

5. Antoniou M., Zeng, Z., Liu F., Cherniakov M., "Passive Radar Imaging with GNSS Transmitters and A Fixed Receiver: Latest Results," *Presented on EUSAR Conference*, Germany, 2012

6. Antoniou M., Liu F., Zeng Z., Sizov V., Cherniakov M., "Coherent Change Detection Using GNSS-Based Passive SAR: First Experimental Results," *presented on IET Radar Conference*, UK, 2012

7. Liu F., Antoniou M., Zeng Z., Cherniakov M., "Point Spread Function Analysis of Long Integration Time BISAR Systems with GNSS Satellite as Transmitter and A Fixed Receiver," *Geoscience and Remote Sensing Letters, 2013*. (electronic version accessible)

8. Liu F., Antoniou M., Zeng Z., Cherniakov M., "Coherent Change Detection Using Passive GNSS-based BSAR: Experimental Proof of Concept," *IEEE Transactions on Geoscience and Remote Sensing, 2013.* (electronic version accessible)

9. Zhou H., Antoniou M., Zeng Z., etc., "Pre-processing for Time Domain Image Formation in SS-BSAR system," *Journal of Systems Engineering and Electronics*. Vol. *23*, pp. *875-880*, 2012

10. Antoniou M., Zhou H., Zeng Z., etc., "Passive BSAR Imaging with Galileo transmitters and A Moving Receiver: Experimental Demonstration," *IET Radar, Sonar & Navigation*., 2013 (revision submitted)

References

[1] Antoniou M., "*Image formation algorithms for space-surface bistatic SAR*", Ph.D Thesis, University of Birmingham, 2007.

[2] Willis N. J., Griffiths D. H., "*Advances in bistatic radar*," SciTech Publishing, Inc, 2007

[3] Carrara G, W, etc, "*Spotlight synthetic aperture radar signal processing algorithms*," Artech house.

[4] Ender J. H. G., Walterscheid I., Brenner A. R., "New aspects of bistatic SAR: processing and experiments," *IGARSS*, vol. *3*, pp. *1758-1762*, 2004

[5] D.R. Sheen, N. P. Malinas, etc., "Foliage transmission measurements using a ground based ultrawide band (300-1300 MHz) SAR system," *IEEE Transactions on Geoscience and Remote Sensing*, vol. *32*, 1994.

[6] Nashashibi, A. Y., Ulaby, F. T., "Bistatic SAR imaging: a novel approach using a stationary receiver," *IGARSS*, pp. *125-128*, 2007

[7] Soumekh M., "Moving target detection in foliage using along track monopulse synthetic aperture radar imaging," *IEEE Transactions on Image Processing*, vol. *6*, 1997

[8] Cantalloube H., Wendler M., ect., "A first bistatic airborne SAR interferometry experiment – preliminary results," *Sensor Array and Multichannel signal processing workshop proceedings*, pp. *667-671*, 2004

[9] Yates G., et. al., "Bistatic SAR imge formation", Radar, Sonar and Navigation, IEE Proceedings, vol. 153, pp. 208-213, 2006

[10] Dubois-Fernandez P., Cantaloube H., Vaizan B., etc., "ONERA-DLR bistatic SAR campaign: planning, data acquisition, and first analysis of bistatic

scattering behaviour of natural and urban targets," *IEE Proceedings Radar, Sonar and Navigation*, vol. *153*, pp. *214-223*, 2006

[11] Walterscheid I., Joachim H. G. Ender, etc., "Bistatic SAR processing and experiments," *IEEE Transactions on Geoscience and Remote Sens*ing, vol. *44*, 2006.

[12] Ulandar Lars M. H., Flood Bjoern, Froelind Per-Olov, etc., "Bistatic experiment with ultra-wideband VHF-band synthetic-aperture radar," *EUSAR*, pp. *1-4*, 2008

[13] Henke D., Barmettler A., Meier E., "Bistatic experiment with the UWB-CARABAS sensor – first results and prospects of future applications," *IGARSS*, vol. *2*, pp. *234-237*, 2009

[14] Balke J., "Field test of bistatic forward-looking synthetic aperture radar," *IEEE Radar conference*, pp. *424-429*, 2005

[15] Balke J., "SAR image formation for forward-looking radar receivers in bistatic geometry by airborne illumination," *IEEE Radar Conference*, pp. *1-5*, 2008

[16] Baque R., Dreuillet P., du Plessis O. R., etc., "LORAMbis a bistatic VHF/UHF SAR experiment for FOPEN," *IEEE Radar Conference*, pp. *832-837*, 2010

[17] Goh A. S., Preiss M., Stacy N., Gray D. A., "The Ingara bistatic SAR upgrade: first results," *International Conference on Radar*, pp. *329-334*, 2008

[18] Cazzani, L., Colesanti, C., etc., "A ground-based parasitic SAR experiment," *IEEE Transactions on Geoscience and Remote Sensing*, vol. *38*, pp. *2132-2141*, 2000.

[19] Sanz-Marcos J., Mallorqui J.J., Aguasca, A., Prats P., "First ENVISAT and ERS-2 parasitic bistatic fixed receiver SAR images processed with the subaperture range-Doppler algorithm," *IGARSS*, pp. *1840-1843*, 2006

[20] Lopez-Dekker P., Merlano J. C., Dugue S., Sanz-Marcos J., etc., "Bistatic SAR interferometry using ENVISAT and a ground based receiver: experimental results," *IGARSS*, pp. *107-110*, 2007

[21] Duque S., Lopez-Dekker P., Mallorqui J. J., "Single-pass bistatic SAR Interferometry using fixed-receiver configurations: theory and experimental validation," *IEEE Transactions on Geoscience and Remote Sensing*, vol. *48*, pp. *2740-2749*, 2010

[22] Sanz-Marcos J., Lopez-Dekker P., Mallorqui J.J., etc., "SABRINA: a SAR bistatic receiver for interferometric applications," *IEEE Geoscience and Remote Sensing Letters*, vol. *4*, pp. *307-311*,2007

[23] Lopez-Dekker Paco, Duque Sergi, Merlano, etc., "Fixed receiver bistatic SAR along-track interferometry: first result," *EUSAR*, pp. *1-4*, 2010

[24] Broquetas A., Fortes M., Siddique M.A., Duque S., etc., "Bistatic SAR based on TerraSAR-X and ground based receivers," *IGARSS*, pp. *114-117*, 2010

[25] Broquetas A., Lopez-Dekker P., Mallorqui J. J., ect., "SABRINA-X: bistatic SAR receiver for TerraSAR-X," *EUSAR*, pp. *1-3*, 2010

[26] Whitewood A.P., Baker C.J., Griffiths H.D., "Bistatic radar using a spaceborne illuminator," *IET International Conference on Radar systems*, pp. *1-5*, 2007

[27] Lindfen T., Akos D. M., "A multistatic GNSS synthetic aperture radar for surface characterization," *IEEE Transactions on Geoscience and Remote Sensing*, vol. *46*, pp. *2249-2253*, 2008

[28] Reuter S., Behner F., Nies H., Loffeld O., Matthes D., Schiller J., "Development and experiments of a passive SAR receiver system in a bistatic spaceborne/stationary configuration," *IGARSS*, pp. *118-121*, 2010.

[29] Wang Rui, Li Feng, Zeng Tao, "Bistatic SAR experiment, processing and results in spaceborne/stationary configuration," *IEEE CIE International Conference on Radar*, vol. *1*, pp. *393-397*, 2011

[30] Guttrich, G.L, Sievers, W. E., "Wide area surveillance concepts based on geosynchronous illumination and bistatic UAV or satellite reception," *IEEE Proceedings Aerospace Conference*, vol. *2*, pp. *171-180*, 1997

[31] Espeter T., Walterscheid I., Klare J., etc., "Progress of hybrid bistatic SAR: synchronization experiments and first imaging results," *EUSAR*, pp. *1-4*, 2008

[32] Walterscheid I., Espeter T., Gierull C., Klare J., "Results and analysis of hybrid bistatic SAR experiments with spaceborne, airborne and stationary sensors," *IGARSS*, vol. *2*, pp. *238-241*, 2009

[33] Walterscheid I., Espeter T., Brenner A. R., Klare J., Ender J. H. G, Nies H., ect., "Bistatic SAR experiments with PAMIR and TerraSAR-X – setup, processing, and image results," *IEEE Transactions on Geoscience and Remote Sensing*, vol. *48*, pp. *3268-3279*, 2010

[34] Rodriquez-Cassola M., Baumgartner S.V., Krieger G., etc., "Bistatic spaceborne-ariborne experiment TerraSAR-X/F-SAR: data processing and results," *IGARSS*, vol. *3*, pp. *451-454*, 2008

[35] Rodriguez-Cassola M., Baumgartner S. V., Krieger G., Moreira A., "Bistatic TerraSAR-X/F-SAR spaceborne-airborne SAR experiment: description, data processing, and results," *IEEE Transactions on Geoscience and Remote Sensing*, vol. *48*, 2010.

[36] Walterscheid I., Espeter T., Klare J., Brenner A., "Bistatic spaceborne-airborne forward-looking SAR," *EUSAR*, pp. *1-4*, 2010.

[37] Espeter T., Walterscheid I., Klare J., "Bistatic forward-looking SAR: results of a spaceborne-airborne experiment," *IEEE Geoscience and Remote Sensing Letters*, vol. *8*, pp. *765-768*, 2011.

[38] Fujimura T., Totsuka H., Imai N., etc.,"The bistatic SAR experiment with ALOS/PALSAR and Pi-SAR-L," *IGARSS*, pp. *4221-4224*, 2011.

[39] Prati C., Rocca F., etc., "Passive Geosynchronous SAR system reusing backscattered digital audio broadcasting signals," *IEEE Transactions on Geoscience and Remote Sensing*, vol. *36*, 1998.

[40] Mittermayer J., Krieger G., Moreira A., etc., "Interferometric performance estimation for the interferometric cartwheel in communication with a transmitting SAR-satellite," *IGARSS*, vol. *7*, pp. *2955-2957*, 2001

[41] Lee P.F, James K., "The RADARSAT-2/3 topographic mission," *IGARSS*, vol. *1*, pp. *499-501*, 2001

[42] Girard R., Lee P. F., James K., "The RADARSAT-2&3 topographic mission: an overview," *IGARSS*, vol. *3*, pp. *1477-1479*, 2002.

[43] D'Errico M., Moccia A., "The BISSAT mission: a bistatic SAR operating in formation with COSMO/SkyMed X-band radar," *IEEE Aerospace Conference Proceedings*, vol. *2*, pp. *809-818*, 2002

[44] Krieger G., Fiedler H., et. al, "TanDEM-X: a satellite formation for high-resolution SAR interferometry," *IET International Conference on Radar Systems*, pp. *1-5*, 2007

[45] Krieger G., Hajnsek I., Papathanassiou K. P., Younis M., Moreira A.,"Inteferometric synthetic aperture radar missions employing formation flying," *Proceedings of the IEEE*, vol. *98*, pp. *816-843*, 2010

[46] Rodriguez-cassola M., Prats P., etc., "First bistatic spaceborne SAR experiments with TanDEM-X," *IGARSS*, pp. *1393-1396*, 2011

[47] Rodriguez-cassola M., Prats P., etc., "First bistatic spaceborne SAR experiments with TanDEM-X," *IEEE Geoscience and Remote Sensing Letters*, vol. *9*, pp. *1-5*, 2012

[48] Cherniakov M., Zeng T., Plakidis E., "Ambiguity function for bistatic SAR and its application in SS-BSAR performance analysis," *Proceedings of the international radar conference*, pp. *343-348*, 2003

[49] Zeng T., Cherniakov M., Long T., "Generalized approach to resolution analysis in BSAR," *IEEE Transactions on Aerospace and Electronic Systems*, vol. *41*, pp. *461-474*, 2005

[50] He X., Zeng T., Cherniakov M., "Interference level evaluation in SS-BSAR with GNSS non-cooperative transmitter," *Electronics letters*, vol. *40*, pp. *1222-1224*, 2004

[51] He X., Zeng T., Cherniakov M., "Signal detectability in SS-BSAR with GNSS non-cooperative transmitter," *IEE Proceedings Radar, Sonar and Navigation*, vol. *152*, pp. *124-132*, 2005

[52] Cherniakov M, Zeng T., Plakidis E., "Galileo signal-based bistatic system for avalanche prediction," *IGARSS*, vol. *2*, pp. *784-786*, 2003

[53] Antoniou M., Cherniakov M., Zeng T., "Problems of surface change detection based on SS-InBSAR," *IEEE International Radar Conference*, pp. *791-795*, 2005

[54] Anoniou M., Cherniakov M., Saini R., Edwards J., Zuo R., "Modified range-doppler algorithm for space-surface BSAR imaging," *CIE International Conference on Radar*, pp. *1-4*, 2006

[55] Antoniou M., Saini R., Zuo R., Cherniakov M., "Image formation algorithm for space-surface BSAR," *European Radar Conference*, pp. *413-416*, 2007

[56] Antoniou M., Saini R., Cherniakov M., "Results of a space-surface bistatic SAR image formation algorithm," *IEEE Transactions on Geoscience and Remote Sensing*, vol. *45*, pp. *3359-3371*, 2007

[57] Antoniou M., Saini R., Zuo R., Cherniakov M., "Space-surface bistatic SAR topology and its impact on image formation," *EUSAR*, pp. *1-4*, 2008

[58] Antoniou M., Cherniakov M., Hu C., "Space-surface bistatic SAR image formation algorithms," *IEEE Transactions on Geoscience and Remote Sensing*, vol. *47*, pp. *1827-1843*, 2009

[59] Saini R., Zuo R., Cherniakov M., "Signal synchronization in SS-BSAR based on GLONASS satellite emission," *IET International conference on Radar Systems*, pp. *1-5*, 2007

[60] Saini R., Zuo R., Cherniakov M., "Problem of signal synchronization in space-surface bistatic synthetic aperture radar based on global navigation satellite emissions-experimental results," *IET Radar, Sonar & Navigation*, vol. *4*, pp. *110-125*, 2010

[61] Cherniakov M., Saini R., Zuo R., Antoniou M., "Space-surface bistatic synthetic aperture radar with global navigation satellite system transmitter of opportunity-experimental results," *IET Radar, Sonar & Navigation*, vol. *1*, pp. *447-458*, 2007

[62] Saini R., Zuo R., Cherniakov M., "Development of space-surface bistatic synthetic aperture radar with GNSS transmitter of opportunity," *IEEE Radar conference*, pp. *1-6*, 2008

[63] Cherniakov M., Pladikis E., Antiniou M., Zuo R., "Passive space-surface bistatic SAR for local area monitoring: primary feasibility study," *European Radar Conference*, pp. *89-92*, 2009

[64] Liu F., Antoniou M., Zeng Z., Cherniakov M., "Point spread function analysis for BSAR with GNSS transmitters and long dwell times: theory and experimental confirmation," *Geoscience and Remote Sensing Letters*, vol. *PP*, pp. *1-5*, 2012

[65] Antoniou M., Zeng Z., Liu F., Cherniakov M., "Passive radar imaging with GNSS transmitters and a fixed receiver: latest results", *EUSAR conference*, pp. *271-274*, 2012

[66] Zeng Z., Antoniou M., Liu F., Cherniakov M., "First space surface bistatic fixed receiver SAR images with a navigation satellite", *International Radar Symposium*, pp. *373-378*, 2011

[67] Antoniou M., Zeng Z., Liu F., Cherniakov M., "Experimental demonstration of passive BSAR imaging using navigation satellites and a fixed receiver", *IEEE Geo-science and Remote Sensing Letters*, vol. *99*, pp. *1-5*, 2011.

[68] Antoniou M., Liu F., Zeng Z., Cherniakov M., "Coherent change detection using GNSS-based passive SAR: first experimental results", Presented on *IET conference on radar system*, 2012

[69] Liu F., Antoniou M., Zeng Z., Cherniakov M., "Coherent change detection using passive GNSS-based BSAR: experimental proof" of concept", *IEEE Transactions on Geoscience and Remote Sensings*, vol. *PP*, pp. *1-12*, 2013

[70] GPS Interface Control Document, 2012

[71] GLONASS Interface Control Document 2012

[72] Galileo Interface Control Document 2012

[73] Beidou Interface Control Document 2012

[74] Zuo R., "*Bistatic synthetic aperture radar using GNSS as transmitters of opportunity*," PhD thesis, 2012.

[75] Soumekh M., "*Synthetic aperture radar signal processing with MATLAB algorithms*," Wiley, 1999

[76] Lei L., Zhou Y., Li J., Sun B., "Synchronization of GEO spaceborne-airborne bistatic SAR ," *IEEE International Geoscience and Remote Sensing Symposium (IGARSS)*, pp. *1209-1211*, 2008

[77] Sun C., Zhou L., Zhang D., Lu G., Chen W., "Analysis of phase synchronization errors based on distributed small satellite SAR system," *International Symposium on Antennas, Propagation & EM Theory (ISAPE)*, pp. *1-4*, 2006

[78] Liu R., Xiong J., Huang Y., "Analysis of bistatic SAR frequency synchronization," *International Conference on Communications, Circuits and System Proceedings*, vol. *1*, pp. *380-383*, 2006

[79] Zhang X., Li H., Wang J., "The analysis of time synchronization error in bistatic SAR system" *International Geoscience and Remote Sensing Symposium Proceedings*, pp. *4619-4622*, 2005

[80] Thompson C., "Bistatic radar noncooperative illuminator synchronization techniques," *IEEE Radar Conference*, pp. *29-34*, 1989

[81] Lei K., Wang X., Gong M., "Time and frequency synchronization analysis of airborne bistatic synthetic aperture radar," *Asia-Pacific Microwave Conference (AMPC)*, pp. *1-4,* 2007

[82] Li Z., Zeng D., Long T., Wang W., Hu C., "Analysis of time synchronization errors in bistatic SAR" *International Conference on Radar*, pp. *407-411,* 2008

[83] Krieger G., Younis M., "Impact of oscillator noise in bistatic and multistatic SAR", *IEEE Geoscience and Remote Sensing Letter*, vol. *3*, pp. *424-428,* 2006

[84] Gong X., Xu G., "Internal time and phase synchronization for distributed micro-satellite SAR," *International Conference on Radar*, pp. *1-4,* 2006

[85] Tian W., Liu H., Zeng T., "Frequency and time synchronization error analysis based on generalized signal model for bistatic SAR," *IET International Radar Conference,* pp. *1-4,* 2009

[86] Tian W., Hu S., Zeng T., "A frequency synchronization scheme based on PLL for BiSAR and experiment result," *International Conference on Signal Processing (ICSP)*, pp. *2425-2428,* 2008

[87] Wang W., "GPS-based time & phase synchronization processing for distributed SAR", *IEEE Transactions on Aerospace and Electronic Systems*, vol. *45*, pp. *1040-1051*, 2009

[88] Wang W., "Design of frequency synthesizer for synchronizing airborne bistatic SAR systems," *IEEE Aerospace Conference*, pp. *1-10*, 2008

[89] Wang W., Peng Q., Cai J., "Phase synchronization errors on near-space passive bistatic radar imaging", *IET International Radar Conference*, pp. *1-4*, 2009

[90] Lopez-Dekker P., Mallorgui J. J., Serra-Morales P., Sanz-marcos J., "Phase synchronization and Doppler centroid estimation in fixed receiver bistatic

SAR systems", *IEEE Transactions on Geoscience and Remote Sensing*, vol. *46*, pp. *3459-3471*, 2008

[91] Duque S., Lopez-Dekker P., Mallorgui J. J., "Single-pass bistatic SAR interferometry using fixed-receiver configurations: theory and experimental validation", *IEEE Transactions on Geoscience and Remote Sensing*, vol. *48*, pp. *2470-2749*, 2010

[92] Sanz-Marcos J., etc., "SABRINA – a SAR bistatic receiver for interferometric applications", *IEEE Geoscience and Remote Sensing Letters*, vol. *4*, pp. *307-311*, 2007,

[93] Tsui J., "*Digital techniques for wideband receivers*," Artech House, 1995

[94] Elliott D. Kaplan, "*Understanding GPS: principles and applications*", Artech House Publishers, 1996

[95] Nel Samama, "*Global positioning:technologies and performance,*" Wiley, 2007

[96] Tsui J., "*Fundamentals of global postioning system receivers*," Wiley & Sons, 2005

[97] IGS official website: http://www.igs.org/

[98] GPS calendar website: http://www.ngs.noaa.gov/CORS/Gpscal.shtmal

[99] IGS sp3 form: http://igscb.jpl.nasa.gov/igscb/data/format/sp3-docu.txt

[100] Skolnik M., "*Radar Handbook*," Second edition, Mc GrawHill, 1990

[101] http://ursi-test.intec.ugent.be/files/URSIGA08/papers/GP205p17.pdf

[102] Neo Y. L., "*Digital processing algorithms for bistatic synthetic aperture radar data,*" Ph.D thesis, 2007

[103] Aria D., Guarnieri A. M., Rocca F., "Focusing bistatic synthetic aperture radar using dip move out," *IEEE Transactions on Geoscience and Remote Sensing*, vol. *42*, pp. *1362-1372*, 2004

[104] Geng X., Yan H., Wang Y., "A-two-dimensional spectrum model for general bistatic SAR," *IEEE Transctions on Geoscience and Remote Sensing*, vol. *48*, pp. *2216-2223*, 2008

[105] Loffeld O., Nies H., Peters V., "Models and useful relations for bistatic SAR processing," *IEEE Transactions on Geoscience and Remote Sensing*, vol. *42*, pp. *2031-2038*, 2004

[106] Neo Y. L., Wong F., Cumming I. G., "A two-dimensional spectrum of bistatic SAR processing using series reversion," *IEEE Transactions on Geoscience and Remote Sensing*, vol. *4*, pp. *93-96*, 2007

[107] Ender J. H. G., Walterscheid I., Brenner A. R., "New aspects of bistatic SAR: processing and experiments," *Proceedings of International Geoscience and Remote Sensing Symposium*, vol. *3*, pp. *1758-1726*, 2004

[108] Hua Z., Liu X., "A fourth-order imaging algorithm for spaceborne bistatic SAR," *Proceedings on International Geoscience and Remote Sensing Symposium (IGARSS)*, 2006.

[109] Natroshvili K., Loffeld O., Nies H.,, "Focusing of general bistatic SAR configuration data with 2-D inverse scaled FFT," *IEEE Transactions on Geoscience and Remote Sensing*, vol. *44*, pp. *2718-2727*, 2006

[110] Neo Y. L., Wong F., Cumming I. G., "Processing of azimuth-invariant bistatic SAR data using the range Doppler algorithm," *IEEE Transactions on Geoscience and Remote Sensing*, vol. *46*, pp. *14-21*, 2008

[111] Neo Y. L., Wong F., Cumming I. G., "A comparison of a point target spectra derived for bistatic SAR processing," *IEEE Transactions on Geoscience and Remote Sensing*, vol. *46*, pp. *2481-2492*, 2008

[112] Bamler R., Boerner E., "On the use of numerically computed transfer function for processing of data from bistatic SARs and high squint orbital SARs," *Proceedings of International Geoscience and Remote Sensing Symposium (IGARSS)*, vol. *2*, pp. *1051-1055*, 2005.

[113] Bamler R., Meyer F., Liebhart W., "No math: bistatic SAR processing using numerically computed transfer functions," *IGARSS*, pp. *1844-1847*, 2006

[114] Zhang Z., Xing M., Ding J., "Focusing parallel bistatic SAR data using the analytic transfer function in the wavenumber domain," *IEEE Transactions on Geoscience and Remote Sensing*, vol. *45*, pp. *3633-3645*, 2007.

[115] Li Y., Zhang Z., Xing M., "Focusing general bistatic SAR using analytically computed point target spectrum", *APSAR*, pp. *638-641*, 2007.

[116] Ender J. H. G., "Signal theoretical aspects of bistatic SAR," *Proceedings of International Geoscience and Remote Sensing Symposium (IGARSS)*, pp. *1438-1441*, 2003

[117] Walterscheid I., Ender J. H. G., Brenner A. R., "Bistatic SAR processing using an Omega-K type algorithm," *Proceedings of Geoscience and Remote Sensing*, pp. *1046-1067*, 2005

[118] Ender J., "A step to bistatic SAR processing," *EUSAR*, pp. *356-359*, 2004

[119] Giroux V., Cantalloube H., Daout F., "An Omega-K algorithm for SAR bistatic systems," *IGARSS*, pp. *1060-1063*, 2005

[120] Giroux V., Cantalloube H., Daout F., "Frequency domain algorithm for bistatic SAR," *EUSAR*, 2006

[121] Qiu X., Hu D., Ding C., "An Omega-K algorithm with phase error compensation for bistatic SAR of a translational invariant case," *IEEE Transactions on Geoscience and Remote Sensing*, vol. *46*, pp. *2224-2232*, 2008

[122] Sanz-Marcos H., Mallorqui J.J., Aguasca A., "Bistatic fixed-receiver parasitic SAR processor based on the back-projection algorithm," *IGARSS*, 2005

[123] Qiu X., Hu D., Ding C., "Non-linear chirp scaling algorithm for one-stationary bistatic SAR," *APSAR*, pp. *111-114*,2007

[124] Qiu X., Hu D., Ding C., "An improved NLCS algorithm with capability analysis for one-stationary BiSAR," IEEE Transactions on Geoscience and Remote Sensing, vol. 46, pp. 3179-3186, 2008

[125] Zeng T., Liu F.F., Hu C., Long T., "Image formation algorithm for asymmetric bistatic SAR systems with a fixed receiver," *IEEE Transactions on Geoscience and Remote Sensing*, vol. *50*, pp. *4684-4698*, 2012

[126] Munson D.C., O'Brian J. D., Jenkins W. K., "A tomographic formulation of spotlight mode synthetic aperture radar," *Proceedings of the IEEE*, vol. *71*, pp. *917-925*, 1983

[127] Jakowatz C. V., Wahl D. E., Eichel P. H., Ghiglia D. C., etc., "*Spotlight-code synthetic aperture radar: a signal processing approach*," Kluwer Academic Publishers, Boston, 1996

[128] Yu D., Munson D. C., "A fast back-projection algorithm for bistatic SAR imaging," International Conference on Image Processing Proceedings, vol. 2, pp. 449-452, 2002

[129] http://en.wikipedia.org/wiki/Euler_angles